FIRAT UNIVERSITY
GRADUATE SCHOOL OF NATURAL AND APPLIED SCIENCES
TÜRKİYE

THE POSSIBILITY OF EARTHQUAKE FORECASTING WITH IONOSPHERIC TOTAL ELECTRON CONTENT AND RADON-222 CONCENTRATIONS USING MONTE CARLO SIMULATIONS

Pishtiwan Akram Hama Rashid

Doctoral Thesis

DEPARTMENT OF PHYSICS

Division of Nuclear Physics

JUNE 2022

FIRAT UNIVERSITY
GRADUATE SCHOOL OF NATURAL AND APPLIED SCIENCES
TÜRKİYE

Department of Physics

Doctoral Thesis

THE POSSIBILITY OF EARTHQUAKE FORECASTING WITH IONOSPHERIC TOTAL ELECTRON CONTENT AND RADON-222 CONCENTRATIONS USING MONTE CARLO SIMULATIONS

Author
Pishtiwan Akram Hama Rashid

Supervisor
Prof. Dr. Fatih KÜLAHCI

JUNE 2022
ELAZIG

FIRAT UNIVERSITY
GRADUATE SCHOOL OF NATURAL AND APPLIED SCIENCES
TÜRKİYE

Department of Physics

Doctoral Thesis

Title: The Possibility of Earthquake Forecasting with Ionospheric Total Electron Content and Radon-222 Concentrations using Monte Carlo Simulations

Author: Pishtiwan Akram Hama Rashid

Submission Date: 01 June 2022

Defense Date: 30 June 2022

THESIS APPROVAL

This thesis, which was prepared according to the thesis writing rules of the Graduate School of Natural and Applied Sciences, Fırat University, was evaluated by the committee members who have signed the following signatures and was unanimously approved after the defense exam made open to the academic audience.

Signature

Supervisor: Prof. Dr. Fatih KÜLAHCI — Approved
Firat University, Faculty of Science

Chair: Prof. Dr. Zekâi ŞEN — Approved
Istanbul Medipol University, Faculty of Engineering

Member: Prof. Dr. Serpil AKÖZCAN — Approved
Kırklareli University, Faculty of Science and Literature

Member: Prof. Dr. Sefa KAZANÇ — Approved
Firat University, Faculty of Education

Member: Prof. Dr. Mediha KÖK — Approved
Firat University, Faculty of Science

This thesis was approved by the Administrative Board of the Graduate School on

.... / .... / 20 ....

Signature

Prof. Dr. Kürşat Esat ALYAMAÇ
Director of the Graduate School

DECLARATION

I hereby declare that I wrote this Doctoral Thesis titled “The Possibility of Earthquake Forecasting with Ionospheric Total Electron Content and Radon-222 Concentrations using Monte Carlo Simulations” in consistent with the thesis writing guide of the Graduate School of Natural and Applied Sciences, Firat University. I also declare that all information in it is correct, that I acted according to scientific ethics in producing and presenting the findings, cited all the references I used, express all institutions or organizations or persons who supported the thesis financially. I have never used the data and information I provide here in order to get a degree in any way.

30 June 2022

Pishtiwan Akram Hama Rashid

PREFACE

This work emphases two important parameters that registered in earthquake prediction. Firstly, the role of Radon-222 as a precursor and the factors that affect soil radon concentration were studied, and Radon-222 has a great importance on geophysical and geochemical parameters. In addition, Radon-222 involved in a very complex system for predicting earthquakes that is Seismo-ionospheric coupling.

Secondly, the ionospheric precursor of earthquakes such as Total Electron Content (TEC) was introduced. Moreover, this study was carried out to understand the relationship of 222Rn and TEC values with earthquakes and also, correlations between radon and atmospheric pressure, dry thermometer temperature, soil temperature at various depths were discussed.

Hence, in this thesis we forecasted the time series of two parameters through modelling and simulating the collected data. Autoregressive Integrated Moving Average (ARIMA) models, multi-regression models, multi-ANN models, and Monte Carlo Simulations (MCSs) were used.

First of all, thanks to Allah for giving us good health. I will take this opportunity to express my sincere gratitude and due respect to my supervisor Prof. Dr. Fatih KÜLAHCI, I am immensely grateful to him for his valuable guidance, continuous encouragement which helped me a lot during the period of my work. I would like to appreciate him for always providing important suggestions. I also express thanks to my course lecturers, Prof. Dr. Osman ÖZCAN, Assoc. Prof. Dr. Murat CANYILMAZ and Prof. Dr. Bilal ALATAŞ for providing us with valuable knowledge, as well, my friends and classmates for their care and moral support. My special thanks to my mother, father, sisters, brothers, relatives and my wife for their moral and spiritual support. May Allah bless you all.

I would like to thank AFAD-Ministry of Interior Disaster and Emergency Management Presidency for providing us the radon data. I express my gratitude to IONOLAB-TEC Online group of Hacettepe University for permitting the access of TEC values. Also, I would like to thank Firat University for their support.

Pishtiwan Akram Hama Rashid
ELAZIG, 2022

TABLE OF CONTENTS

Page

ABSTRACT

The Possibility of Earthquake Forecasting with Ionospheric Total Electron Content and Radon-222 Concentrations using Monte Carlo Simulations

Pishtiwan Akram Hama Rashid

Doctoral Thesis

FIRAT UNIVERSITY
Graduate School of Natural and Applied Sciences
Department of Physics

June 2022, Page: xvii + 117

This study was handled and discussed in two different dimensions in order to make future earthquake forecasting. First, the role of Radon-222 inert gas as an earthquake prediction precursor is discussed, and the factors affecting soil Rn concentration are examined in a multidisciplinary context in physics, artificial intelligence, geology, and geophysical frameworks. Determining the seismo-ionospheric changes of soil Rn-222 gas requires complex physical and mathematical calculations and forecasting. Secondly, the Total Electron Content (TEC), one of the ionospheric precursors of earthquakes, was discussed. Our aim here was to obtain solid physical evidence for earthquake-based gas and ion exchanges between the earth and the atmosphere; therefore, radon, atmospheric pressure, atmospheric temperature, soil temperature and their interactions were examined at various soil depths to see the physical changes in the journey of the above-mentioned variables from the underground to the Earth's atmosphere (Ionosphere). For all variables, three Autoregressive Integrated Moving Average (ARIMA) models were proposed. Then, the main statistical characteristics of the data were determined and future values of the variables were predicted using Monte-Carlo Simulations (MCSs). In addition to all these, Multiple Linear Regression and Multiple Artificial Neural Network models were obtained for Radon-222 using certain meteorological parameters. While obtaining all these models, as many variables as possible were used to increase the reliability of the calculations and the results were widely discussed within the framework of the relevant field.

Keywords: Monte Carlo Simulation, Artificial Intelligence, Forecasting, Linear Regression, Radon time series, Total Electron Content, Earthquake.

ÖZET

Monte Carlo Simülasyonları Kullanılarak İyonosferik Toplam Elektron İçeriği ve Radon-222 Konsantrasyonları ile Deprem Tahmin İhtimaliyeti

Pishtiwan Akram Hama Rashid

Doktora Tezi

FIRAT ÜNİVERSİTESİ
Fen Bilimleri Enstitüsü

Fizik Anabilim Dalı

Haziran 2022, Sayfa: xvii + 117

Bu çalışma, ileriye dönük olarak deprem öngörülerinde bulunmak için, iki farklı boyutta ele alındı ve tartışıldı. İlk olarak, Radon-222 asal gazının bir deprem kestirim öncüsü olarak rolü tartışıldı ve toprak Rn konsantrasyonunu etkileyen faktörler fizik, yapay zekâ, jeoloji ve jeofiziksel çerçevede çok disiplinli olarak incelendi. Toprak Rn-222 gazının sismo-iyonosferik değişimlerinin belirlenmesi, karışık fizik ve matematik hesaplamalar ve öngörüler gerektirir. İkincil olarak, depremlerin iyonosferik öncüllerinden biri olan Toplam Elektron İçeriği (TEC) ele alındı. Buradaki amacımız, deprem temelli yeryüzü ve atmosfer arasındaki gaz ve iyon değişimleri için sağlam bir fiziksel kanıt elde etmekti. Bu nedenle, yukarıda bahsi geçen değişkenlerin yeraltından dünya atmosferine (iyonosfere) olan yolculuğunun fiziksel değişimlerini görmek için çeşitli toprak derinliklerinde radon, atmosfer basıncı, atmosfer sıcaklığı, toprak sıcaklığı ve bunların etkileşimleri incelendi. Bütün değişkenler için, üç Otoregresif Entegre Hareketli Ortalama (ARIMA) modeli önerildi. Ardından verilerin temel istatistiksel özellikleri belirlendi ve Monte-Carlo Simülasyonları (MCS'ler) kullanılarak değişkenlerin gelecekteki değerleri öngörüldü. Bütün bunlara ilâveten, belirli meteorolojik parametreler kullanılarak Radon-222 için Çoklu Doğrusal Regresyon ve Çoklu Yapay Sinir Ağı modelleri elde edildi. Bütün bu modeller elde edilirken, hesaplamaların güvenirliliğini artırmak için elden geldiği kadar çok değişken kullanıldı ve sonuçlar ilgili alan çerçevesinde geniş bir şekilde tartışıldı.

Anahtar Kelimeler: Monte Carlo Simülasyonu, Yapay Zekâ, Kestirim, Doğrusal Regresyon, Radon zaman serileri, Toplam Elektron İçeriği, Deprem.

LIST OF FIGURES

Page

LIST OF TABLES

Page

SYMBOLS

A	: Area of the Fault
A	: Nuclear activity
Bq	: Becquerel
C	: Concentration of Radon in Soil Gas
Ci	: Curie
α	: Alpha Particle
β	: Beta Particle
γ	: Gamma Rays
D	: Mean Displacement within the Fault
D	: Pressure Diffusivity
$\mathrm{D_a}$	: Diffusion Coefficient in Air
$\mathrm{D_w}$	: Diffusion Coefficient in Water
$\mathrm{D_m}$	: Molecular Diffusion Coefficient
D_a	: Diffusion Coefficient for Radon in Pure Air
D_z	: Diffusion Coefficient for Radon in Soil
$\mathrm{D_{eff}}$	: Effective Diffusion Coefficient of Radon in Soil
∇C	: Gradient of Radon Activity
$\mathrm{E_r}$	: Average Recoil Energy on Formation
$\mathrm{F_a}$	: Advective and Convective Flux Density
f_oF2	: Critical Frequency
M_L	: Local Magnitude
m_b	: Body Magnitude
M_S	: Surface Magnitude
M_W	: Instantaneous Magnitude
N_mF2	: Ionosphere Peak Electron Density
μ	: Shear Modulus of Rocks
J^d	: Activity flux Density
k	: Permeability
ε	: Porosity
η	: Viscosity of Gas
λ	: Decay Constant
^{222}Rn	: Radon-222
^{220}Rn	: Thoron
^{219}Rn	: Actinon
τ	: Mean Life Time
P	: Average Pressure of the Gas
V	: Apparent Soil Gas Flow Velocity

ABBREVIATIONS

ARIMA : Autoregressive Integrated Moving Average

AR : Autoregressive

MA : Moving Average

ANN : Artificial Neural Network

RMSE : Artificial Neural Network

R^2 : R-Squared

MSE : Artificial Neural Network

CME : Coronal Mass Ejections

GPS : Global Positioning System

MCSs : Monte Carlo Simulations

NAFZ : North Anatolian Fault Zone

RAD : Radiation Absorbed Dose

REM : Roentgen equivalent man

TEC : Total Electron Content

USGS : United States Geological Survey

MLR : Multi-Linear Regression

SSE : Sum of Square Error

ADFT : Augmented Dickey-Fuller Test

ESU : Electrostatic System of Units

LSSI : Local Spatial Scintillation Index

1. INTRODUCTION

The soil Rn-222 is formed in Earth's crust by decay of ^{226}Ra naturally, which is a product of ^{238}U decay chain since its creation [1,2]. Radon is an invisible radioactive gas and it cannot be sensed by humans. Rn-222 and its short-lived daughters in the atmosphere are considered to be the second cause of lung cancer [3].

Soil Rn-222 utilized as a signifier for many applications of environmental geology for many decades. Environmental operations have a vital relationship with soil Rn-222, like eruptions of volcanic, tracing in atmospheric, hydro-geological and marine issues, it was investigated as a possible earthquake precursor that occurs when fault blocks move rapidly [4–13].

The journey of radon atoms starts as emanation from mineral grains that contain radium, transportation into soil intergranular pore spaces and exhaled to the atmosphere [14]. This journey has a lot of details due to crucial factors, for example the radon production rate; earth crust movements; the main influences on radon concentration levels include soil porosity, the number of tiny cracks on the surface of the soil, and meteorological variables like temperature, rainfall, and humidity as well. [15].

The Rn-222 is a subject of great importance in Türkiye where the mean of the annual Rn-222 was 81 Bq/m^3, higher than the worldwide mean of 40 Bq/m^3 per year [16]. The radon sources were affected by many factors related to the transient geological tectonic progressions, ground soil characteristics, environmental and climatic variables, carrier gases, solar effect, tide, etc [17–25]. The multi-seasonal of the Rn-222 depicts the evidence of controlling factors, for example tidal forces or climate [26–29]. In all the studies, the behaviours of the controlling factors dealing with radon time series are not univocal and hence the influence of factors has been proposed to be site-specific [30].

The anomalies in Rn-222 time series can play an important role for the purpose of earthquake prediction. There are many studies that conveyed anomalous Radon-222 behaviour in soil, groundwater, thermal spas, and atmosphere to earthquakes [31–39].

Other studies were presented that the fluctuations in radon time series were not only affected due to earthquakes but also from meteorological variables [40,41]. It is important to distinguish between Rn-222 anomalies produced due to earthquakes and those produced only through meteorological influences. There are a lot of researchers who have found that Rn-222 concentration depends upon meteorological variables [42–45].

There is strong evidence that gas emanation (e.g., Radon, carbon dioxide methane, etc.) changes the conductivity of air by several days before major events, raises surface temperature and locally generated electrostatic fields occur. Ground-based and satellite sensors can indicate the abnormal fluctuation of different parameters during earthquakes. The findings of numerous independent post-earthquake analyses of more than hundred strong earthquakes have been very encouraging and encourages us to extensively express the problem for the prediction of earthquakes with magnitudes M>5.5 [46–48]. According to [49], major correlated phenomena before large earthquakes have a common source, air ionization was produced by radon emanating from active tectonic faults.

Now, we can understand the need of introducing the ionosphere. Therefore, briefly we introduced ionosphere and ionospheric TEC precursors of the earthquakes. The ionosphere refers to the Earth's ionized upper atmosphere, ionized as a result of solar radiation and ranging from an altitude of 60-1000 kilometers. It has a significant contribution in the electricity production in the atmosphere and produces the magnetosphere's inner edge.

One of the most significant descriptive quantities of the ionosphere is ionospheric total electron content, well-defined as the entire number of electrons between two locations. Its unit is TECU and equivalent to (10^{16}electrons/m^2) [50].

Large earthquakes' ionospheric TEC precursors have been studied extensively, both as precursors and after effects [36,51,60,52–59]. Precursors of earthquakes in the ionospheric TEC are usually divided into two types: chemical and physical. Temperature, conductivity, and water level are examples of physical precursors. Gases and chemical elements, such as Rn-222 in Soils and underground water in a fault-zone, are chemical precursors that were verified to have a significant contribution in short-term earthquake prediction [61]. Pulinets presented a lengthy list of possible reasons, including Rn-222 eject [36], which cause lower electric fields in the atmosphere to penetrate along geomagnetic lines and into the ionosphere.

Unrelatedly of the precise reasons of earthquake-precursor TEC-anomalies, after excluding other causes of TEC disturbances, variations utilizing the TEC median values were used to show their earthquake relationship statistically, for example geomagnetic storm activity and solar flare [62,63].

In recent years, important development has been achieved in the advancement of unique processing algorithms of ionospheric data for recognizing the ionospheric indicator of earthquakes. [36,64]. The first is dependent on the basic concept that a station nearer to the epicenter of an upcoming earthquake feels the occurrence more than a station faraway. It was understood by calculating the coefficient of cross-correlation between critical frequency data (daily) for stations of ionospheric [65].

This thesis consists of eight chapters. The first Chapter devoted to the introduction of the scope and an in-depth literature review. It provides the basic knowledge of radon and ionospheric precursor, its forward improvements till this time. The second Chapter gives an idea about earthquakes, seismic activities in the world and Türkiye, prediction parameters in crustal movement. Chapter 3 and 4, describes radon and ionosphere as precursors of earthquakes, role of radon in Seismo-ionospheric coupling. Chapter 5 describes the data and study area. The model description was concentrated in Chapter 6. It is concerned with the models for ^{222}Rn concentration and TEC values time series. The results and discussion were given in Chapter 7. Finally, Chapter 8 is devoted to conclusion.

1.1. Problem Statement

Studies have reported the effect of external disturbances into the ionosphere during seismicity [66–68] . The real description of how this disturbance occurs is yet to be clearly defined. On the other hand, Rn-222 has been an agent of seismic studies for decades [32,69]. There is a good chance of having radon's contribution to ionospheric disturbance with its ionizing capability, and abnormality during seismic activities. How can this contribution be investigated? Approaching the problem using purely analytical methods is subject to mathematical constraints. And the limitation is always encapsulated in the assumptions made when modelling the system. On the other hand, statistical/stochastic approaches (e.g., ARIMA) gives only an estimated result, ignoring the true physical mechanisms involved. Another approach is to try the modern artificial intelligence (machine learning techniques), this will allow the inclusion of several parameters of interest in a single model. However, this has been criticized by some scholars as to have been too precise, and does not reflect reality. In this study, we are determined to study and understand the relationship between Rn-222 and TEC, especially during seismic activities in Türkiye (along Anatolian Fault Lines).

1.2. Hypotheses

In this study, we are determined to study and understand the relationship between Rn-222 and TEC, especially during seismic activities. Having this relationship would pave the biggest way to understanding Seismo-ionospheric coupling. Since the focus is to establish the impression that Rn-222 plays a great role in causing Ionospheric disturbance, then any suitable method mentioned would be employed. In this study, we shall present results which will support or refute the Seismo-ionospheric phenomenon

1.3. Motivation

Earthquakes have been a catastrophe throughout centuries; therefore, seismic studies are important, it is known from literature that the ionosphere can also be affected, making it one of the key areas leading to Seismo-ionospheric coupling. Since Rn-222 has been a key player in the seismicity discipline, and with the ionospheric effect. This study would be very significant to understanding this disaster.

1.4. Method

Prior observations were collected and analyzed using time series modelling for ^{222}Rn concentration and TEC values to design appropriate models. The models describe the series' characteristic structure. The models of the series were then used to predict its future values.

The (ARIMA) model is the most often used stochastic model for time series [70–72]. As well, MCSs techniques which are efficient in stochastic evaluations [73] to forecast radon concentration and TEC values. The combination of ARIMA and MCSs together in the scope is a new method, and recently was used by [74].

To build an appropriate model to the actual time series, great care was taken. It is obvious that good model fitting is required for successful time series forecasting. Efforts have been made in this direction for the efficient models such as multi-regression and multi-ANN to improve the forecasting accuracy.

1.5. Social Benefits

Forecasting the earthquake's parameters may serve humanity to be ready for facing the earthquake disasters at least. For example, if the number and magnitude of the earthquake is determined (forecasted) in a specific place then people of that region should take it into their consideration while they construct houses. As well, the statistics of the earthquake occurrences may give us an idea about the increasing number of earthquakes with time. For this purpose, the average number of earthquakes for the magnitude ($M \geqslant 4.5$) per year, according to the statistics of the United States Geological Survey (USGS) was plotted which indicates a positive trend in the number of earthquake occurrence in the world wide.

1.6. Literature Review

In this section of the study, we focused on two main scopes. The first topic is soil radon concentration and its possible connection with underground seismic activities; the second topic is TEC values and its relation with earthquakes. Nowadays, both of the mentioned scopes are hot topics and the researchers dealt in a high-level. Therefore, this section gives review of some research that has been done about these subjects.

1.6.1. Literature Review on Radon Precursor

Many studies have suggested that anomalies in radon time series data could be linked to pre-seismic activities and meteorological parameters. Before a certain period of time, the possibility of an anomalous increase in radon concentrations as a result of underground seismic activities had been determined [75–78]. Changes in the meteorological variables have been significant such as temperature, pressure, and precipitation certainly influence the soil radon emanation [79–81]. Depending on the laboratory investigations, Iskandar et al. discovered that as soil temperature rises, radon emission rises as well [82]. The radon emission falls at times of high air pressure [83]. Radon emanation and transport in the soil are influenced by parent isotope composition, rock porosity, grain size, rock fracture distribution, soil moisture, permeability, and meteorological conditions.

There are possibilities of soil permeability and soil moisture under atmospheric pressure, which influence Rn-222 emanation [80]. The emanation of Rn-222 can be considered as a complicated and non-linear stochastic process depending on potential chaotic variables such as soil temperature, pressure and humidity [84–87]. The existence of dependable soil radon and spring water anomalies have been indicated before earthquakes in Marmara by [80]. The empirical mode decomposition method can be used to detect and remove diurnal fluctuations in Rn-222 emanation data [88,89]. Seasonal variations in Rn-222 time series shown by [81]. In Western Türkiye, regardless of soil properties, Rn-222 emanation is low from November to April and generally high from May to October [81].

Several theoretical and empirical algorithms have been suggested for studying radon earthquake precursory behaviour, such as extracting radon anomalies caused by seismic activity [90,91,100,92–99]. Changes in strain inside the crust are thought to cause positive anomalies prior to earthquakes [93,101,102].

In the literature, several studies have been found in Türkiye which show the radon's significance and earthquake precursory. Some researchers place great importance on research around the North Anatolian fault [103,104,113–115,105–112].

There are many reasons for the interest of Anatolia. The development of Anatolia's neotectonics is mostly characterized by three geodynamic processes [116], (1) the Arabian-Eurasia plate collision caused right directional movement alongside the Bitlis-Zagros Suture Zone during Oligocene-early Miocene, (2) As a result of the due west movement of the Anatolian-block left from the Arabian-Eurasia plate impact area sideways the EAF and NAF Systems, the Anatolian block is able to get away from the Arabian-Eurasia plate collision area [117,118], and (3) Since the early Miocene, the African plate has been subducted beneath Eurasia along the Hellenic [117].

1.6.2. Literature Review on Ionosphere Precursor

After the 1964 "Good Friday" Alaska earthquake, ionospheric influences on earthquakes was published as the first study [119–124]. The wave motions were viewed as being initiated by ground movements prior and post to the earthquake, similar to how seismology views them. As a result, the mechanism of seismo-ionospheric coupling that was observed was the ionosphere coupling of acoustic-gravity waves [125]. The after-earthquake influence was illustrated through a direct seismograms comparison and ionosonde observations of Doppler shift, which describe the vertical oscillation of the ionospheric layer caused by the earthquake's acoustic vibrations [125]. But it should be declared that the effects before the earthquake were identified as well [121,122].

Global ionosphere maps (GIMs) comprising vertical TEC grid data have recently been used to explore ionospheric phenomena [126–128]. In addition, GIMs were considered as a source of data to investigate TEC fluctuations caused by earthquakes [62, 85, 156, 158-162].

In this thesis, the statistical characteristics of the data were determined which were collected for Reşadiye along the Fault Zone of North Anatolian (NAFZ) in Türkiye. Subsequently, ARIMA models were recommended to fit both Rn-222 concentration and TEC values, as well, Monte Carlo simulations techniques were used which are efficient in stochastic evaluations [73] to forecast radon concentrations and TEC values. The combination of ARIMA and MCSs together in the scope is a new method. The purpose of this research was to learn more about the correlations of ^{222}Rn and TEC values with earthquakes and also, correlations between radon and atmospheric pressure, dry thermometer temperature, soil temperature at various depths were discussed. Also, radon time series are modelled by multi-regression and multi-ANN methods using the meteorological parameters. Finally, the obtained Rn-222 concentrations and TEC values were analyzed to see anomalies in the time series, and correlated with seismic events in the study area.

2. EARTHQUAKE

In this chapter, an introduction was given to earthquake occurrence and earthquake parameters, including equation of magnitude scales, prediction parameters in crustal movement. Important earthquakes in the World and Türkiye were mentioned.

2.1. Occurrence of Earthquakes

An earthquake is a discontinued shift through weak zones, which are known as faults in the Earth's crust. According to [129], an earthquake is the result of elastic recoil. Elastic deformation of compression or stretching of the crust happens as a result of the slow flow of substances, produced by thermal and gravitational convection in the mantle [129].

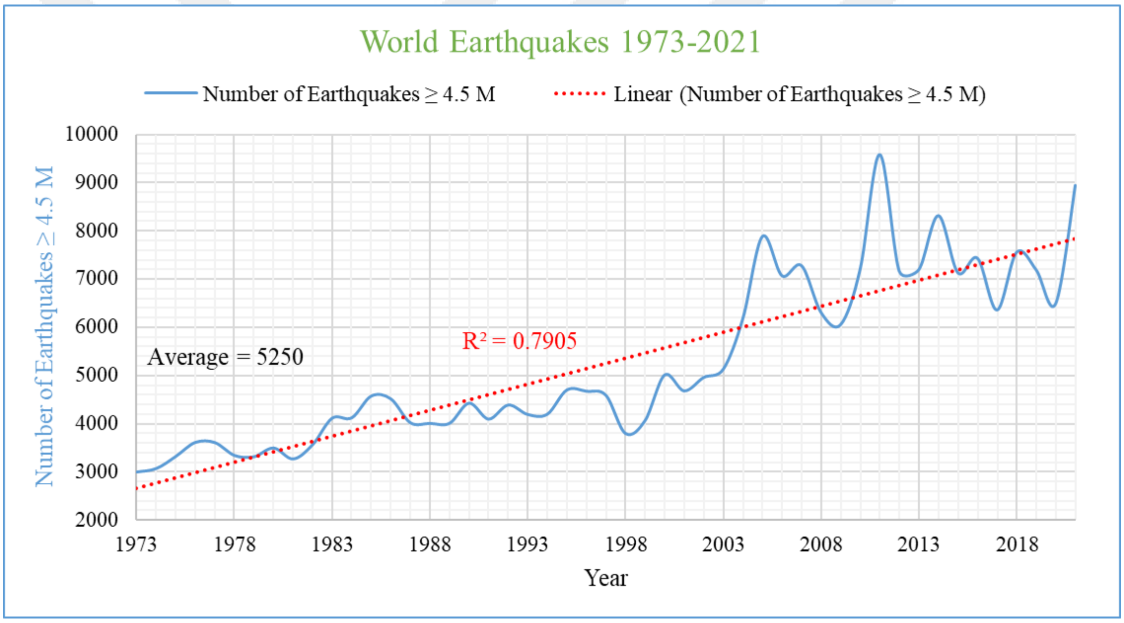

Figure 2.1. The earthquakes annual number for ($M \geqslant 4.5$) from 1973 to 2021, according to statistics of the USGS.

Figure 2.1 illustrates the annual number of earthquakes for 1973-2021 worldwide. and the red dotted line shows the increase in the number of earthquake occurrence for the magnitude ($M \geqslant 4.5$). The average number of earthquakes per year, according to the archived data of the United States Geological Survey (USGS) was shown in **Figure 2.2**,

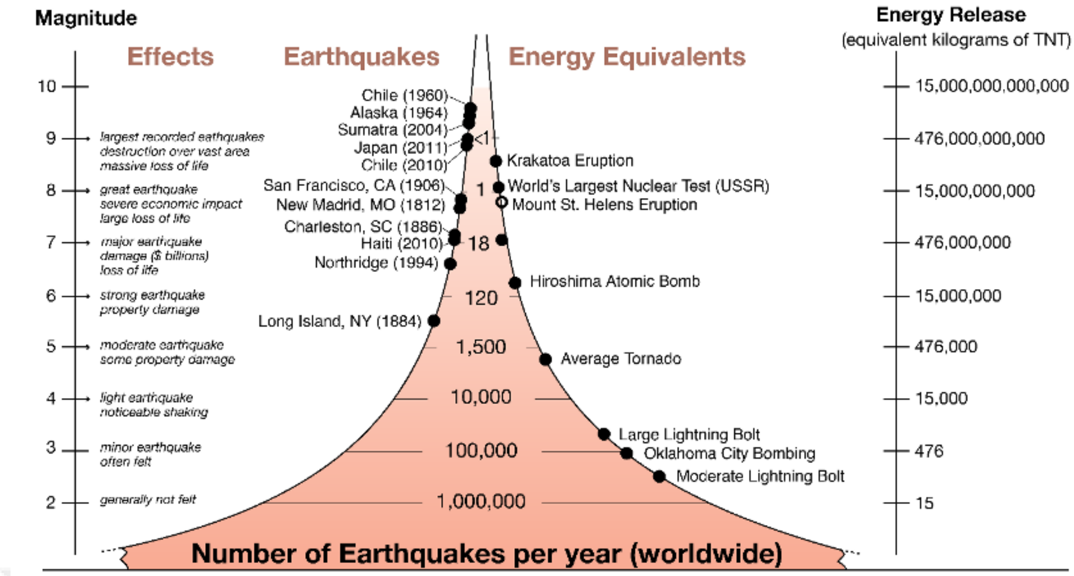

Figure 2.2. The average annual number of earthquakes (x-axis), magnitude (left axis) and energy in trinitrotoluol similar (right axis) produced annually as a result of earthquake shaking [130].

Strong earthquakes have significantly more energy than lots of small earthquakes altogether. For example, the energy of one powerful earthquake with a magnitude of 9.0 is equivalent to the energy released as a result of 1 million earthquakes with a magnitude of 5.0, or equivalent to 32000 earthquakes with a magnitude of 6.0.

2.2. Parameters of Earthquake

2.2.1. Focus/Hypocenter

The focus is the location where seismic energy initially starts to flow at the occurrence of an occurrence. The focus can be obtained from the earliest arrival times unrelatedly of the eventual size and length of the occurrence since the velocity of rupture is smaller than the velocity of P-wave. The epicenter is the *(x, y)* point on the surface of Earth directly over the focus, whereas the hypocenter is the *(x, y, z)* point on the surface of Earth directly over the epicenter [131].

2.2.2. Epicenter

The epicenter was a projection of the hypocenter on the surface of earth that was located on the surface using geographic coordinates. Seismic waves carry the mechanical energy released at the focal through the crustal medium. Epicenter is the point where the earthquake was felt the most and this is also the region where the earthquake caused the most damage.

2.2.3. Focal Depth

The shortest distance from earth's surface to the point (hypocenter) where the energy released during the earthquake can be defined as the depth of the earthquake. This distance is also in the middle of the epicenter region. One of the ways of classification of tectonic earthquakes is according to depth of hypocenter (focus). The earthquakes in each region were classed using the following ranges based on their focal depths:

1. Shallow earthquakes (0 to 70 km)
2. Intermediate earthquakes (71 to 300 km)
3. Deep earthquakes (301 to 700 km)

In Türkiye, the focal depths range from 0 to 60 km which were classified as shallow earthquakes. Deep and Intermediate earthquakes generally occur in supra-subduction zones. The damages caused by deep earthquakes are not much, but they were felt in very large areas. On the other hand, although shallow earthquakes were felt in a narrow area, the damage and destruction effects it creates are quite high.

2.3. Earthquakes Types

Tectonic, collapse, volcanic, and explosion are the four different categories of earthquakes.

2.3.1. Tectonic Earthquake

When the earth's crust splits as a result of geological pressures acting on rocks and plates nearby, physical and chemical changes happen [132].

2.3.2. Volcanic Earthquake

A volcanic earthquake is defined as an earthquake that happens as a result of tectonic forces related with volcanic activity [132].

2.3.3. Collapse Earthquake

Small earthquakes in underground caves and mines are generated by seismic waves created by rock explosions on the surface, causing collapse earthquakes [132].

2.3.4. Explosion Earthquake

An earthquake that occurs as a consequence of the blast of a nuclear or chemical explosion is known as explosion earthquake [132].

2.4. Focal Mechanism of Earthquake

There are numerous types of crustal blocks' relative movement in the moment of an earthquake which are called the focal mechanism. For example, normal faulting, strike slip, thrust or reverse faulting, oblique-slip (combination of mechanisms) could take place as well. The type of slip was determined semi-automatically from the seismic waveforms, and mathematically in the form of the seismic moment tensor was expressed. Visual representation of the focal mechanism was shown by the so-called beachball diagram.

The focal sphere might also be used to show how focal mechanisms worked. To create the old beach ball illustration, the lower hemisphere was designed and the compressional quadrants were shaded. For several forms of focal mechanisms, see **Figure 2.3**.

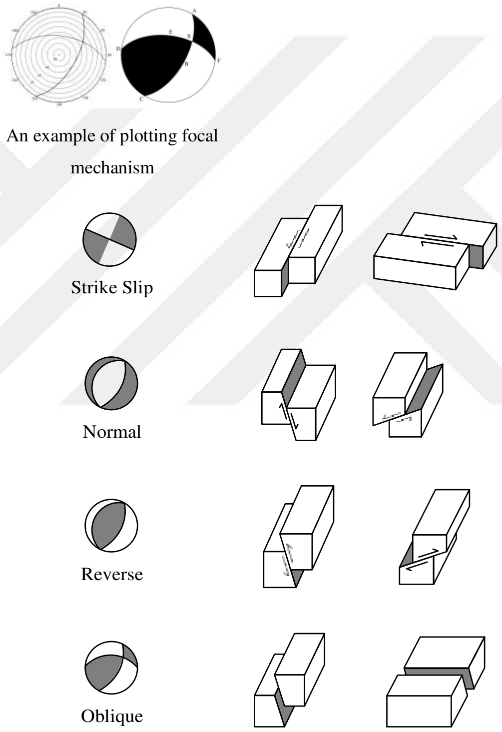

Figure 2.3. Focal spheres and associated fault geometries. With the compressional quadrants shaded, the focal sphere-lower half is on the left. The primary and auxiliary fault planes are depicted in block diagrams on the right [131].

The shaded regions in these graphs depict P waves leaving the source downward with outward first movements, which will cause upward initial movements at the receivers. The sections that aren't shaded will provide downward initial movements at the receivers. The tension axis is located in the shaded area. The pressure axis is located in an unshaded area. In beach ball plots, normal and reverse faulting can be identified by noting whether the plot's center is white or black. A normal fault and a probable extension region are represented by the white in the middle with black edges. A reversal fault and tensional region are shown by the dark in the middle and white margins. [131,133].

2.5. Types of Faults

A fault is a region of cracks that separates two rock blocks. Faults allow the blocks to transfer around in terms of one another. This motion may happen suddenly, like the moment of an earthquake, or slowly, in the form of creep. Faults might be a few of millimeters long or thousands of kilometers elongated. In the moment of an earthquake, the rock along one-side of the fault slips quickly in relation to the other. The surface of fault can be upright, plane, or at slant angle in between. Faults are classified based on how the two blocks move. There are three or four types of main faults [130,132].

2.5.1. Normal Fault

When the hanging wall falls towards the foot wall, it is called a dip slip. This form of faulting occurs as a result of an extension [130,132], example of normal fault is shown in **Figure 2.4**.

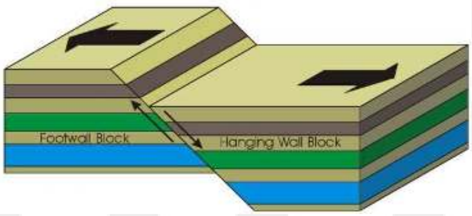

Figure 2.4. Normal fault [134].

2.5.2. Reverse Fault

The hanging wall moves up or thrust over the footwall in a dip-slip fault. This form of faulting happens in compressive areas, and a reverse fault is usually expressed as a thrust fault once the dip angle is shallow [130,132], example of reverse fault is shown in **Figure 2.5**.

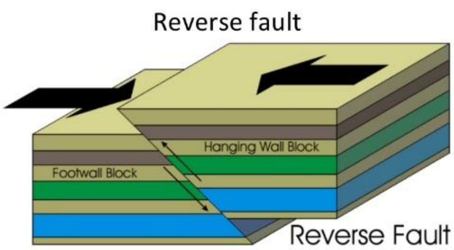

Figure 2.5. Reverse fault [134].

2.5.3. Strike Slip Fault

Due to a fault, the two blocks glide past with one another. The San Andreas fault, for example, is a type of a right-lateral-fault.

Strike Slip Fault- Left lateral

If you were on the fault, looking sideways its extent, and the left-block moved to you. When the right-block travels away then it is a strike slip fault of the left lateral [130,132], example of fault with left lateral strike-slip is shown in **Figure 2.6**.

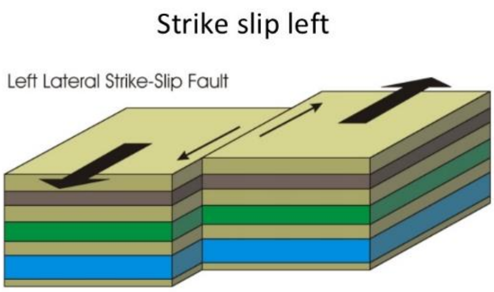

Figure 2.6. Fault with left lateral strike-slip [134].

Strike Slip Fault- Right lateral

If you were on the fault and looking sideways its extent, you'd see where the right-block is traveling to you. When the left-block travels faraway then it is a strike slip fault of right lateral [130,132], example of right lateral strike-slip fault is shown in **Figure 2.7**. The NAF is an active strike slip fault of right lateral that extends along the transform border among the Eurasian and Anatolian plates in the north of Anatolia.

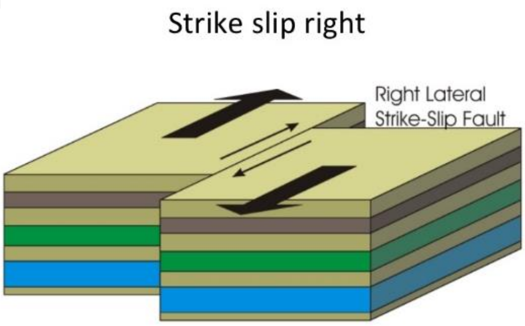

Figure 2.7. Right lateral strike-slip fault [134].

2.6. Fault of North Anatolian (NAF)

Fault region of north Anatolia (NAF) was described by Ketin in the late 1940s [135]. The NAF is one of the world's largest (1500 km long) active continental strike-slip faults at this moment. Reşadiye geothermal area located on the line of NAF [136]. The town of Reşadiye also was surrounded by places where surface ruptures formed during the 1939 Erzincan Earthquake (M_S = 7.8). The North Anatolian Fault Zone is known for the highest seismicity region in the world, and has been caused by many large and destructive earthquakes as illustrated in **Table 2.1**.

Table 2.1. List of recorded earthquakes with $M_S \geq 6.0$ in NAFZ [137].

Location	Date	Latitude	Longitude	M_S
Saroz Gulf	09.08.1912	40.60	27.20	7.3
	08.10.1912	40.60	27.10	6.3
Marmara Sea	22.05.1766	40.80	29.10	7.3
	10.07.1897	40.60	28.70	7.0
	18.09.1963	40.71	29.09	6.4
Sakarya-İzmit	17.08.1999	40.70	29.99	7.8
Duzce-Sakarya	20.06.1943	40.83	30.48	6.4
	26.05.1957	40.80	30.80	6.0
	12.11.1999	40.74	31.21	7.2
	23.08.2000	40.71	30.75	6.3
NAF's Southern Branch	04.01.1935	40.30	27.45	6.3
	04.01.1935	40.30	27.49	6.4
	26.05.1957	40.58	31.00	7.0
Marmara's Southern Region	18.11.1919	39.26	26.71	7.0
	10.06.1944	39.48	26.56	6.8
	18.03.1953	40.01	27.49	7.2
Tosya-Duzce	26.11.1943	40.97	33.22	7.3
	01.02.1944	41.10	33.20	7.3
	13.08.1951	40.86	32.68	6.9
	07.09.1953	40.94	33.13	6.1
Erbaa-Tosya	25.06.1910	41.00	34.00	6.2
	20.12.1942	40.66	36.35	7.1
Erzincan-Tokat	09.02.1909	40.00	38.00	6.3
	18.05.1929	40.20	37.90	6.1
	26.12.1939	39.80	39.38	7.9
	08.11.1941	39.74	39.50	6.0
	13.03.1992	39.72	39.63	6.7
Erzincan's east	19.08.1966	39.17	41.56	6.8
	26.07.1967	39.54	40.38	6.0
	27.01.2003	39.48	39.77	6.0

2.7. Seismic Waves

During an earthquake, the Earth's crust breaks down., different types of seismic waves were generated: volumetric (longitudinal P-waves of compression and lateral shear S-waves), and surface waves (Love waves are polarized upright to the incidence plane, while Rayleigh waves are polarized in the plane of incidence) [129].

2.7.1. Body Waves/Volumetric

It propagates within the earth's interior and reaches before the surface waves caused as a result of an earthquake. These waves frequency is higher than of surface waves [138].

P-waves

P-waves, or primary waves, are the first category of body wave. It is the fastest type of earthquake. The P-wave can travel within fluids and solid rock, forming earth layers. P-waves pull and push-on rock. The primary waves of a seismic event are sometimes heard by animals. For example, just before an earthquake 'hits,' dogs start barking hysterically. (Or before the arrival of the surface waves). People can usually only hear the bumps and rattles of these waves. Because of the pulling and pushing that primary wave do, they are categorized as compressional waves. The particles travel in the same path as the wave and energy, or direction of wave propagation [138].

S-waves

The S-wave or the secondary wave, is the second body wave that may be felt during a seismic event. Secondary waves are slower than primary waves and able to travel within solid rock rather than liquid. Secondary waves make rocks to move upward and downward, vertical to the wave's traveling direction [138].

2.7.2. Surface Waves

Surface waves move within the crust. It has a lower frequency compared to body waves, making them easily distinguishable on a seismogram. They reach after body waves. They are in charge of the destruction that ends up with seismic events. In deeper earthquakes, the strength of the surface waves was attenuated [138].

Love Waves

A Love wave is the fastest surface wave, and it causes the ground to shift from side to side. Its motion is fully horizontal [138].

Rayleigh Wave

It travels across the ground in the way a wave travels across a lake. It causes the ground to shift down and up, as well as side to side, in the wave's direction. It may be significantly greater than the other waves which is accountable for the most of the vibrations felt in the time of a seismic event [138].

2.8. Magnitude Scales

An earthquake is a major source of energy releasing those changes into thermal energy, energy of plastic deformation and energy of seismic waves. Only the seismic waves were used to evaluate earthquake energy.

The decimal logarithm of the highest amplitude is the local magnitude. At a distance of 100 kilometers from the epicenter, it was recorded by a standard Wood-Anderson seismograph. Local magnitude M_L might be calculated as shown in Equation (2.1) [131]:

$$M_L = \log_{10} A + 2.56\log_{10} - 1.67 \tag{2.1}$$

where A (μm) stands to the amplitude of waveform; Δ (km) is the path between the epicenter to the seismograph. The equation is valid for values of ($10 < \Delta < 600$ km).

The energy of each wave is different. It is some part of the total energy of the earthquake, hence the magnitude was determined on the basis of seismic waves which changes, depending on the kind of wave that was used (Equation (2.1)–(2.4)) [131].

The determination of magnitude based on body waves' recording was given by the Equation (2.2) [131]:

$$m_b = \log_{10}(A/T) + Q(h,\Delta) \tag{2.2}$$

where A (μm) stands to the amplitude; T (s) stands to the wave period; Δ (km) is the path between the epicenter to the seismograph. The calibration function is $Q(h, \Delta)$ which depends on the focal depth h (km) and distance Δ, Geometric waves' divergence and attenuation due to absorption was considered.

To calculate the magnitude of an earthquake by surface waves Equation (2.3) is used [131]:

$$M_S = \log_{10}(A/T) + 1.66\log_{10}\Delta + 3.3 \tag{2.3}$$

Magnitude M_S is identified in the period of 20 seconds. Magnitude m_b is identified in the duration of (0.3-3 s). Magnitude scales m_b and M_S for strong earthquakes produce lower values for magnitude. This phenomenon was called the saturation of magnitude scales. With the intention of avoiding errors in measuring the strength of an earthquake, Kanamori suggested to determining the magnitude using the seismic moment M_0 (Nm) or moment magnitude[139]. Instantaneous magnitude is shown by M_W and calculated by using Equation (2.4):

$$M_W = 0.67 \log_{10} M_0 - 10.7 \tag{22.4}$$

where $M_0 = \mu DA$; μ is the shear modulus of rocks (about 30 HPa); A denotes the fault's area; D is the fault's average displacement.

2.9. World and Türkiye Earthquake

Considering the effects of earthquakes in the world, there are two main earthquake belts. They are the Pacific earthquake zone and Alpine - Himalayan earthquake zone. About 81% of the earthquakes occurring in the world were in the Pacific earthquake zone and 17% were in the Alpine - Himalayan earthquake zone [140].

Türkiye is located inside the big Alpine belt, which stretches beginning from the Atlantic Ocean to the Himalayas. Along strike-slip faults, the Anatolian Plate moves westward and southwestward (EAFZ and NAFZ). The addition of continuous Rn-222 activities in soil to the seismic activity adds important insights. Southern and western Türkiye have had a lot of seismic events in the previous few thousand years. The destruction of nearly 1900-year-old Biblical churches in Izmir is one of the most striking examples.

2.10. Parameters of Prediction in Crustal Movements

The conventional method of earthquake prediction depended on the seismic cycle, which entails the periodic storage and discharge of seismic stress while considering continual tectonic plate motion. In other cases, such as the Parkfield earthquake series, the earthquake sequence has a regular periodicity. The mechanism of the 1906 California earthquake was outlined and the theory of elastic rebound was presented [141].

Variations in some parameters discovered prior to the earthquake for example changes of chemical and physical properties of materials composing the crust. These changes lead to the generation of different kinds of anomalies in the earthquake preparation zone; these changes were called the precursors of earthquakes and serve as a basis for earthquake forecasting.

According to the dilatancy-diffusion model [142,143], at different stages of an earthquake's cycle in the earthquake preparation zone different changes of geophysical parameters can be observed [141]. **Figure 2.9** shows the idea of the seismic cycle stages [144]. Among them, the seismic velocity (change in the relation of longitudinal and transverse waves velocities V_P/V_S), the resistivity of the Earth's crust, the ratio of strong and weak aftershocks, as well as geochemical precursors (e.g., radon emanation) can be observed. Data of these changes built a physical basis for predicting future earthquakes [145].

The macroscopic diffusion coefficient, which falls during compression and increases during unloading, was used to determine radon migration. The loading-unloading procedure used in the time of earthquake preparation is the main cause of Rn-222 fluctuations prior to earthquakes. Several papers used Rn-222 fluctuations as a short-term seismic predictor before the earthquake [146–149]. Before the Kobe earthquake, there was a radon anomaly, which was depicted in **Figure 2.8**.

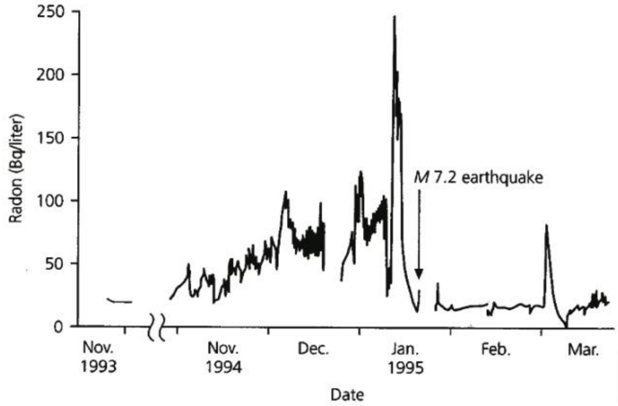

Figure 2.8. Radon in groundwater before and after Kobe earthquake in Japan (16 January 1995) [150].

The increase in radon concentration was noticed some distance away from the fault when measuring Rn-222 in the region of tectonic faults in California [147]. The future earthquake's epicenter is located within the compression zone, where radon concentrations decrease prior to the occurrence of the earthquake (called "near zone"). For a 5-magnitude earthquake, the near-zone radius is approximately (24 ± 15 kilometers). The size of the near region grows in proportion to the magnitude of the earthquake. The stretching zone surrounds the compression region, where Rn-222 rises prior to the earthquake (known as the "far-zone," with a radius of around 110±40 for a 5-magnitude earthquake).

In the seismotectonic regions, the concentration of gases for example Rn, CO_2, He, CH_4, Ar, H_2, N_2, O_2, Na, Cl, Rb, and Hg were found in the soil and underground waters were also changed before, during and after the earthquake [151]. Precursory variations in several parameters before an earthquake were shown in **Figure 2.9**. Different ionospheric precursors were shown in **Figure 2.10** for some strong earthquakes. Anomalies appear as either a negative or positive signal, or both. Ordinary daily variations shadowed more complex examples, which could not be identified without expertise [152]. Data analysis has revealed that information concerning strong earthquake preparation is always seen in ionospheric data. Solar cycle and seasonal dependencies have regular character, while electric field variations are sporadic [36].

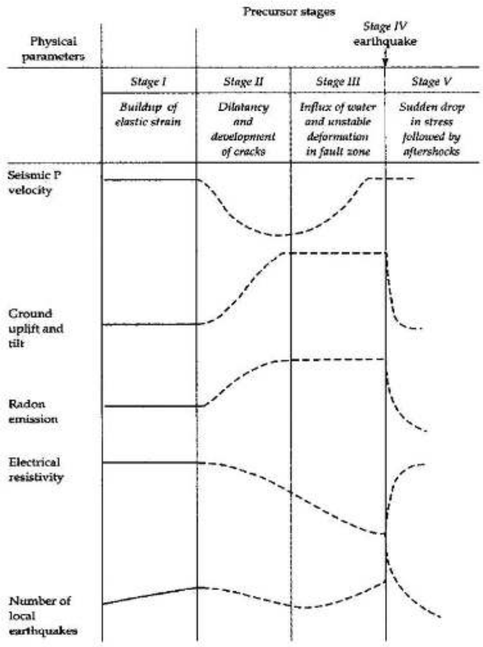

Figure 2.9. Precursory variations in several parameters before an earthquake occur during the interval of earthquake preparation [144].

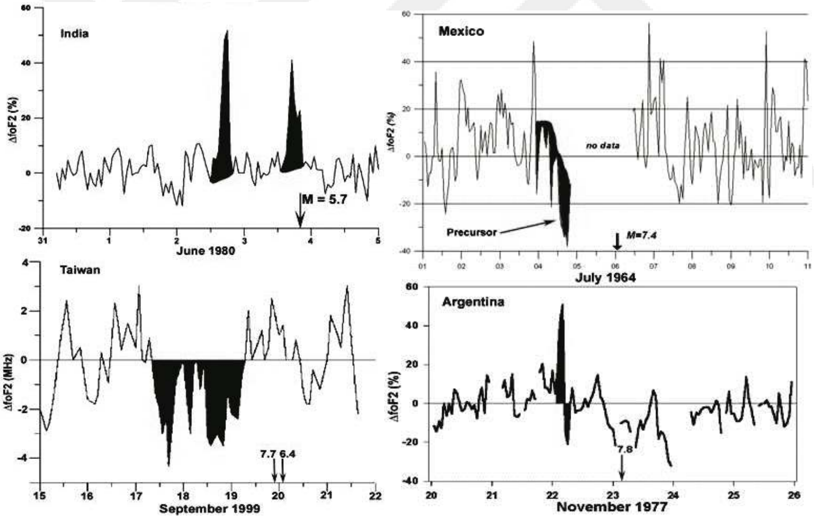

Figure 2.10. Ground-based ionosondes recorded a variety of ionospheric precursors. M=7.4 in Mexico, Jul. 6, 1964; Earthquake in Argentina's Causete, Nov. 23, 1977, M=7.8; M=6.6 earthquake at Ahmedabad, India, Jul. 23, 1999; Earthquake in Taiwan's Chi-Chi. M=7.7 Sep. 20, 1999 [36].

3. RADON

This chapter includes sections and subsections to give detailed information about soil radon. Radioactive decay, diffusion, radon measurement techniques, radon transport, the effect of meteorological parameters on radon and radon precursor are from the selected sections.

3.1. The Basic Concepts of Radioactive Decay

The half-lives of naturally occurring uranium and thorium minerals are on the order of the Earth's age. The shorter-lived nuclei have long disappeared, leaving just the long-lived decays to see today [153].

3.1.1. The Decay Law of Radioactive

Because it is impossible to predict when an unstable nuclide will decay. The chance of an atom decaying throughout time dt is denoted by λdt, where λ is the proportionality constant or decay constant. The decay number of atoms in time dt is denoted by $-dN = \lambda N dt$, where $N(0)$ number of atoms exist originally. In the case of extremely short-time intervals, it is possible to write it as

$$\frac{dN}{dt} = -\lambda N \tag{3.1}$$

Integrating relative to time denotes the number of atoms existing at any point in time t [154].

$$N(t) = N(0)e^{-\lambda t} \tag{33.2}$$

3.1.2. Activity

The mean number of decay processes that a radioactive sample undergoes per unit time is the activity or strength of the sample. This is an extrinsic quantity that is proportional to the amount of source material in the sample (the larger sample the greater the total number of decays) [155]. The activity A, or the decay number per unit time, is denoted by

$$A = -\frac{dN}{dt} = \lambda N \tag{3.3}$$

3.1.3. Half-life and Mean life Time

It is the time for the number of atoms to reduce to half of its original value. It was calculated using the half-life, $t_{\frac{1}{2}}$, i.e., $\frac{1}{2} = e^{-\lambda t_{\frac{1}{2}}}$. As a result of this relationship, the half-life was correlated to the decay constant [154].

$$t_{\frac{1}{2}} = \frac{In2}{\lambda} \approx \frac{0.693}{\lambda} \tag{3.4}$$

The average or mean life time of a radioactive material (τ) is another useful time scale for obtaining decays. It's the average amount of time a nucleus takes before decaying. It has the following relationship with the decay constant (λ) [156]:

$$\tau = \frac{1}{\lambda} \tag{3.53}$$

3.1.4. Types of Radiation Decay and Properties

Alpha decay, beta decay, and gamma decay are the three forms of radiation associated with radioactive decay.

Alpha Particles

The following method can be used to describe the spontaneous emission of an alpha particle:

$${}_{Z}^{A}X_{N} \rightarrow {}_{Z-2}^{A-4}X'_{N-2} + \alpha \tag{3.6}$$

The nuclei of some unstable atoms emit alpha particles, which are a form of ionizing radiation. Its symbol is α. Two protons and two neutrons make up a helium nucleus (${}_{2}^{4}He$). The initial and final nuclei are X and X', respectively, whereas N is neutrons' number, A is the number of total mass, and Z is protons number [153]. Heavy nuclei such as uranium, polonium, radium, and thorium emit alpha particles, which have much higher neutron numbers than protons. Alpha particles are positively charged due to the presence of two protons in their structure, and they have a large mass due to the presence of neutrons and protons. Alpha particles travel at around one-twentieth the speed of light in air, depending on the energy of the individual particle. Because of their short trajectories, they can quickly be absorbed by passing materials.

$$\frac{226}{88}Ra \rightarrow {}_{86}^{222}Rn + {}_{2}^{4}He \tag{3.7}$$

As illustrated in equation (3.7), the decay of Radium-226 to Radon-222 is a good example of this type of decay. Typical alpha particle emitters include uranium (Uranium (^{238}U), Radon (^{222}Rn) and Radium (^{226}Ra).

Beta Particles

The conversion of a proton to a neutron or a neutron to a proton is the most basic β decay process. β decay changes both Z and N by one unit in a nucleus: therefore, $A = Z + N$ remains constant. The charge of beta particles can be either negative or positive. Regardless their charge, they have the equivalent very small mass (1/2000 the mass of a neutron). Alpha particles can't penetrate as far as beta particles can. A sheet of aluminum, on the other hand, can easily stop them.

$$neutron \rightarrow proton + electron \quad \beta^- \ decay \tag{3.8}$$

$$proton \rightarrow neutron + positron \quad \beta^+ \ decay \tag{3.9}$$

$$proton + electron \rightarrow neutron \quad electron\ capture \tag{3.10}$$

Negative β decay, or negatron decay, was the first process. An ordinary electron is created and emitted in this process. The second process is positive β decay, also known as positron decay, which involves the ejection of a positively charged electron. In the third process, an atomic electron is captured, allowing a proton to be converted to a neutron. The neutrino was emitted in all three processes, and because it has no electric charge, its presence in the decay process has no effect on the identity of the generated particles [153].

Gamma Ray

Electromagnetic waves emitted by radioactive nuclei are known as gamma rays (such as ^{137}Cs and ^{60}Co). Cosmic rays, which come from space and reach the Earth's atmosphere, contain high-energy gamma rays. They are highly penetrating and cause serious damage to live tissues when absorbed [157]. The time it takes for a gamma ray to be emitted from an excited nuclear state is usually only 10^{-12} s, so it's almost instantaneous [158].

3.1.5. Radiation Units

Radiation was measured using two sorts of measures: activity units and exposure units (dose). The amount of radiation emitted by a given radiation source is measured in units of activity. The amount of radiation absorbed or deposited by a radiation source is measured in exposure units [159]. Activity A is the number of disintegrations, nuclear transformations, or decay events per unit time in a sample. Disintegrations per minute (dpm) and disintegrations per second (ds) are two commonly used informal units (dps).

The Curie (Ci) is the US unit of activity. One Curie is $3.7 * 10^{10}$ dps or $2.2*10^{12}$ dpm. The millicurie and microcurie are two common multiples. The Becquerel is the SI unit of activity (Bq). One Becquerel is 1 dps [159].

$$1\,Ci = 3.7 * 10^{10}\,Bq \tag{3.11}$$

$$1\,Bq = 2.7 * 10^{-11}\,Curie \tag{3.12}$$

The Roentgen (R) is known as a unit of measurement for radiation of gamma ray or X-ray. In 1cm^3 of dry air, 1 R is the quantity of radiation of X-ray or gamma that deposits sufficient energy to strip approximately 2x10^9 electrons off their orbits (1 ESU). The roentgen was only used to ionize dry air [160].

The quantity of absorbed dose in a substance is measured by the Radiation Absorbed Dose (RAD). One RAD is equal to 0.01 gray, and 100 RADs are equal to one gray.

The REM is used to describe the biological effects of ionization on human tissue. The damage caused by one rad of β-radiation is smaller than that of one rad of α-radiation. The Sievert is a unit of biological damage in the International System of Units (SI) [160].

$$one\ RAD = 0.01\ Gray \quad (3.133)$$

$$one\ REM = 0.01\ Sievert \quad (33.14)$$

3.2. Radon and Its Progeny

Friedrich Ernst Dorn discovered radon, a radioactive, odorless, colorless, and tasteless noble gas, in 1900. It has an atomic number of 86 and is found naturally as a decay product of thorium or uranium. Radon-222 is the most frequent and stable form. Radon-222 will eventually degrade into Pb-206. It melts at -71°C and evaporates at -61.8°C. It has a density of about 8 times that of the sea level Earth's atmosphere. At 25 degrees Celsius, Rn-222 is the densest of the noble gases and one of the heaviest gases [161]. Organic liquids are more soluble in radon than water. Rn-222 has a chemical sorption characteristic that is inert, meaning no reaction with other elements. Radon was thought to have no interaction by the soil grains surfaces. Isolated radon sorption onto rock-grains and soil in some circumstances were described by [162].

Radon's physical parameters are listed in **Table 3.1**. As well, the physical and nuclear characteristics for Rn-219, Rn-220 and Rn-222 summarized in **Table 3.2**.

Table 3.1. Radon's atomic, physical, and chemical characteristics [13].

Properties	Value
Atomic number	86
Standard atomic weight $A_{r,std}$	222
Outer shell electron configuration	$6s^2 6p^6$
Density ρ (at 0 °C, atm press.)	9.73 kg/m^3
Melting point T_m	202 °K
Normal boiling point	208.2 °K
Fusion heat L_f	3.25 kJ/mol
Vaporization heat Lv	18 kJ/mol
1st ionization enthalpy	1037 kJ/mol
States of oxidation	0, 2, 6
Electronegativity χ (Pauling scale)	2.2
Covalent radius r_{cov}	0.150 nm
Radius of Van der Waals r_v	0.220 nm

Table 3.2. Physical and nuclear characteristics of ^{222}Rn, ^{220}Rn and ^{219}Rn [13].

Parameters	Symbol	Rn-222	Rn-220	Rn-219
Half-life	$T_{1/2}$	3.8 d	55.8 s	3.98 s
Decay constant	λ	$\sim 2.1\times 10^{-6}$ s^{-1}	$\sim 1.24\times 10^{-2}$ s^{-1}	~ 0.17 s^{-1}
$E_{avg, recoil}$ on formation	E_r	0.086×10^5 eV	1.03×10^5 eV	1.04×10^5 eV
Diffusion coefficient (air)	D_a	10^{-5} m^2/s		
Diffusion coefficient (water)	D_w	10^{-9} m^2/s		

The three radioactive isotopes of radon that occur naturally are; ^{222}Rn (Radon) is a uranium series decay product in **Table 3.3**, The two most abundant radioactive substances on the earth are thorium and uranium. They have existed since the beginning of time. Isotopes that are found in nature have extraordinarily lengthy half-lives, in the billions of years range.

The relative significance of the three radon isotopes is determined by their mean lifetimes and abundance. 5.51d, 80.2*s*, and 5.71*s,* respectively are the mean lifetimes of ^{222}Rn, ^{220}Rn, and ^{219}Rn. The natural ratio of $^{235}U/^{238}U$ is 0.00719. Consequently, ^{219}Rn was formed in much smaller amounts than ^{222}Rn. In comparison to ^{222}Rn, ^{220}Rn has a short half-life. The mean diffusive motion distances for ^{220}Rn and ^{222}Rn are thus 0.029m and 2.2m, respectively. In this study, the radon isotope ^{222}Rn is the most concerning [161].

Table 3.3. Uranium's decay series till Rn-222 (U-238) [161].

Isotope	**Half life**	**Decay**
^{238}U	4.49×10^9 *year*	*Alpha*
^{234}Th	24.1 *day*	*-Beta*
^{234}Pa	1.17 *minutes*	*-Beta*
^{234}U	2.48×10^5 *year*	*Alpha*
^{230}Th	7.7×10^4 *year*	*Alpha*
^{226}Ra	1.6×10^3 *year*	*Alpha*
^{222}Rn	3.82 *day*	*Alpha*

3.3. Diffusion of Radon

The main form of radon transport from the earth to the air is molecular diffusion [17,18]. According to Fick's law, the Rn-222 flow density is proportional to the gradient of concentration, hence the activity flux density occurring from random motion of molecular is obtained:

$$J^d = -D_m \nabla C \quad (3.15)$$

where J^d is activity flux density ($Bq/m^2\ s^1$), D_m (m^2/s) is the molecular diffusion coefficient and ∇C is the Rn-222 gradient (Bq/m^4). The minus sign was used to show that Rn-222 spreads from higher to lower concentrations. In air (D_{ma}) and water (D_{mw}), the molecular diffusion coefficients are around 10^{-5} and 10^{-9} m^2/s, respectively Table 3.2.

For two reasons, the rate of Rn-222 transport in earth is slower than in a homogeneous medium like pure air: (1) path of the tortuous flow(τ) around particles and (2) fluid volume comparatively is smaller (porosity = *n*). The bulk radon flux density can be calculated by taking these two factors into account:

$$J^d = -n_s \tau D_m \nabla C \quad (3.16)$$

where n_s is the soil porosity. In a pure solution, Tortuosity (τ) is unity, but in soils it is usually less than unity. Closely packed uniform spheres have a value of 0.66. When the terms D_m and τ are integrated, the coefficient of diffusion of the pore fluid is calculated,

$$D = \tau D_m \quad (3.17)$$

Substituting for D from Equation (3.17) in (3.16),

$$J^d = -n_s D \nabla C \quad (33.18)$$

D_e, which is the coefficient of effective bulk diffusion inside earth, is the product of porosity and *D*. The radon diffusion length in the matrix is linearly proportional to *D*. The ^{222}Rn location determines the radon diffusion coefficient in soil. The soil category, water content, pore size distribution, and porosity all play a significant role. In air and water, the molecular diffusion coefficients differ by a factor of 10^4. As a result, moisture effects dominate. According to researchers, radon diffusion is significantly influenced once moisture of soil crosses a specific threshold, which is determined by the geometry of the soil pore size [163].

3.4. Radon Measurement Techniques

The amounts of ^{222}Rn and its daughter products in the environment have been measured using a variety of techniques. In comparison to subsurface groundwater, Rn-222 in surface waters is very low. In comparison to soil air, radon concentrations in atmospheric air are usually lower.

Techniques for measuring radon were categorized based on three factors: whether they measure ^{222}Rn or its daughter products, time resolution, and radioactive detection of the type of emission. The majority of approaches depend on the discovery of α-particles. To measure radon isotopes, a single alpha particle was sometimes detected or all 3 α-particles produced in the decay of ^{222}Rn were counted using scintillation counters. Some approaches rely on the detection of γemission produced by the progeny of ^{222}Rn (e.g., ^{214}Bi, ^{214}Pb) during radioactive decay. However, beta decays are used in only a few methods.

For sampling and analysis, there are three types of time resolution: (a) *The grab-sample* technique includes measuring ^{222}Rn in a separate sample of water or air obtained at a single place during a short period of time, RAD7, for example, can detect ^{222}Rn in the air at any time; (b) *The continuous* technique allows for simultaneous measurement of time-series ^{222}Rn concentrations in soil gas, air, and water samples. Smart Radon Duo and Scintillation Radon Monitors, for example, are new instruments that may be used to continuously monitor ^{222}Rn and ^{220}Rn in air, soil gas, and water. This type of measurement is extremely useful when utilizing ^{222}Rn as a tracer to predict earthquakes.; and (c) technique of *Integrating* offers the average concentration for a specific duration of time. This information can be used to calculate the average ^{222}Rn concentration in a building on a monthly or annual basis [13].

3.5. Processes of Radon Transport Below the Earth's Surface

There are two types of gases in the geosphere, carrier and trace gases [164]. The main representatives of them are CH_4 and CO_2 as carriers whereas Rn and He are trace gases. Different forms of gas migration were studied such as dry and saturated diffusion, water and gas-phase advection. The main language of Lithosphere–Atmosphere communication are gases.

Typical radon concentrations in soil gas vary from 370 Bq/m^3 to 3.7 × 10^4 Bq/m^3 (10-1000 pCi/L) [165]. Advection and diffusion are the two main mechanisms of subsurface radon transport. These transportation methods were divided into two categories: fluid convection and earth-mechanical [165].

3.5.1. Mechanisms of Earth-Mechanical Transport

The following are examples of earth-mechanical transportation [165]:

(i) Temperature differences between the soil and the air

(ii) Changes in barometric pressure

(iii) Surface effects of wind turbulence

(iv) Seismic stress causes variations in pore pressure.

(v) Other gases sweep the area, e.g., volatile organic compounds from soil hydrocarbons.

(vi) Effects of tidal pumping on the Earth

The pumping effect, which transports radon from sources to the surface, is well understood. At a depth of less than 2 meters, however, the pump action has no effect. Underground channels, cracks, and fissures are used to transport ^{222}Rn from the subsurface to the surface of the earth. In some circumstances, radon is transported due to natural heat gradients and pressure differentials. According to studies, radon levels in the topsoil layer are reduced when there is a high wind velocity over several hours. Strong winds drop surface pressure, allowing upper soil air with high ^{222}Rn concentrations to mix with the free air. Additionally, short-term Rn-222 measurements in soil have revealed long-term fixed fluctuations (6-12 h) produced by tidal influences on the earth. The closing and opening of pore spaces during the tides causes a pumping effect, which drives underlying ^{222}Rn to the exterior. Subsurface seismic activity causes considerable variations in ^{222}Rn activities in groundwater and soil, according to the findings.

3.5.2. Fluid Convection Mechanism

Convection is the most common way for energy to move through fluids. Radon released underneath was taken to the exterior by fluid convection inside the earth, similar to how water vapor is transported from the earth's surface to the air. Subsurface temperature gradients enable warmer (lighter) fluids to travel higher and cooler fluids to move lower, resulting in a convection cell, which can be produced using water or soil gas as shown in **Figure 3.1** [166].

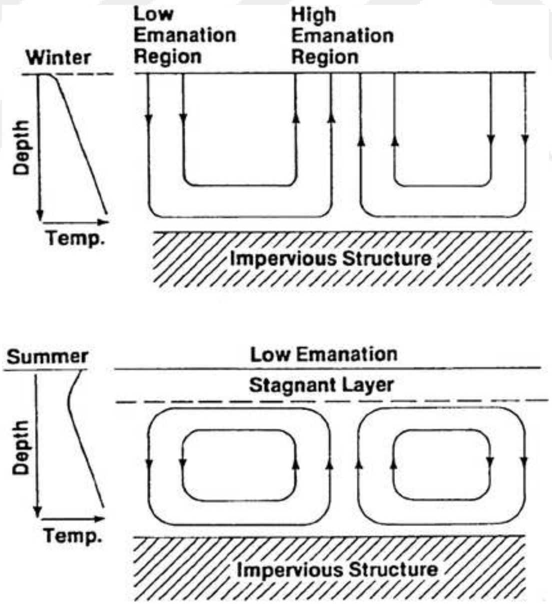

Figure 3.1. Subsurface fluid convection patterns [166].

The convective fluid mechanism inside the earth produced by the geothermal gradient in air or, through the buoyancy triggered in water, *dT/dz*, convection cells may form within the ground as a result. Its stability condition based on a selection of factors including hydraulic permeability (*K*), Changes in fluid density as a function of temperature (*dρ/dT*), vertical dimension of convective area (h), viscosity of the fluid (η), and the fluid-filled medium's thermal diffusivity (D). Convection has been reported to occur when the following conditions are met:

$$Kgh^2(\mathrm{dT/dz})_{\mathrm{net}}(\mathrm{d}\rho/\mathrm{dT}) > 4\pi^2\mathrm{D}\eta \tag{3.19}$$

where g denotes gravity's acceleration. The vertical dimension of the convective zone of 100 m is given by Equation (3.19), and $(dT/dz)_{\mathrm{net}}$ = 30 °C/km, and experiences convection ($K > 3 \times 10^{-7}$ cm^2) [166].

Long-distance radon transport is thought to be possible due to a general vertical flow of other gases working as a radon carrier [167]. The study of radon measurements was done by [166] at a depth of 60 cm below the earth's surface shows possible convective flow.

3.6. Vertical Transport of Radon in Subsurface Soil

The vertical transport of Rn-222 can be defined using the conservation of continuity equation and radon mass. A number of researchers have used this equation [4,168,169]. Diffusional and advective transport are the two main mechanisms for vertical radon transport from subsurface soil. The mass of transported Rn-222 per unit of cross-sectional area per time can be calculated using the advective and convective flux density (F_a):

$$F_a = vC \tag{3.20}$$

where C denotes the radon concentration in soil gas, which is defined as the Rn-222 mass per volume, and v denotes the Darcy's velocity, which is defined as the air volume flowing per area of cross-sectional area per time in the direction z (upward). Fick's law defines the diffusive flux density (F_d) as the mass of transported Rn-222 per cross-sectional area per time:

$$F_d = D_z \partial(nC)/\partial z \tag{3.21}$$

where n denotes the effective porosity of gas, the radon diffusion coefficient in the direction z is D_z, and the mass of Rn-222 in the volume of soil is denoted by nC. The diffusion coefficient for Rn-222 in pure air (D_a) and the coefficient of diffusion for Rn-222 (D_z) were connected as follows:

$$D_z = D_a \tau_z \tag{3.22}$$

For damp soil, τ_Z is the coefficient of tortuosity. The following continuity equation explains the conservation of mass of radon:

$$\frac{\partial(nC)}{\partial t} = -\frac{\partial F}{\partial z} - \lambda nC + n\Phi \tag{3.23}$$

where F in direction z is the total flux density ($F_d + F_a$), t is time, the decay constant for ^{222}Rn is λ, and U is the source term. It is a production rate of Rn-222 concentration in moist soil pore space per unit volume. Putting Equation (3.21) for F_d and (3.20) for F_a in Equation (3.23), the equation of transport will be:

$$\frac{\partial C}{\partial t} = \partial\left(D_z \partial C / \partial z\right) / \partial z - \partial(vC / n) / \partial z - \lambda C + \Phi \tag{3.243}$$

Because the vertical diffusion constant is constant, the advectional transport ($v\partial C / \partial z$) is substantially bigger than $C\frac{\partial C}{\partial z}$, Equation (3.24) simplified to:

$$\partial C / \partial t \approx D_z \partial^2 C / \partial z^2 - (v / n)\partial C / \partial z - \lambda C + \Phi \tag{3.253}$$

where $D_z \partial^2 C / \partial z^2$ is the diffusion term, $(v / n)\partial C / \partial z$ is the advective flow, and λC is the decay of ^{222}Rn and Φ is the production. Via the boundary settings**:** $\mathrm{C}(0, \mathrm{t}) = 0$ and $\mathrm{C}(-\infty, \mathrm{t}) = \Phi / \lambda$ Rn-222 gas concentration in the soil was supposed to be at steady state [217].

3.7. Influence of Meteorological Parameters on Radon Release

Temperature, pressure, wind speed, and the amount and frequency of precipitation can all affect the duration it spends for radon to move from the subsurface to the surface. When there is a huge pressure gradient due to changes in atmospheric circumstances, Rn-222 can be transported upward faster when soils of heterogeneous have many channels and cracks through which radon can outflow [170]. At that depth of 100 m from the surface, air pressure variations are difficult to influence.

When there is a temperature inversion, Rn-222 can be trapped near the earth's surface because of a colder air mass located on the ground [171].

Figure 3.2 shows the synchronous variations of radon with solar tides which are measured at the active volcanic island Terceira, Azores [172]. The author also investigated the relationship of radon activity with the lunar and marine tides, seismic and volcanic activity. For all external forces, the radon activity response was detected with different levels of confidence.

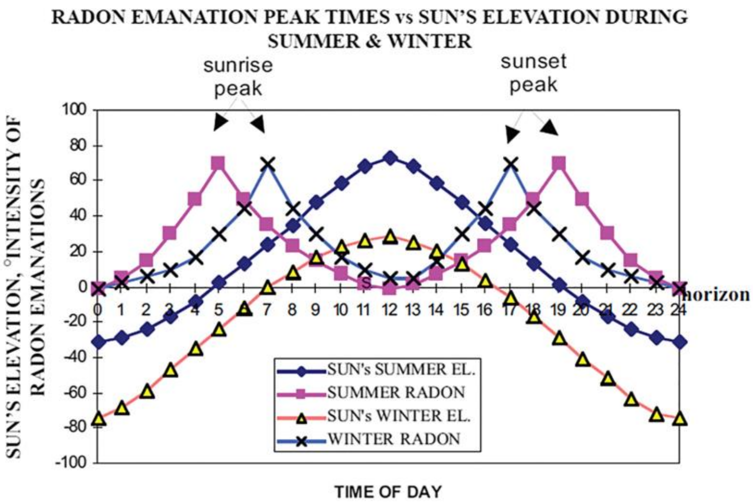

Figure 3.2. Radon emanation peak times versus the sun's elevation during summer and winter [172].

3.8. Radon Precursor as Earthquake Predictor

As a precursor to predicting earthquakes, one of the most effective tracers is radon-222. Because of its distinctive chemical properties, its transportation in environments of subsurface is mainly governed by advection, radioactive decay, and diffusion. Important data about the earth's crust's subsurface seismic activity and earthquake formation process can be provided by radon activity changes in ground water and soil gas [173–175].

Emanation of Rn-222 rates is shown to be higher in seismically active locations as well as subsurface active faults, where major channel paths for Rn-222 and gases (CO_2, CH_4, N_2, H_2, He, F, and Cl) to escape are provided. The rates at which gases escape from subsurface faults are not uniform. They are influenced by a variety of parameters such as subsurface conductivity, porosity, underlying material permeability, and so on. However, the released rupturing energy from subsurface seismic activity could change the permeability and porosity of subsurface, influencing radon channel paths. Since the 1960s, variations in geochemical, geophysical, and hydrological (crustal deformation measurement) parameters leading ahead to major earthquakes have been documented [175]. The earliest indication of a link between ^{222}Rn and earthquakes came from extremely elevated activity of Rn-222 in water from a Russian well before the April 26, 1966 Tashkent earthquake [176]. The investigation of this incident sparked dozens of new studies, and it later became a guideline in Haicheng's successful prediction. The importance of radon observations in the successful prediction of this earthquake cannot be overstated [177].

3.8.1. The Mechanism of Rn-222 Vertical Transport in Seismically Active Regions

Throughout its creation from radium's alpha decay, radon enters the pore space of soils and rock grains mostly through the process of nuclear recoil [163]. Subsurface radon was then transported to the surface by Fick's law-governed molecular diffusion and Darcy's law-governed advection flow. As mentioned in Section 3.6, The flow of Rn-222 within the earth is influenced by three factors:

(i) Convection caused by geothermal heat; (ii) the earth's pre-seismic stresses and (iii) emanation of underground gas. The geothermal gradient (~30 ° C/km) within the earth persuades fluid buoyancy, resulting in fluid flow, which leads to convection within the earth. As mentioned in Section 3.5.2, Thermally induced sub-terrestrial fluid convection in locations with higher-than-average permeability, could be a possible transport mechanism for ^{222}Rn. Gases can simply escape from the subsurface in areas with multiple active faults and fracture zones.

It is well known that locations with multiple active faults are typically quite impermeable. Before big earthquakes, the energy of rupturing released causes significant fluctuations in the porosity and permeability of the surrounding rocks close to the epicenter. As mentioned in Section

3.5.2, the effective permeability in a perpendicular channel is required for long-distance travel of Rn-222 from uranium-ore bodies to the surface of earth. The permeability fluctuation was not routinely measured during seismic activity. As a result, the amount of permeability varies during, before, and after significant seismic events has been unknown.

The Rn-222 release rates will fluctuate due to changes in permeability and porosity where seismic activity is high. The creation of micro-cracks in the aquifer system caused an irregular growth in Rn-222 concentration in groundwater; some of the micro-cracks caused a sudden fall in Rn-222 one week previous to the earthquake [150].

Mineral and hydrocarbon deposits in the subsurface have the potential to release gas, resulting in pressure gradients and an upward gas flow. As illustrated below, the mean pressure (P) produced in a homogeneous permeable medium obeying Darcy's law:

$$P = D\varepsilon\eta / k \tag{3.263}$$

where k stands for permeability, ε stands for porosity, the gas viscosity denoted by η, and the pressure diffusivity denoted by D. The viscosity and permeable medium porosity, both of which are difficult to calculate, are required for computing the pressure. Subsurface hydrocarbon deposits can be produced on a large scale to generate sufficient gas pressure. Then, by releasing CO_2, radon and other gases like CO_2, N_2, CH_4, H_2, He, F and Cl can carry away.

The influence of vertical flow on Rn-222 was measured using a 1-D model. The upright movement of Rn-222 is governed by two progressions: Fick's law-governed molecular diffusion and Darcy's law-guided gas flow. The result of Rn-222 (C, atom m^{-3}) for steady-state as a function of (−z) is obtained by Equation (3.27) using a conventional continuity equation and the standard boundary condition (Rn-222 concentration is negligible at earth's surface) [150]:

$$C = \frac{\varphi}{\lambda}\left\{1 - \exp\left[\gamma\left(\frac{\varepsilon\lambda}{D}\right)^{1/2} Z\right]\right\} \tag{3.27}$$

where

$$\gamma = \frac{v}{2(\varepsilon\lambda D)^{1/2}} + \left(\frac{v^2}{4\varepsilon\lambda D_{eff}} + 1\right)^{1/2} \tag{33.28}$$

where v denotes the apparent gas flow velocity in the soil, The volumetric radon emanation rate is denoted by φ, ε is porosity of soil, λ, the decay constant of ^{222}Rn and the effective diffusion coefficient of Rn-222 is D_{eff}. Equation [17] describes the the coefficient of effective diffusion and molecular diffusion (D_0):

$$D_{eff} = \varepsilon\tau D_o \tag{33.29}$$

The theoretical radon activities calculated using Equation (3.27) and plotted in **Figure 3.3** can be compared to values obtained several meters apart at different depths. It appeared that during anomalous periods ^{222}Rn concentration elevated at the shallower depths only.

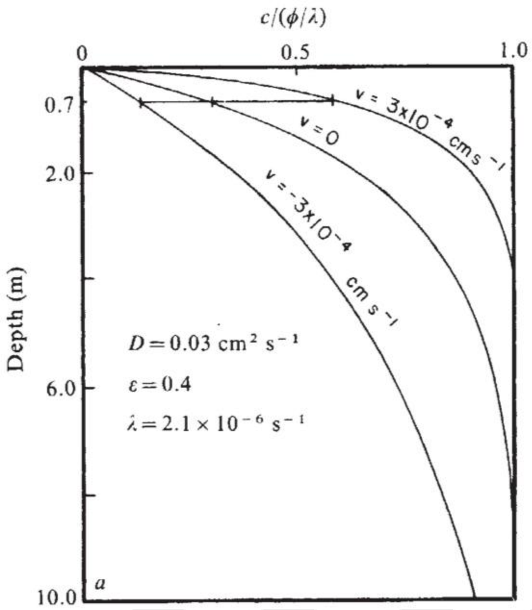

Figure 3.3. Theoretical model of Rn-222 in subsurface soil as a function of -Z [4].

3.8.2. Radon Activity Monitoring on a Long-Term

In order to predict earthquakes, long-term monitoring of Rn-222 activity in soil and groundwater is basic. Many countries along plate boundaries, including Türkiye, China, Japan, India, Russia, and the United States, have continuous monitoring programs in place. Continuous monitoring of groundwater and soil processes is essential for earthquake prediction, as is a thorough understanding of other parameters that influence Rn-222 near the earth's surface. For instance, radon sampling at 10 m depth for 15 minutes at a monitoring station in Himalayan revealed a complicated pattern with high seasonality and diurnal trends [178]. The results of a large number of monitoring wells around the San Andreas fault zone showed the greatest regional variability, by four orders of magnitude, with no systematic spatial trend [179]. There was no evidence that these fluctuations were linked to underlying seismic activity.

Main geophysical phenomena, like seismic events and volcanic eruptions, are proven to cause considerable radon concentration changes in the soil. **Figure 3.4** depicts radon measurements in soil air near the Tuzla fault line in Türkiye between 2007 and 2011, with (338 ± 38 kBq m^{-3}) average concentration [180]. Because of the high seismic activity in this location and the nearby fault lines, the observations of this monitoring station showed multiple anomalies [180]. Radon concentrations were also observed along Türkiye's NAF extremely active fault, with radon activity reaching 200000 Bq m^{-3} according to [80].

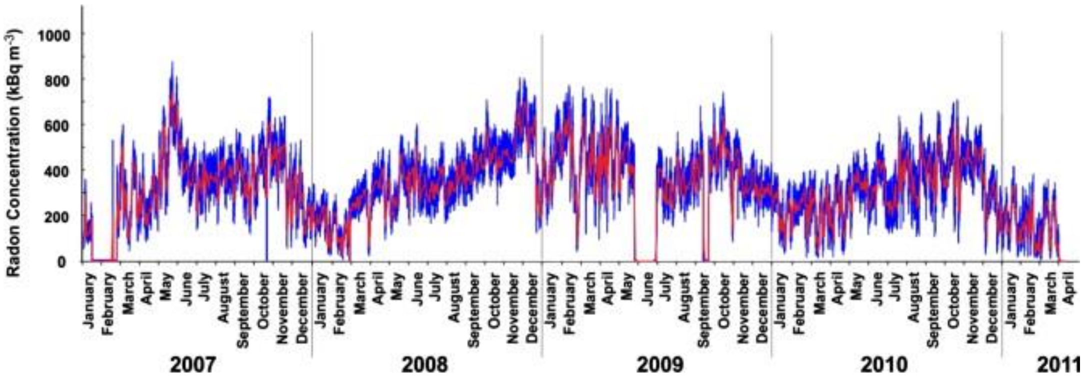

Figure 3.4. Radon-222 measurements in the Tuzla fault line were taken between 2007 and 2011 (around 80 kilometers southwest of Izmir, Türkiye). Because of the seismic activity in this location and the fault lines nearby, this data showed several anomalies [180].

Table 3.4. The comparison of ^{222}Rn activities in soil-gas samples from several tectonic regimes [181].

Nation	Range of Radon-222 (Bq/m^3)	Studied by
Türkiye	209–7389	Erees et al. (2006) [182]
Türkiye	4300–9800	Inceoz et al. (2006) [112]
Türkiye	98–8594	Tabar et al. (2013) [181]
Jordan	800–26700	Abumurad and Al-Tamimi (2005) [183]
Russia	1700–24000	Iakovleva and Ryzhamova. (2003) [184]
Ghana	9910–42100	Amponsah et al. (2008) [185]
Cameroon	5500–8700	Ngachin et al. (2008) [186]
India	1657–1855	Chaudhuri et al. (2010) [187]
India	1500–15900	Choubey et al. (2007) [188]
Canada	6800–74700	Chen et al. (2008) [189]

Long-term predictions have been improved over time, particularly in locations where major earthquakes occur near plate borders and in inland areas. Data from trench studies of active faults and historical earthquake geodetic survey data were collected over a 100-year period, indicating that significant earthquakes occur often in many regions.

Long-term monitoring offers real-time observations, providing insight into crustal deformation. As illustrated in **Table 3.4**, relationships among micro-seismic occurrences and reported ^{222}Rn anomalies were investigated in order to link anomalous ^{222}Rn to earthquakes.

4. IONOSPHERE

The ionosphere is defined as the upper region of the atmosphere that contains sufficient electrons and ions to make interaction with electromagnetic fields effectively. Like a conducting medium, it is subjected to plasma physics laws as a partially ionized gas, and it is important for the global electric circuit. Because of its electromagnetic characteristics, the ionosphere makes interactions with and is governed in part by the Earth's magnetic field. As a result, magnetoactive plasma was meant to describe the ionosphere.

The ionosphere's altitude borders are currently estimated to be between 50 and 1000 kilometers. For all levels of the ionosphere, **Figure 4.1** depicts the altitude structure of the ionosphere and the ionization main source [190].

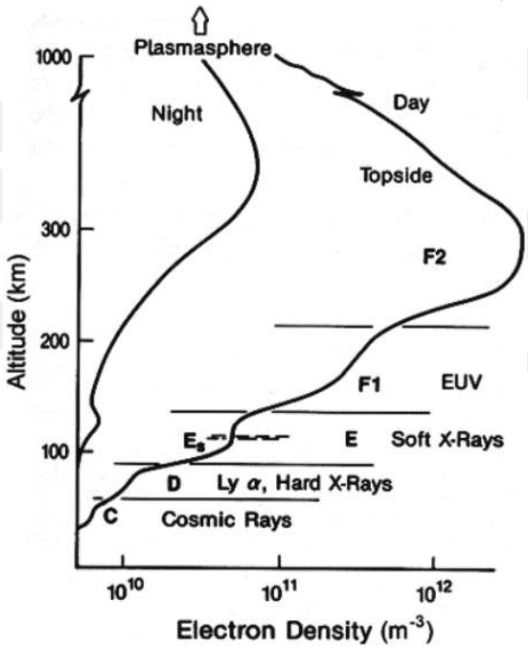

Figure 4.1. The main ionization areas and the structure of the ionosphere during a night and day of summer (middle latitude) [190].

Solar UV light has a shorter wavelength of 102.7 nm causes ionization in the ionosphere, which is successfully taken by atmospheric molecules. Solar cosmic rays at high latitudes are further sources of ionization, but they are sporadic and linked to solar activity. Based on the day time and geophysical circumstances, layers of ionospheric can be divided into two or more, which is why the ionospheric area and layer are distinguishable as indicated in **Table 4.1** [191].

Table 4.1. Regions and layers of the ionospheric [191].

Zone	Approx. Altitude Range (km)	Layer	Approx. Altitude (km)	Approx. Electron Density-Daytime (m^{-3})
C			65	10^8
D	50-90			
		D	70-90	10^9
		El	100-110	10^{11}
E	90-140	E2	115	10^{11}
		E_s	110-120	variable
		F1, $F1^{1/2}$	140-200	$2x10^{11}$
F	140-350	F2	200-350	10^{12}
Topside	350-1000			10^{10} 10^{11}
Plasmasphere	>1000			10^9

4.1. Ionospheric Regular Variations

Fluctuation of ionospheric can be subdivided on a variety of temporal scales, with the biggest temporal scale associated with the solar activity cycle. Although there is a cycle of 11-year, which is the number of visible dark spots on the solar disk using a telescope, there are several manifestations of solar activity, including ejections of coronal mass (CME), solar flares, and solar proton events. In geophysics, solar activity is measured by the solar radio flux with a wavelength of 10.7 cm, as shown in **Figure 4.2**, the critical frequency (top panel) was shown to be strongly linked to solar activity. This demonstrates that as solar activity increases, the critical frequency's absolute daytime value rises [192].

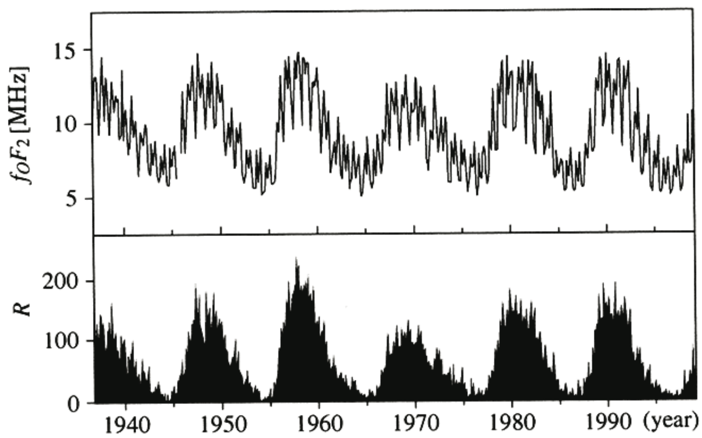

Figure 4.2. Solar activity (60 years), the solar cycle fluctuations (top) and solar 10.7 radio flux (bottom) [192].

Seasonal fluctuations, as shown in **Figure 4.3**, are the next temporal scale in ionospheric variability. The seasonal effect was seen in the maximum about the equinoxes and the minima in the summer for the noon values. However, when solar activity decreases, the seasonal effect's amplitude decreases. There is a change among the Southern and Northern hemispheres at the solar cycle minimum. The fall equinox maximum vanishes in the Southern hemisphere. The seasonal behavior of midnight is pure, but it contains a reversal of the solar cycle's seasonal dependence.

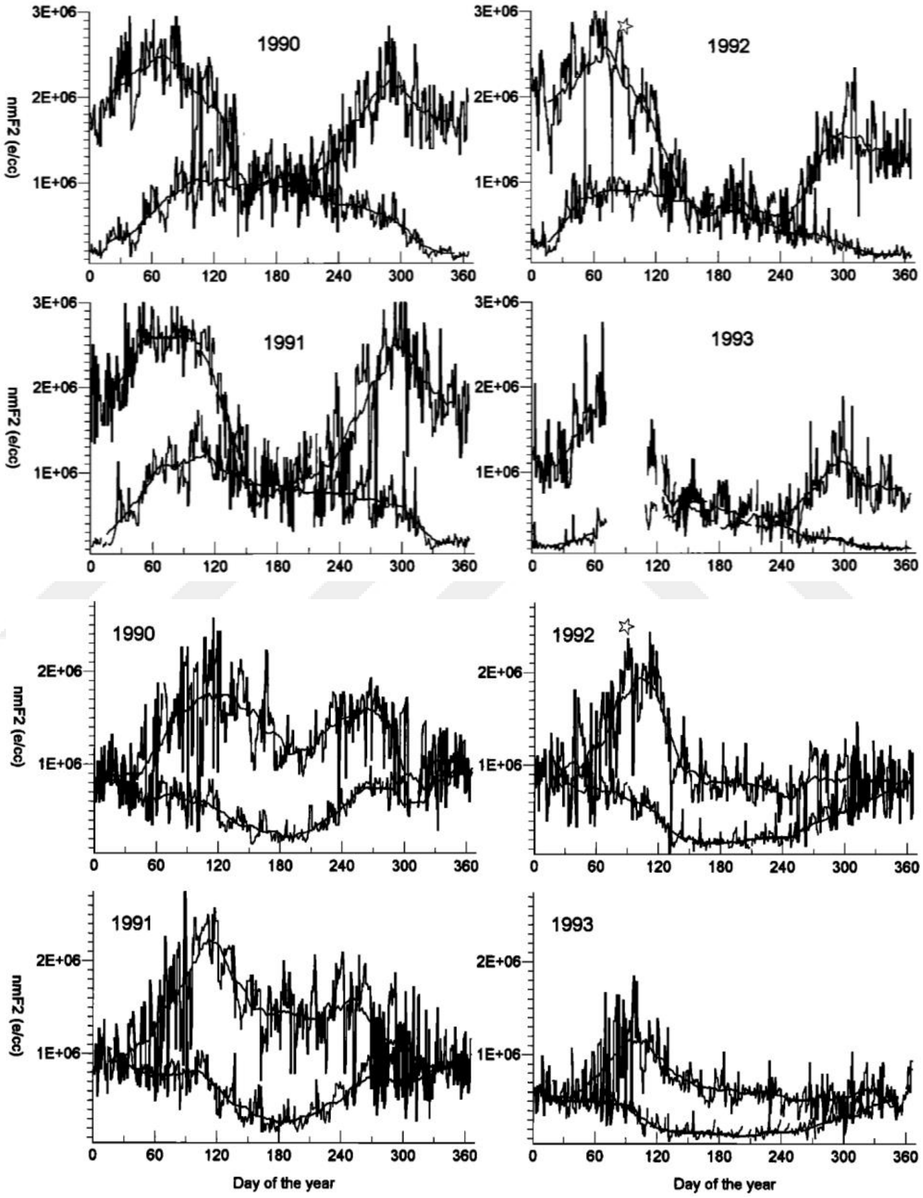

Figure 4.3. The values of the electron concentration at noon (upper) and midnight (bottom) for 4 years of the 22nd solar cycle (upper two plots) for Tokyo and Canberra (bottom two plots) (two bottom plots). Daily meanings are overlaid with a 30-day running mean [193].

The daily variations are the smallest temporal scale regularly changes. In **Figure 4.4**, the typical daily fluctuations for undisturbed states were displayed. In different areas, daily changes of the critical frequency might be unlikely. The daily variations in the ionosphere have their own unique features. The day-night oscillation is the most obvious example of wave-like fluctuation.

Day-to-day fluctuation is the most interesting features, as it shows a large variance without any obvious cause.

As seen in **Table 4.2**, the differences among ionospheric changes in the time of magnetic storms and seismo-ionospheric fluctuations,

Table 4.2. Variations in ionospheric by the magnetic storm and seismo-ionospheric variables [36].

Fluctuations in the ionospheric (magnetic storm)	Variations of Seismo-ionospheric
Variations are seen all across the world and have a global character.	Only in the domain of earthquake preparation do variations appear (with some shift equatorward)
The magnitude and duration of the variations are significant, and they comprise a continuous process that lasts 40-48 H.	Variations are sporadic in character and arise at the same time every day in the same location, but they do not have a continuous property.
Disturbances in low latitudes are primarily detected at night, with positive and negative phases observable, first and foremost between sunset and sunrise.	Fluctuations are also seen in day, with negative deviation in the afternoon hours being the most statistically validated predictor in low latitudes.
The Δh_mF2 value in the time of a storm is (60 to 80 km) with h_mF2 in quiet day not less than 250 kilometers	The Δh_mF2 prior to earthquakes may reach 150 kilometers
Because the mass relation ($[N_2] + [O_2]) / [O]$ increased as a result of the formation of a storm, the mean molecular mass at Flayer altitudes increased. Due to an increase in the NO^+/O^+ relationship, the average mass of ions in the time of the storm has also increased.	Because of fluctuations in magnetospheric fluxes of ions O^+ and increases in concentration of light ions (H^+ and He^+), seismo-ionospheric fluctuations result in a decrease in average mass of ions at F-layer heights.
During a magnetic storm, the positive and negative deviations are determined by the storm's development phase.	Negative and positive deviations of seismo-ionospheric variations are dependent on LT, relative location of observation point and epicenter, and sign of electric field anomaly.
During storm, electrons and ions are heated to high temperatures (2000 – 3000 K)	Before earthquakes (~ 300 K), there was almost no heating.

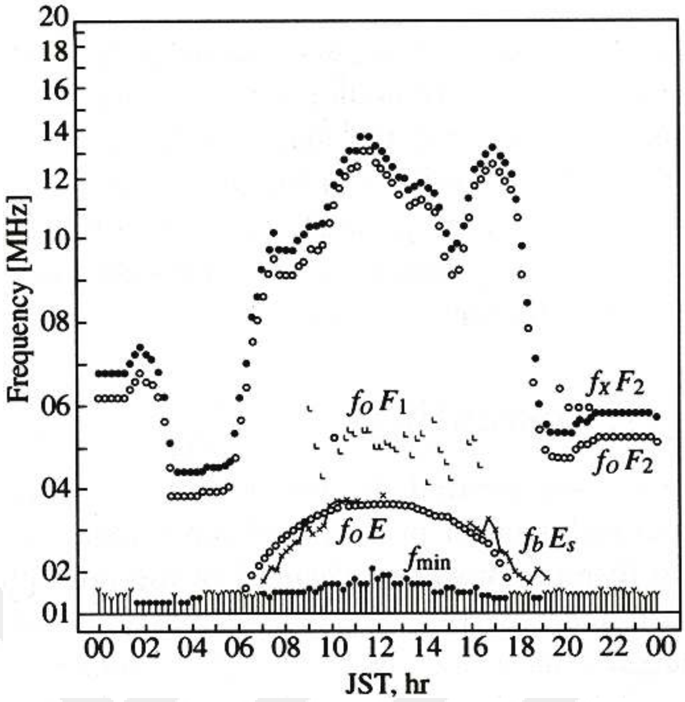

Figure 4.4. f_OF_2 with other characteristic frequencies scaled from the ionogram show typical daily fluctuations [194].

4.2. Ionospheric Precursors to Predict Earthquake

The first seismo-ionospheric coupling mechanism was the acoustic-gravity wave [125,195]. The post-earthquake influence was proved by comparison of seismograms and ionosonde records, reflecting the vertical oscillation of the ionospheric layer caused by the earthquake's acoustic vibrations. However, it should be noted that the effects were also identified before the earthquake [121,122].

The shape, duration time, amplitude, and time of appearance of the registered precursors on the ground vary by sign and other factors, such as their shape, duration, and time of appearance prior to the earthquake [36]. The ionospheric precursors provide a very realistic prospect time: from 1 to 7 days, not years, months, or weeks. This is a significant benefit of ionospheric precursors.

Separating the precursor is a pattern identification art that includes the signal choice technique against a noisy background. As a result, different techniques for varying amounts of ionospheric variability can be applied in different geophysical settings.

The following are the main properties of ionospheric precursors: [36]:

- The plasma density was influenced by seismically produced precursors, which were detected among 7 d and a few hours before the seismic event.
- Fluctuation might be either positive or negative.

- A seismically produced deviation of sign has a very short duration of approximately 4-6 h which is opposite to magnetic storm effects, in which a very strong seismic event can last for over twelve hours.
- The size of the preparation zone determines the threshold at which seismo-genic influences on the ionosphere will be noticeable, which matches to a magnitude of 5.
- Typically, seismo-ionospheric changes have the similar amplitude as an ionosphere's day-to-day fluctuation (30%), although they can be much more noticeable (up to 100%) at specific times in local time.
- Local time determines the shape and sign of seismo-ionospheric fluctuations. This dependence may vary by longitude and latitude, necessitating more investigation for each geophysical area.
- The form and sign of seismo-ionospheric fluctuations in one-point observations are determined by the relative location of the observation and the epicenter.
- The range of the ionosphere's influenced area at the maximum of the F- layer relies on the size of the seismic event, and for all major earthquakes with M>7, it can exceed 40 degrees in longitude and latitude.
- Seismoionospheric changes have an influence on plasma, causing the ionosphere's height scale to grow.
- Changes in ion mass or parallel particle fluxes are the main causes of height scale fluctuations. They aren't due to fluctuations in plasma temperature.
- The measured variances in the critical frequency correspond well with the TEC seismo-ionospheric fluctuations.
- In the magnetically conjugated region, the related ionospheric effects can be recognized under certain conditions.
- Seismo-ionospheric changes cause modification of equatorial anomalies at equatorial and low latitudes.
- Several days prior to the earthquake, increasing sporadic E-layer activity was reported across the earthquake preparedness zone.
- Several days before the earthquake, growth of D-region ionization was noticed over the seismic preparedness area.
- Inside the magnetic tube that was loaned to the preparation zone, precipitation of energetic particles was noticed.
- Inside the magnetic-tube loaned to the preparation region, a higher concentration of light ions was found.

4.2.1. Effects on F_2-Region of Ionosphere

Influences from long-term causes, e.g., tectonic faults, were studied [196]. This research was done to understand data from the Intercosmos-19 satellite's topside sounder, which recorded large longitudinal fluctuations when traveling over the Andes [197]. At three constant latitudes, longitudinal profiles of electron density and critical frequency at a height of 400 km were calculated. For 25° S latitude, the critical frequency was shown in **Figure 4.6**.

The tectonic plate margins contain a large network of tectonic faults that "lives", implying that ionosphere changes can be formed continuously as well. The GPS receivers can keep track of small-scale changes of the ionosphere. **Figure 4.5** illustrates differences among worldwide seismic activity centered on lengthways tectonic plate margins with the ionospheric phase variations for global distribution as measured by the GPS receivers' network.

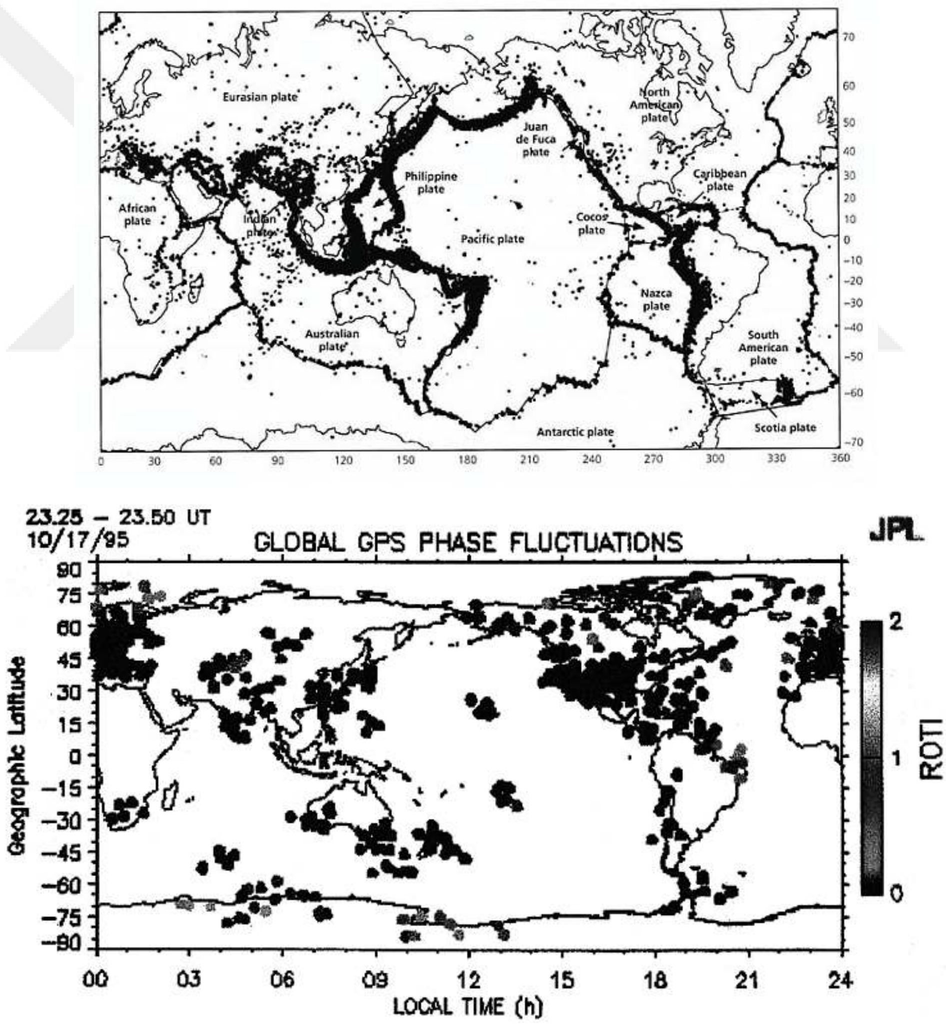

Figure 4.5. Seismic activity for Global distribution of (upper), global distribution of GPS receivers signal phase variations produced by the small-scale irregularities (lower) [36].

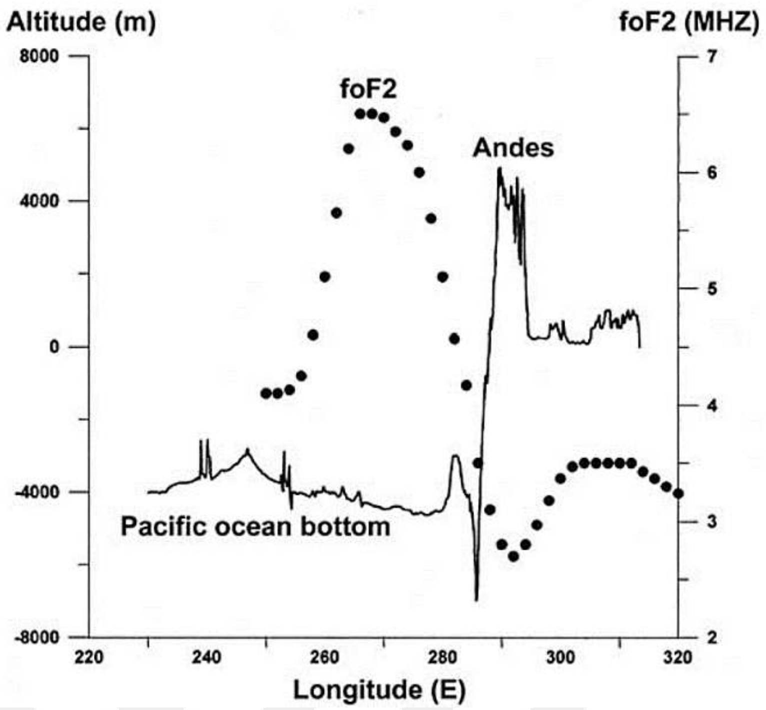

Figure 4.6. Longitudinal distribution *foF2* (*dots, right axis*) (July 15th–16th, 1980, 05:00 LT) and ground level data (*line, left axis*) [36].

4.3. Role of Radon in Seismo-ionospheric Coupling

Natural radioactivity acts as a critical influence in the morphology of the atmosphere, the calculation of global electric circuit variables as well. Electromagnetic radiation or a flux of rapid charged and neutral particles indicate the release of the nucleus of radioactive substances. By traveling within the atmosphere, radioactivity supplies the energy for excitation and ionization of molecules.

4.3.1. Ionization Production

Natural radioactivity and cosmic-rays are the primary sources of ionization in the lower atmosphere. Radiation of the ground was responsible for more than 60 percent of the overall production of natural ionization bases.

In air, ^{219}Rn (Actinon), ^{220}Rn (Thoron) and ^{222}Rn (Radon) are the primary sources of α-particles that represent a helium nucleus with a charge of $2e$. Isotopes of heavy metals, in particular, are produced as a result of their disintegration, and they are promptly absorbed by aerosol particles. The released energy of particles is between 4 and 9 MeV, and the free pass length is less than 6 cm. For instance, α-particle produced in Rn-222 decay with a mean energy of E_α=6 MeV can yield ~2x10^5 electron-ion pairs in atmospheric air. The radon flux produced on the Earth's surface is typically less than (1.4 atom/cm^2/s) [198]. However, in some regions, such as geo-active zones near

Earth's crustal cracks, radon emanation from the ground might be significantly higher. Fast electrons with an average energy of ~0.25 MeV and a free pass in air of ~1 m is produced by β-emitters. They are created by the disintegration of ^{85}Kr in the air, as well as ^{90}Sr and ^{90}Y on the Earth's surface. Essentially, γ-radiation is the product of the decay of radium and thorium.

Ions are produced in an atmosphere near the Earth's surface by cosmic radiation, which is produced by the sun's usual activity. At an altitude of 20–35 kilometers, velocity of ion production increases from ~2 $cm^{-3}s^{-1}$ to 5$cm^{-3}s^{-1}$. However, following severe solar flares, generation of ions in the atmosphere increases due to corpuscular radiation [199].

4.3.2. Near-Ground Atmospheric Electric Field

In the list of physical precursors of short-term, the electric field anomaly as precursor coexisted with Rn-222 release at all times [142]. Many articles suggest that Rn-222 release fluctuates conductivity of air and then affects the atmosphere electric field which can be found in relation to the influence of radon.

The link between Rn-222 and changes in the *foF2* near Tashkent about the time of the Nazarbek seismic event (M = 5.1, 11th December 1980) sparked the first hypotheses [76]. This link was discovered exclusively for values of the *foF2* collected at particular durations of LT, implying that the observed effect is LT dependent.

Variations in Rn-222 concentration (triangles) were detected at a well not far from the epicenter of the earthquake in **Figure 4.7**. Two additional curves depict smoothed (running average) fluctuations of f_oF2 scaled over numerous months for two specific LT periods. There is a clear anticorrelation between two processes: In the area of the earthquake, Rn-222 concentration rises a few days before the earthquake, while Rn-222 concentration in the morning and afternoon hours slowly lowers.

As depicted in **Figure 4.8**, the process of generating abnormal electric fields prior to big earthquakes. The parameters of the neighboring ground layer are strongly altered by Rn-222 release from the crust, as shown in **Figure 4.9**. Within the layer, it can modify the electric field value numerous times, up to the electrode effect's opposite sign. The ionization efficiency of Rn-222 and its daughter products might be ten times that of cosmic rays [200], which are able to affect the thunderstorm activity [201,202]. There's also the effect of surface roughness on the fluctuation of the electric field near the ground. The parameters of seismo-ionospheric coupling can be categorized into three categories in **Table 4.3**.

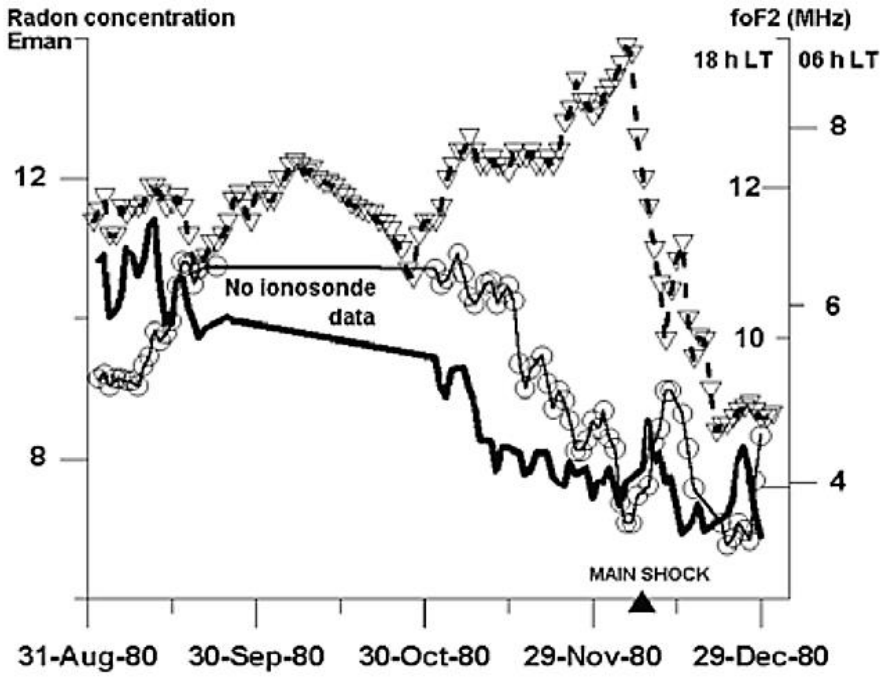

Figure 4.7. For the Tashkent ionospheric station, correlation among Rn-222 in the well near the upcoming epicenter (*triangles*) and the average for 5 days of f_oF2 scaled for 06:00 local time (*bold*) and 18:00 local time (*circles*). The *bold triangle* on the diagram depicts the time of the seismic event [76].

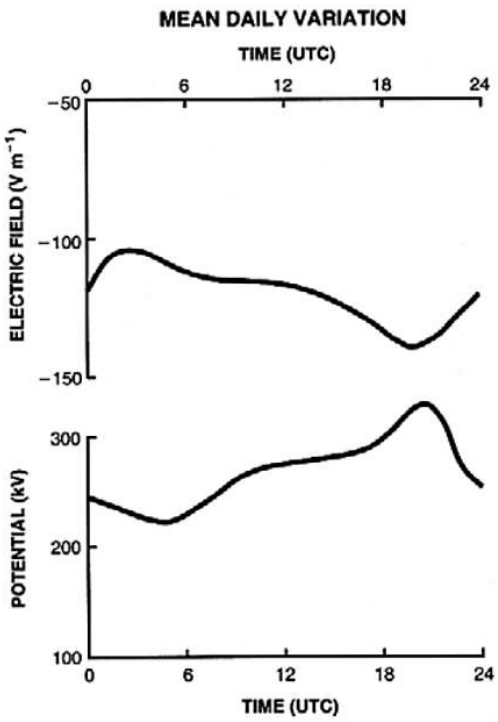

Figure 4.8. The atmospheric electric field's main diurnal variation (top panel). Negative numbers indicate that the electric field is pointing downward. The potential of the ionosphere as measured by balloons (bottom panel) [203].

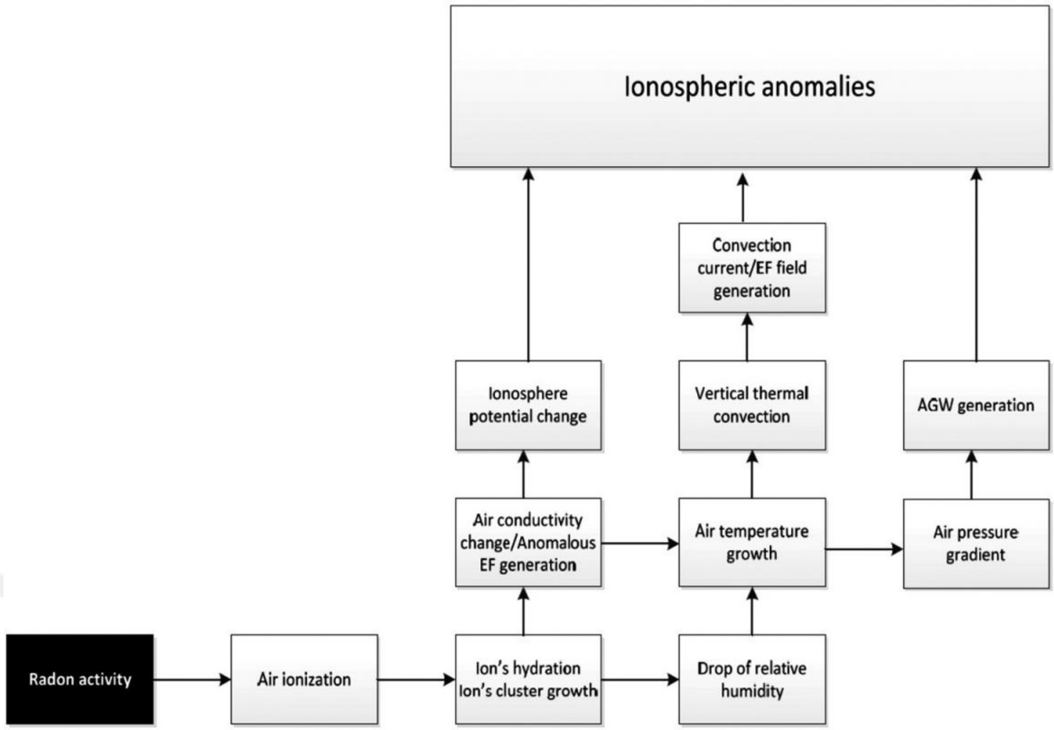

Figure 4.9. Effect of radon emanation on the geochemical/electromagnetic parameters [204].

Table 4.3. Parameter list of Earth and space data [204].

	Parameter	Instrument	Platform	Methodology	Products
Ionosphere	TEC variations	GPS/TEC	IGS	quartile-based approach 15 day mean	Variations in space plasma and TEC
	Ionospheric variations	Langmuir Probe (LP)	DEMETER	Ionospheric perturbation detection	
	Electrical field and plasma	LP, AC/DC	NASA C/NOFS		
	Electron density profiles	Occultation GPS	FORMOSAT3/COSMIC	Radio Occultation technique	Vertical profiles of ionospheric electron density
Low Atmosphere	VIS-NIR Earth radiation	MODIS, SEVIRI MTST	EOS TERRA, AQUA GMS MTST MSG/SEVIRI	Cloud detection	Identified anomalous cloud shapes
	SWR: Surface Latent Heat Flux	NCEP Ensemble Products	NOAA NCEP-NCAR CDAS	SLHF anomalous variations	SLHF anomalies
	LWR: Outgoing long wave radiation	AVHRR AIRS	NOAA EOS AQUA	Detection in transient OLR field	OLR change detection
	Atmospheric chemical potential	NASA Data Assimilation	GEOS-5, MERRA	Time series data analysis	Maximum in ACP
Litho-sphere	Radon flux	Alpha, Gamma	US-CA; Italy, Taiwan, Greece, Turkey, Japan	Time series data analysis	Anomalous counting rate of radon flux

The effects of aerosols are another important factor. The atmospheric electric field in rural areas polluted by aerosols is up to four times greater than in clear air, according to experimental observations [205].

Many precursors were discovered after analyzing the destructive earthquake in Irpinia, Italy, with a magnitude of 6.9. The following are some of the observed precursors [36]:

- Rn-222 anomalies began post to the seismic swarm in May 1980 and lasted until the Irpinia seismic event, which was reported at great ranges from the epicenter.
- Thermal anomalies began five days prior to the seismic event and spread across vast region (> 500 kilometer)
- Ionosondes in Athens and Rome observed ionospheric anomalies two and one days before the seismic earthquake, respectively.
- The Intercosmos-19 satellite began recording ionospheric anomalies three days before the event.
- The ion mass changes were manifested as scale height anomalies.
- Three days prior to the seismic event, VLF noise anomalies began.

Another recent major earthquake event is the seismic sequence (M6.3 Norcia, M 6.1 Macerata and M 6.5 Perugia) of 2016 Central Italy, which became one of the most important and unusual modern earthquake events [204]. Recently, studies show an enhanced coupling between the atmospheric boundary layer and the ionosphere, which has been proposed to be linked to large (>M6) earthquakes.

The scenario of the events' progress can be characterized based on the data obtained on the Irpinia seismic event precursors. The development of neutral associates and radon emanation prepared the lower atmosphere over several months. Gas discharges began around five days before the earthquake across the entire Apennine peninsula, which were detected by satellite as thermal anomalies. The gas aerosols boosted the electric field strength, resulting in the formation of a strong electric field and the disruption of neutral companions that could penetrate into the ionosphere [36].

4.4. Ionospheric TEC

The collective number of electrons in the slab from the satellite to the receiver is known as the Total Electron Content (or TEC). Because the F_2 layer contributes the most to TEC, the TEC variations are often quite similar to the f_OF2 variations. In other circumstances, their behavior is antiphase due to the plasmasphere's higher contribution to TEC, such as during geomagnetic storms. According to [206], the correlation between fluctuations in N_mF2 and TEC(GPS) is 0.953. As a result, GPS TEC data can be used as if it were ionosonde observations, specifically for plotting. In comparison to single receiver time series analysis, **Figure 4.10** illustrates the benefit of having many GPS receivers in the area. The time series of total electron content at L'Aquila GPS (red) was displayed from top to bottom, along with the running average (blue). The percentage change (ΔTEC) among the real values of TEC (GPS) and the monthly median may be seen in the second graph from the top. A strong positive TEC anomaly can be seen in the figure a few hours prior to the seismic event. The third plot from the top illustrates that the local spatial scintillation index has a higher sensitivity than the GPS TEC time series analysis in detecting pre-earthquake anomalies in the ionosphere, since the anomaly appears before in TEC.

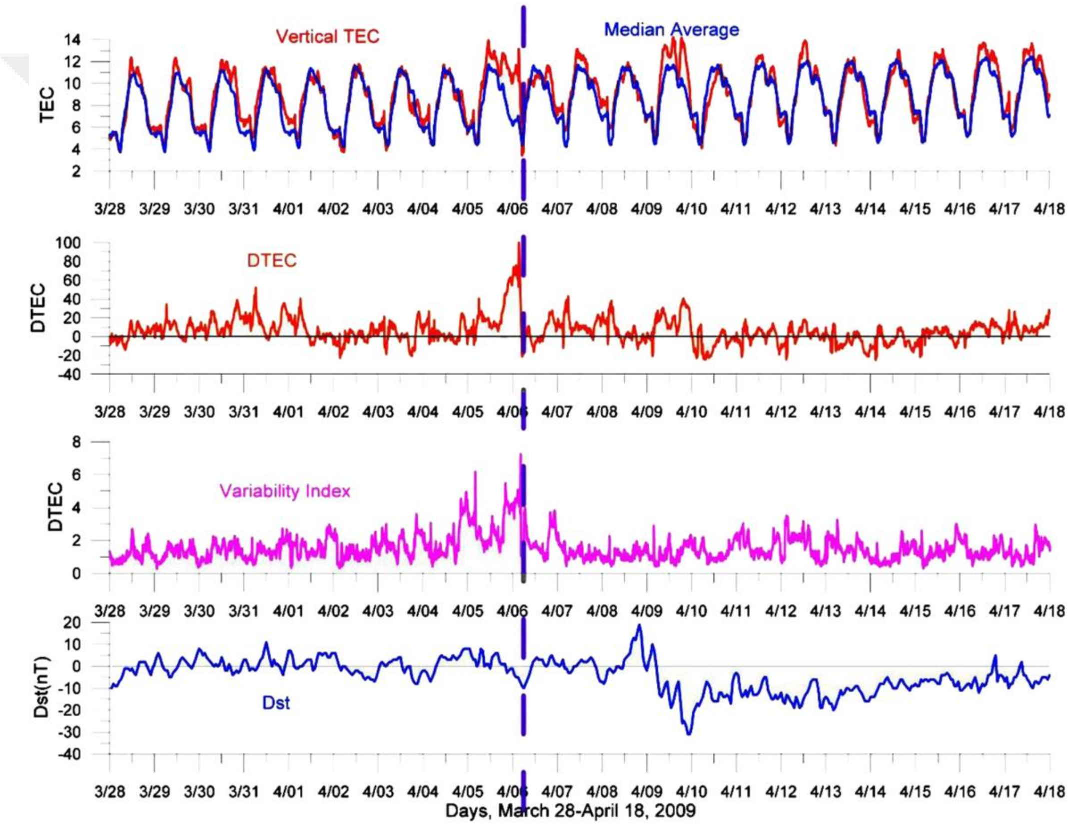

Figure 4.10. (1) The vertical TEC time series is represented by the red line, the aqui GPS receiver is represented by the blue line, and the running average is represented by the blue line. (2) Difference between the total electron content and the median instantaneous values (percent). (3) The LSSI was derived using observations from the GPS receiver network-Italian. (4) Dst, or the global equatorial geomagnetic activity index. The time of the major shock on April 6, 2009 is indicated by the blue vertical dashed line [207].

The global geomagnetic index Dst, shown in the fourth graph from the top, was used to distinguish between seismically produced ionospheric anomalies with geomagnetic disturbances. The period leading up to the L'Aquila seismic event was quiet, however on April 8, a tiny geomagnetic storm occurred.

The ionospheric precursor mask is possibly the advanced and sensitive technology for observing precursors [208], There is a specific representation of the total electron content (color coded) in coordinates: X-days relative to the main shock day, and Y-the local time, which was presented in **Figure 4.11** for the example of L'Aquila. After years of research into powerful M⩾ 6 earthquakes in Greece, it was discovered [209], a positive anomaly occurred above the preparation area at the night time 1-3 days before to an earthquake. This effect was discovered to be effective for all M > 6 seismic events, and it was linked to the physical mechanism of anomaly formation [210]. In **Figure 4.11**, the prototype mask designed for the L'Aquila earthquake was displayed. Starting six days before the earthquake, positive anomalies were reported in the afternoon and morning hours.

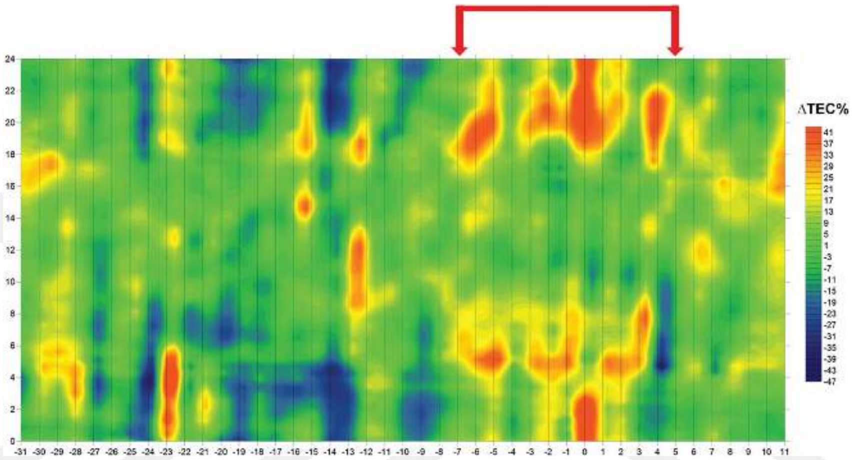

Figure 4.11. L'Aquila earthquake's precursor mask. April 6, 2009 is Day 0 on the x-axis [210].

It's crucial to notice that anomalies don't go away right after the main shock; they stick around for a few days afterward, and the period of anomaly appearance matches the [211]-detected 'foreshock period'. Using spatial distribution, the TEC (GPS) anomaly 1 d prior to the major shock is depicted in **Figure 4.12** using observations from the GPS receiver network in Italia.

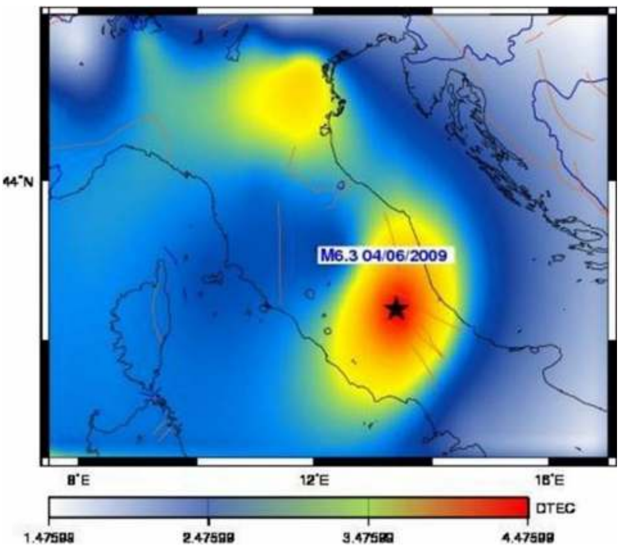

Figure 4.12. The GPS TEC residual map (ΔTEC) 1-day prior to the earthquake of L'Aquila with 6.3 M (6th of April, 2009) [207].

Several various circumstances should be satisfied by the mechanism of atmospheric anomaly development (time of ionization, plasma-chemical reactions, etc.). The inertia of thermodynamic and atmospheric progressions does not ensure that all precursors respond instantly. Furthermore, any quantities are discrete in nature; for instance, an ionosonde in standard mode will sound once every 15 minutes. GPS receivers provide more efficiency chances, with GPS TEC computation rates ranging from 2 minutes to 5 minutes and beyond. As a result, there is no guarantee that TEC will be accurately measured at the time of the major shock. However, a co-seismic signal was apparently collected in the case of L'Aquila, as illustrated in **Figure 4.13**.

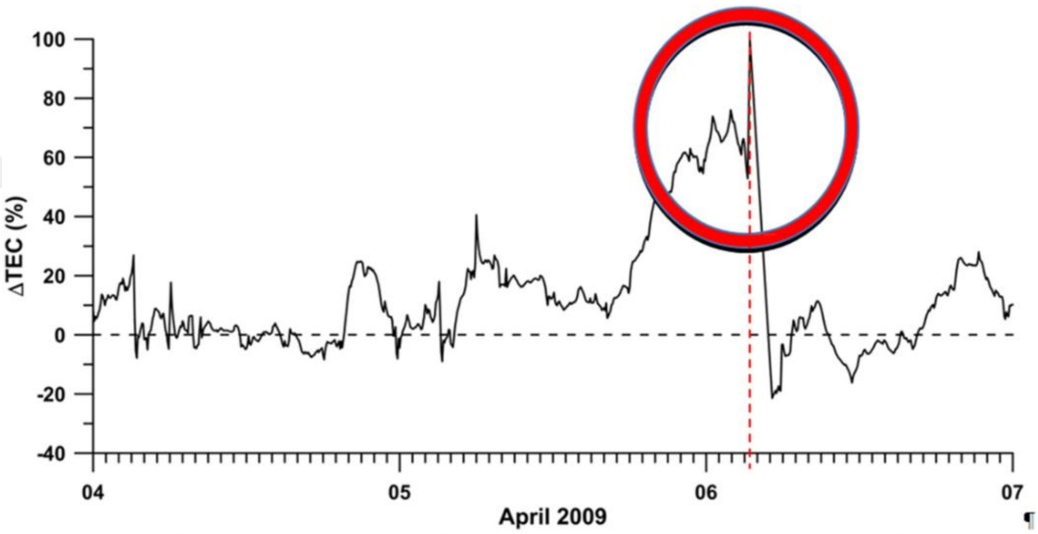

Figure 4.13. The aqui receiver produced a coseismic ionospheric indication (in the red circle) [207].

Important progress has recently been made in the growth of unique ionospheric observation operating algorithms for detecting earthquake ionospheric precursors [36,64]. The first was based on a basic principle: a station located nearer to the epicenter of an upcoming seismic event 'feels' the approaching more compared to the one located distant.

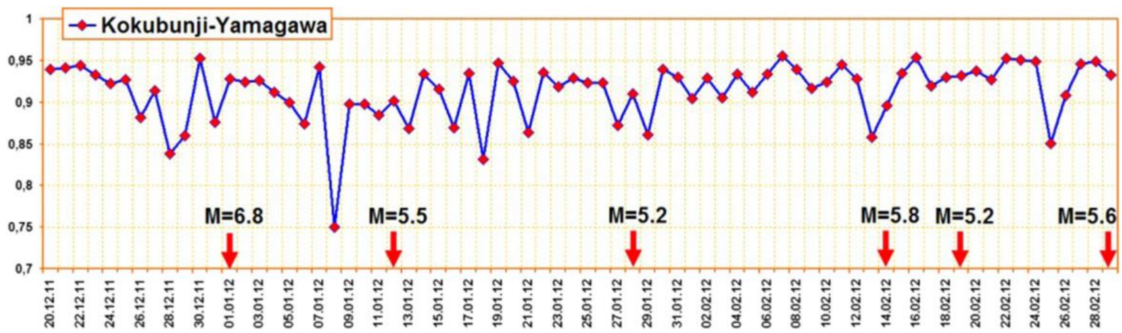

Figure 4.14. Cross-correlation analysis of the critical frequencies f_oF2 measured at Kokubunji and Jamagawa ionosondes for the period from December 20, 2011 to February 29, 2012 [207].

Calculating the cross-correlation coefficient between daily f_OF2 records for total electron contents for GPS receivers revealed this [65]. It can be observed from **Figure 4.14** and **Figure 4.15**, before earthquakes, there is a remarkable reduction in the value of the coefficient of cross-correlation one or several days prior to seismic events.

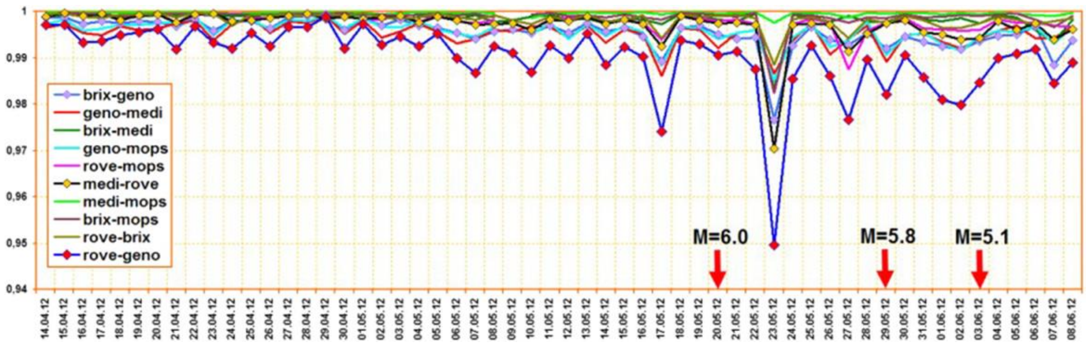

Figure 4.15. Variations of the cross-correlation coefficient before a series of quakes in Northern Italy in 2012 for the period from April 14 to June 8, 2012 [207].

5. DATA AND STUDY AREA

This chapter includes the study area and the information about data sources as well the nature of the data explored by figures. Also, the transformations of the data highlighted for specific data. Moreover, we focused on data preparation to obtain suitable and correct results.

5.1. Study Area

North Anatolian Fault Zone (NAF) was described by Ketin in the late 1940s [135], It is currently one of the world's greatest active continental strike-slip faults. The fault originated in response to the Arabian Plate's northward drift in the east and the Hellenic subduction zone's southward rollback in the west [212]. The Fault Zone of North Anatolian is known for the highest seismicity region in the world, and has caused many large and destructive earthquakes.

Reşadiye geothermal area located on the line of NAF. This geothermal area is related to the region's geological structure. The topsoil is made up of rocks, silt, sand, limestone, and andesitic volcanic rocks [213]. The town of Reşadiye was also surrounded by places where surface ruptures formed during the 1939 Erzincan Earthquake (Ms = 7.8) as shown in the **Figure 5.1**.

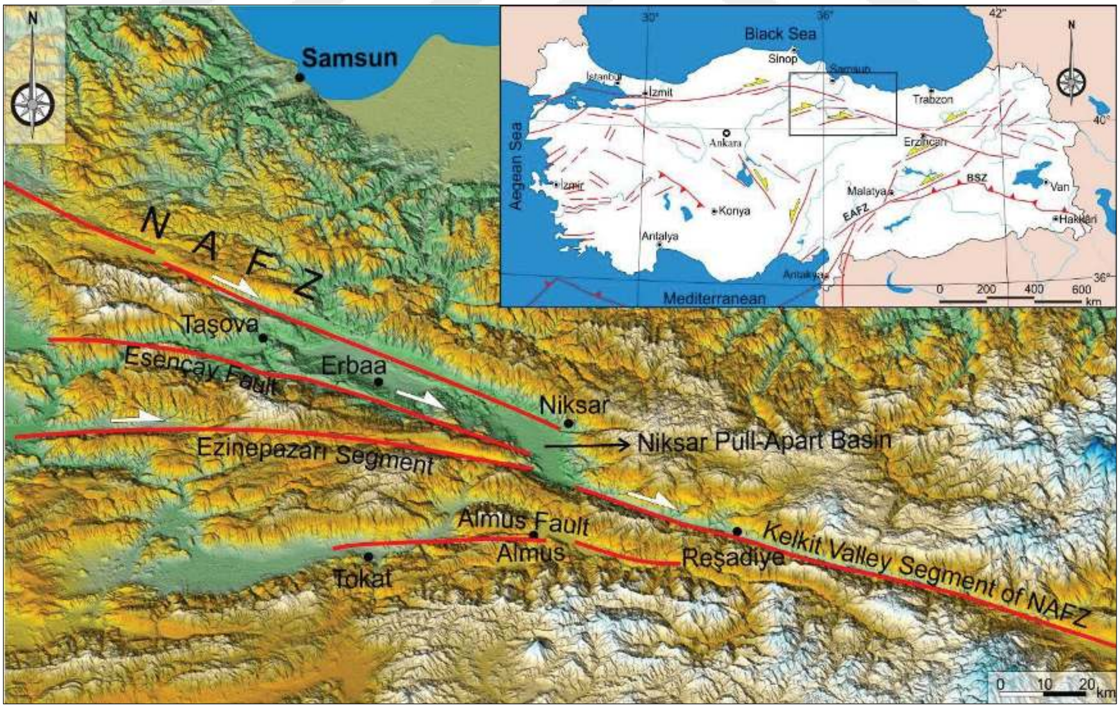

Figure 5.1. Allocation of active faults around Reşadiye [214].

5.2. Data Sources and Explanations

In this study, we used a lot of data for the purposes of investigation from different sources. Then some of them required to be formatted, sorted, resampled, and interpolated. As well, filtered data obtained for certain conditions for the purpose of investigation. It is also important to know which data at which time interval is significant to make the proper investigation, otherwise it will be useless or inaccurate. Likewise, for some of the data we need the precise time interval in order to learn the instantaneous behavior of the variable which may be linked to another parameter.
We would also like to express that the missing values in the range of the data when it is used makes it difficult to explain a proper cause and effect. For some data, we tried to decrease the level of difficulty by interpolating and resampling data, for some it is okay but still it remains as weak for interpreting the results for some data. In this section, graphically we clarified this.
Moreover, it is very important to select correct parameters when the data is obtained from the online sources. Because of using different sources for each data, may someone forget the concept of local and universal time (Türkiye Time = UT+3 hours). The data which used in this thesis categorized as the following subsections.

5.2.1. Earthquake Data

The earthquakes used in this thesis were taken from B.U. KOERI-RETMC, the surface information of the website given in **Figure 5.2**. The downloaded data from the website is the format of the text file and it should be converted to excel file format. Before downloading data, one should read the guidelines in the webpage carefully to obtain a correct output. Examples of the prepared data table are shown in the below.

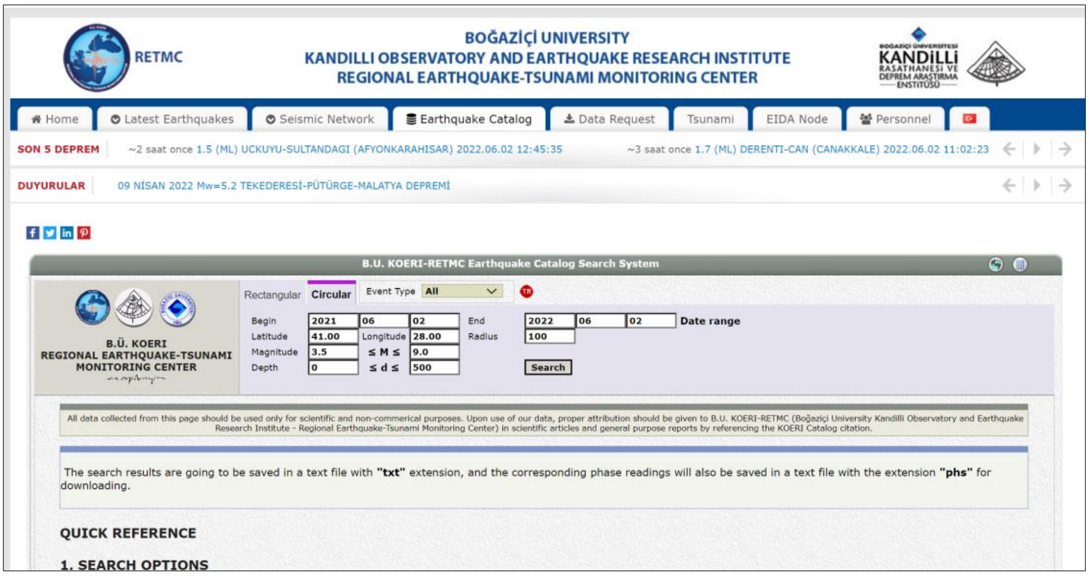

Figure 5.2. An overview for the surface information of the website [215].

Table 5.1. List of selected earthquakes according to Ankara station (39.8875° N, 32.7586° E) in IONOLAB.

No	Date (dd-mm-yyyy)	Time (UT)	Location of epicenter		Depth (km)	Magnitude (M)	Distance to the EQ epicenter (km)	De/R	Site location
			Latitude	Longitude					
EQ1	09-02-2007	15:30	39.9423	32.3487	14.9	3	35.5	1.82	Outside EPZ
EQ2	16-02-2007	20:11	40.075	32.7777	8.1	3.3	20.9	0.8	Inside EPZ
EQ3	21-02-2007	11:05	38.3525	39.307	7.5	5.9	590	1.71	Outside EPZ

Table 5.1 displays the earthquakes list and the distance from the TEC receiver station of Ankara city to the earthquake epicenter (De). Also, the ratio of De/R is given for determining whether the TEC receiver station is inside/outside the earthquake preparation zone.

Table 5.2. List of selected earthquakes according to Trabzon station (40.9947° N, 39.7756° E) in IONOLAB.

No	Date (dd-mm-yyyy)	Time (UT)	Location of epicenter		Depth (km)	Magnitude (M)	Distance to the EQ epicenter (km)	De/R	Site location
			Latitude	Longitude					
EQ1	21-01-2007	07:38	39.606	42.829	5	5.1	301.5	1.93	Outside EPZ
EQ2	27-01-2007	00:56	40.9768	39.3015	5	3.4	39.8	1.38	Outside EPZ
EQ3	05-02-2007	10:29	41.1117	40.0667	16.3	3.2	27.7	1.16	Outside EPZ
EQ4	09-02-2007	02:22	38.404	39.0475	3	5.5	294.7	1.27	Outside EPZ
EQ5	19-02-2007	10:03	40.8482	39.6305	21.4	2.8	20.3	1.27	Outside EPZ
EQ6	21-02-2007	11:05	38.3525	39.307	7.5	5.9	296.5	0.86	Inside EPZ
EQ7	22-02-2007	09:51	40.8145	39.7212	5.6	2.7	20.6	1.42	Outside EPZ

Table 5.2 shows the list of earthquakes and the distance from the TEC receiver station of Trabzon city to the earthquake epicenter (De). Also, the ratio of De/R is given for determining whether the TEC receiver station is inside/outside the earthquake preparation zone.

Radon and TEC anomaly considered as a result of earthquake if the ratio between D_e (distance to the EQ epicenter) and R (preparation zone) smaller and equal to one. The Dobrovolsky earthquake preparation radius is given as [93],

$$R = 10^{0.43M}\ km \quad \text{(earthquake preparation zone)} \tag{55.1}$$

where M is earthquake magnitude;

The linear epicentral distance (in km) D_e is well-defined as a product of the Earth's radius ($\rho \approx 6371km$) and the angular distance (in radian), the factor of converting degree to radian is π/180, ϕ which is between the Radon/TEC monitoring station and the earthquake epicenter as shown in **Figure 5.3**.

$$D_e = \rho\varphi \tag{55.2}$$

Where,

$$\varphi = cos^{-1}(\cos\alpha_a\ \cos\alpha_b + \sin\alpha_a\ \sin\alpha_b \cos(\beta_a - \beta_b))$$

where (α_a, β_a) are geographic coordinates of the earthquake event and (α_b, β_b) are the geographic coordinates of Radon/TEC monitoring station in radian [216]. In this study, the earthquakes inside [(De/R) <1] and outside [(De/R) <2] of the preparation zone were selected.

$$\frac{D_e}{R} \leq 2$$

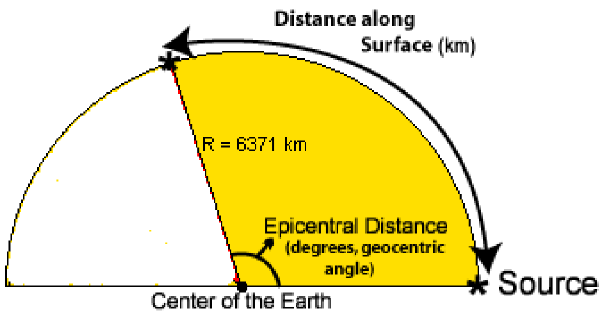

Figure 5.3. Epicentral Distance and Surface Distance (1° of epicentral distance is equal to 111.2 km) [217].

5.2.2. Radon Data

Alpha particle detectors are used to continuously monitor the Rn-222 gas in the soil (Model 611 Alpha Meter from AlphaNuclear Co. is employed). Rn-222 concentration is measured every 15 minutes in $kBqm^{-3}$. The Alpha-Meter-611 sensors are placed in a small borehole (one meter). The data is automatically stored in a repository by the data collection system. The Ministry of Interior's Disaster and Emergency Management Presidency has made this information available (AFAD), Türkiye (https://en.afad.gov.en/). In this study, we worked on the Reşadiye town in Tokat city where the radon monitoring station is located at Latitude 40.38977 and Longitude 37.33451. The **Figure 5.4** below shows the alpha particle detectors composition.

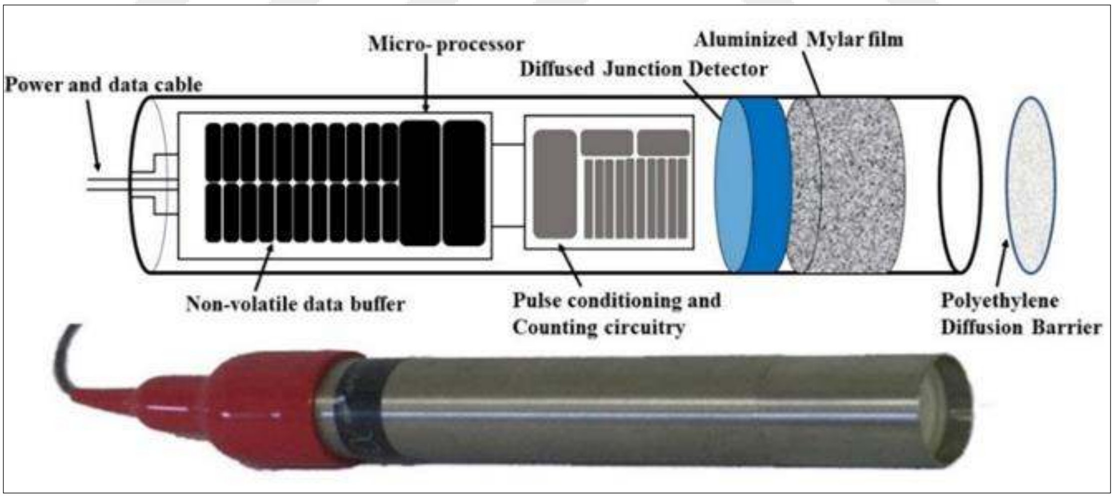

Figure 5.4. The Alpha-Meter 611 detector composition [218].

The **Figure 5.5-8** displays the transformation of the radon data in 15 minutes interval, **Figure 5.6** displays interpolated in 15 minutes interval, **Figure 5.7** and **Figure 5.8** illustrate daily and monthly resampled and interpolated respectively. From the given figures, it is clear that radon data has seasonality behavior which is linked to certain meteorological parameters in the next subsection will be mentioned.

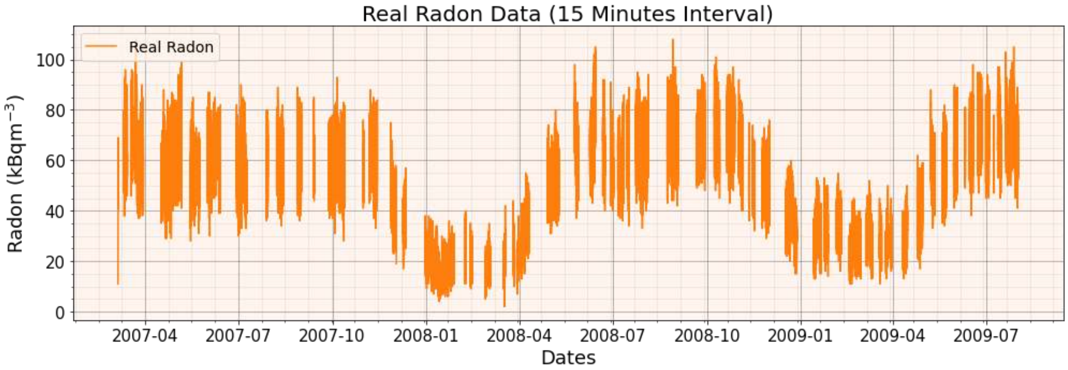

Figure 5.5. Radon data from the Reşadiye radon monitoring station located at Latitude 40.38977 and longitude 37.33451.

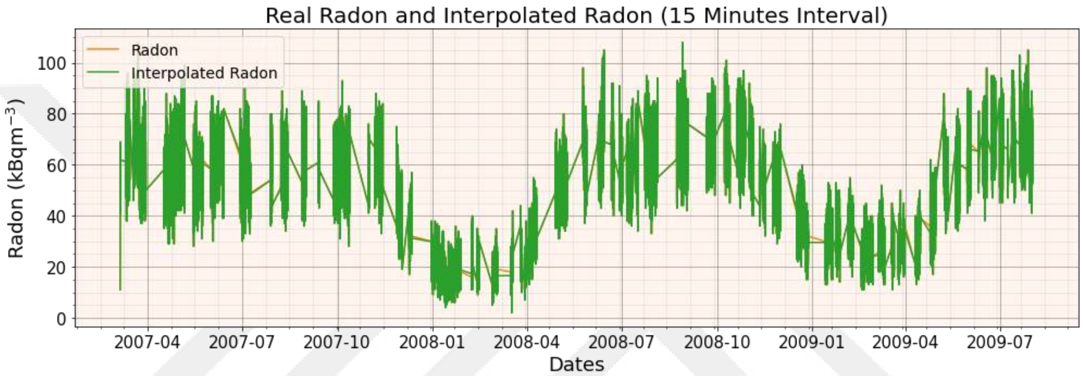

Figure 5.6. Interpolated and actual radon data in 15 minutes interval.

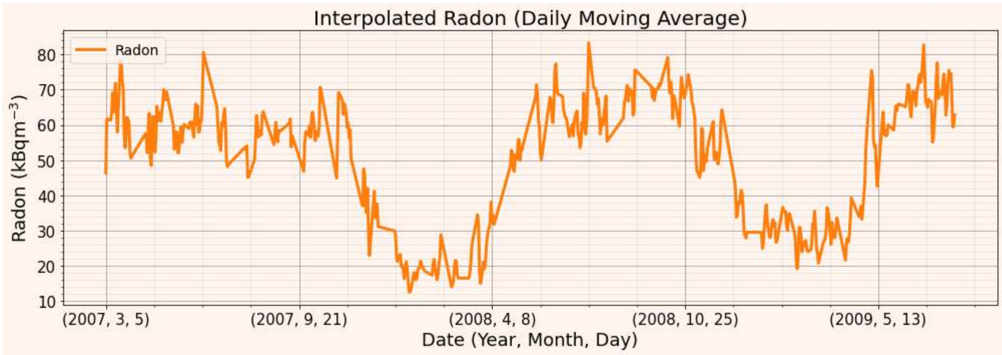

Figure 5.7. Daily resampled and interpolated radon data.

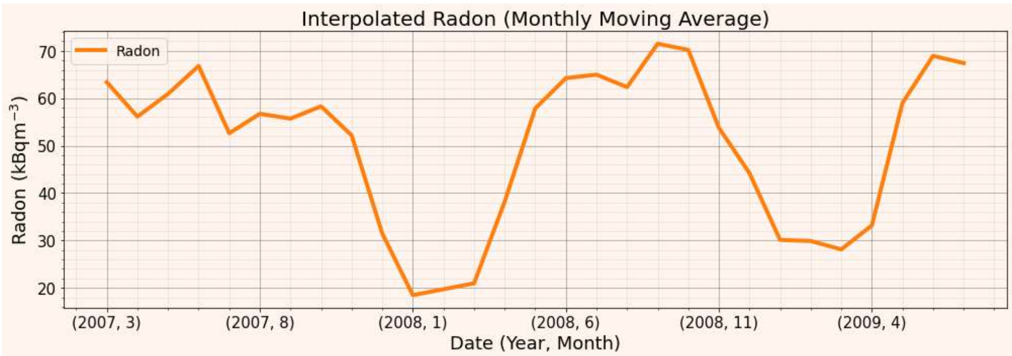

Figure 5.8. Monthly resampled and interpolated radon data.

5.2.3. Meteorological Data

The meteorological data are provided by the Ministry of Environment, Urbanization and Climate Change- General Directorate of Meteorology (https://mgm.gov.tr/). The Soil temperature data is recorded at various depths (5cm, 10cm, 20cm and 50cm). These data sets are useful as they will enable study of the relationship between Radon-222 and meteorological variables. The temperature and pressure are obtained for daily variation in units of °C and hPa respectively. The meteorological parameters and Radon data for the study region are given in **Figure 5.9** and **Figure 5.10**.

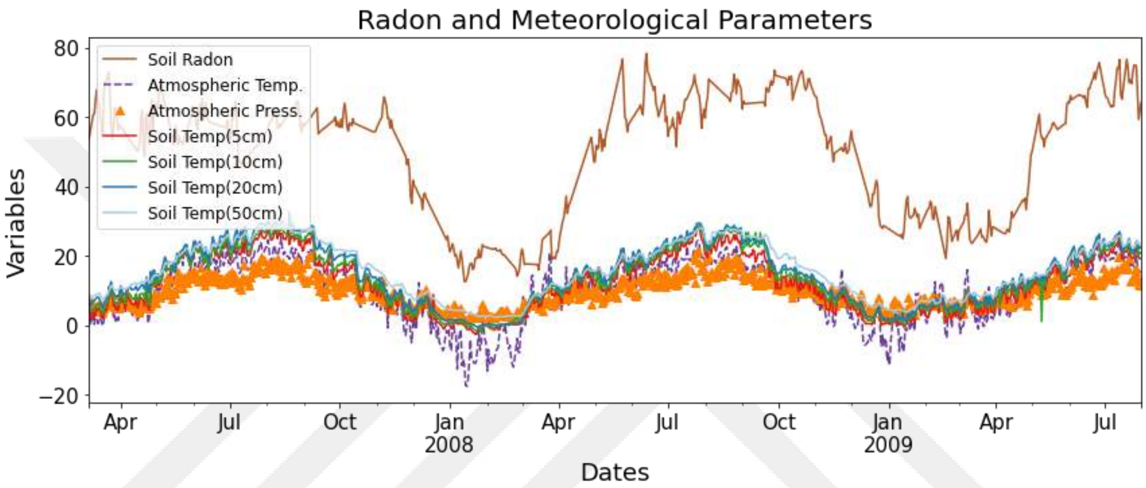

Figure 5.9. Radon-222 concentration and meteorological parameters (Atm. Temp., Atm. Press., and Soil Temp.).

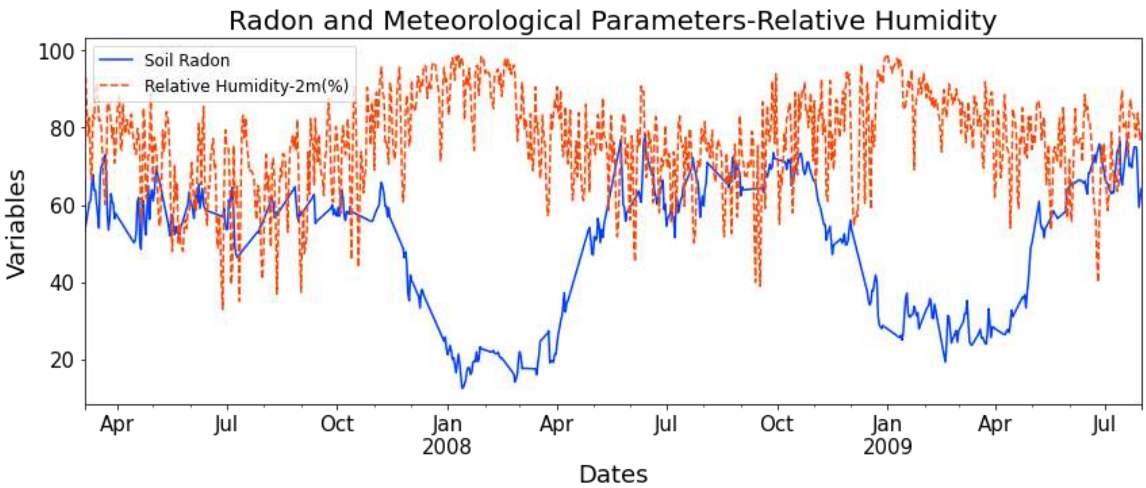

Figure 5.10. Radon-222 concentration and relative humidity.

From the **Figure 5.9**, it is seen that Radon and meteorological data are positively and highly correlated. While in **Figure 5.10**, negative and less correlation can be observed. Based on this, in the next section statistical properties will be stated for the purpose of a multi-linear regression model.

5.2.4. VTEC Data and TEC Maps

Total electron content (TEC) data used in this thesis was provided by IONOLAB-TEC online v1.34, from the Electrical and Electronics Engineering Department at Hacettepe University (http://www.ionolab.org/webtec/). For downloading data, one should create a user then can proceed with it. The TEC data has a 2.5 minutes sampling interval in units of TECU, 1TECU = 10^{16} el/m^2. The TEC data from IONOLAB are estimated vertical total electron content (VTEC) which initially it is in Rinex file format. The surface information of the website for single stations is shown in **Figure 5.11**.

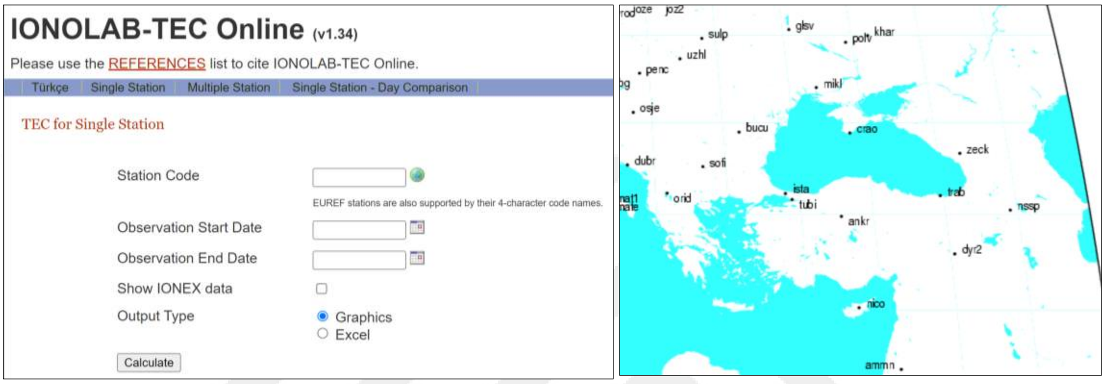

Figure 5.11. An overview for the surface information of the website with the code of stations (right) [219].

Similarly, ionospheric maps were obtained from (http://www.ionolab.org/), built on the Ionosphere Extended to Plasmasphere as an International Reference (IRI-PLAS). The latitudinal and longitudinal resolutions of these TEC map data are 2.5° and 5°, respectively, and they are generated per 2 hours in UTC. The surface information of the website for single stations is shown in **Figure 5.12**.

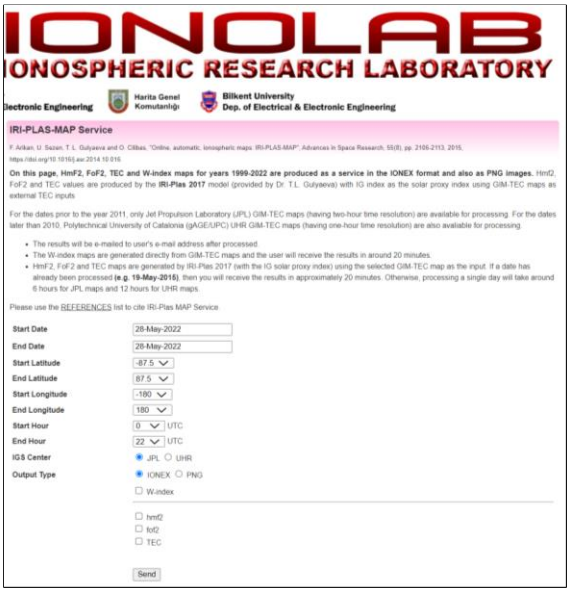

Figure 5.12. An overview for the surface information of the website [220].

5.2.5. Solar and Geomagnetic Data

The data on geomagnetic and solar activity were taken at (OMNI). The geomagnetic and solar variables had to be taken into consideration in order to determine whether or not a certain TEC anomaly was seismically produced. For this reason, the variation of the geomagnetic storm time disturbance (Dst in nT), the solar radio flux (F10.7) in solar flux units (1 SFU = 10^{-22} W m^{-2} Hz^{-1}), and the 3-hour kp are considered. kp is a three-hour index used to determine the global level of "all irregular disturbances of the geomagnetic field caused by solar particle radiation within the 3-hour interval concerned" [221]. kp index is similar to ap and sunspot number (R) similar to F10.7, therefore, we will use F10.7, kp, Dst. The equivalent and range of mentioned data were demonstrated in **Table 5.3** for Kp index, **Table 5.4** for Dst geomagnetic activity, and **Table 5.5** for sunspot number SSN and its equivalent to F10.7.

Table 5.3. Quiet and disturbed days using geomagnetic kp index.

Kp Index 0-90 (OMNI)	Geomagnetic Activity Level	Kp Index 0-90 (OMNI)	Geomagnetic Activity Level
0	Quiet	47	Minor storm
3	Quiet	**50**	Minor storm
7	Quiet	53	Minor storm
10	Quiet	57	Moderate storm
13	Quiet	**60**	Moderate storm
17	Quiet	63	Moderate storm
20	Quiet	67	Strong storm
23	Quiet	**70**	Strong storm
27	Unsettled	73	Strong storm
30	Unsettled	77	Severe storm
33	Unsettled	**80**	Severe storm
37	Active	83	Severe storm
40	Active	87	Severe storm
43	Active	**90**	Extreme storm

Table 5.4. Dst geomagnetic activity.

Dst (Disturbance Storm Time) (nT)	Geomagnetic Activity Level
(Dst > -20)	Quiet
(Dst< - 20)	Disturbed
(Dst > -20)	Quiet geomagnetic activity
(-20 > Dst> -50)	Moderate magnetic storm
(-50 > Dst> -100)	Strong magnetic storm
(-100 > Dst> -250)	Severe (very strong) magnetic storm
(Dst< -250)	Extreme(super) magnetic storm

Table 5.5. Sunspot number SSN and its equivalent to F10.7.

F10.7 (OMNI)	Sunspot Number SSN (R) (OMNI)	
		Solar Activity
64-67	0	0-20 (Very Low)
83	25	
102	50	20-40 (Low)
124	75	40-80 (Moderate)
148	100	80-150 (High)
172	125	
196	150	150-250 (Very High)
219	175	
240	200	
273	250	> 250 (Extreme)
	300	

In **Table 5.3-5,** the solar and geomagnetic activity range from the OMNI web are obtained. Then, the threshold level for quiet conditions is given in the next chapter for this study.

6. MODELS AND METHODS

In this chapter, Models for Radon and TEC variations over Türkiye were obtained using suitable regression models (ARIMA and Machine learning models) and attempted to forecast Radon and TEC values using the model and optimize this forecast with Monte-Carlo simulation method. Then seek the relationship between TEC and earthquakes. Also, TEC values were modelled and pre-anomalies and post- anomalies detected for selected earthquakes. Moreover, for moderate earthquakes, the temporal and spatial properties of ionospheric anomalies will be analyzed. Finally, statistical relationship between Rn-222 and TEC using cross correlation analysis obtained.

6.1. Radon Models

Model Radon variations using suitable regression model (ARIMA), multi-regression model, and multi-ANN model. Also, attempted to forecast Radon and TEC values using the model and optimize this forecast with Monte-Carlo simulation method.

6.1.1. ARIMA

Box and Jenkins developed the Auto Regressive Integrated Moving Average (ARIMA) model [70]. ARIMA (p, I, q) formed from the combination of the (AR (p)) section, integrated (I (d)) section and (MA (q)) section. By regressing the Radon values on their previous values, the AR component denotes the drawn-out effects of earlier Radon. The degree of differencing is indicated by the integrated (I) section. ARIMA model has been utilized to forecast the seasonal variations and diurnal of Radon values. Box and Jenkins define the ARIMA model in its most general form [70],

$$\phi_p(B)(1-B)^d X_t = c + \theta_q(B)\varepsilon_t \tag{66.1}$$

where p is Autoregressive Orders processes, q is Orders of Moving average processes, θ_q ϕ_p are Coefficients of MA and AR sections, X_t is Radon at time t, d stands for the number of times the Radon has been differenced, B is the operator for $BV_t = V_{t-1}$'s backward shift, c stands for constant term, ε_t is Error, a normal distribution with zero mean and standard deviation, σ.

The stationary AR operator's mathematical expression will be as follows,

$$\phi_p(B) = \left(1 - \phi_1 B - \phi_2 B^2 - \ldots - \phi_{p-1} B^{p-1} - \phi_p B^p\right) \tag{66.2}$$

In the same way, the invertible MA operator is defined as,

$$\theta_q(B) = \left(1 - \theta_1 B - \theta_2 B^2 - \ldots - \theta_{q-1} B^{q-1} - \theta_q B^q\right) \tag{66.3}$$

For the lowest Akaike Information Criterion, the proper ARIMA model for Radon data may be found (AIC). For determining the order of a time series, AIC holds the maximum likelihood function. AIC's mathematical expression is as follows,

$$AIC_{(r,s)} = \ln \hat{\delta}^2 + \frac{2(r+s+1)}{N} \quad (66.4)$$

$$AIC(p,q) = \min_{0 \leqslant s \leq 1} AIC(r,s) \quad (66.5)$$

If the following equation is fulfilled, the ARIMA model's order is (p, q), where, s lies in between 0 and Q, r lies in between P and 0, $\hat{\delta}^2$ is the max. probability estimate for Radon time series.

- **ARIMA Model for Radon data in this study:**
  - ADFT

$$y_t \;=\; c \;+\; \delta\, t \;+\; \phi\, y_{t-1} \;+\; \beta_1\, \Delta\, y_{t-1} \;+\; \ldots \;+\; \beta_p\, \Delta\, y_{t-p} \;+\; \varepsilon_t$$

$$H_0 :\; \phi \;=\; 1 \quad H_a :\; \phi \;<\; 1$$

Table 6.1. Parameters of Test.

	Lags	Model	Statistic of Test	Level of Significance
1	20	AR	t1	0.05

Table 6.2. Results of Test.

	Null-Rejected	P value	Statistic of Test	Critical value
1	true	0.013883	-2.4617	-1.9417

Table 6.1 and **Table 6.2** display the parameters and results of the Radon time series. For this range of data, the p-value is (0.013883), statistic of test is (-2.4617), and critical value is (-1.9417).

- Model Estimation

Table 6.3. Estimation Results.

Parameter	Value	Standard Error	t Statistic	P value
Constant	-0.018894	0.082782	-0.22824	0.81946
AR{1}	0.018433	0.058784	0.31358	0.75384
AR{2}	-0.23458	0.043494	-5.3934	6.9152e-08
AR{3}	0.80395	0.058044	13.8506	1.2609e-43
MA{1}	-0.13807	0.07967	-1.733	0.083092
MA{2}	0.094165	0.061625	1.528	0.1265
MA{3}	-1	0.067502	-14.8143	1.1833e-49
MA{4}	0.10818	0.079623	1.3587	0.17426
MA{5}	0.16082	0.052872	3.0417	0.0023528
MA{6}	0.13701	0.060849	2.2516	0.024347
MA{7}	0.0018149	0.053368	0.034007	0.97287
Variance	17.3844	1.0815	16.0743	3.8619e-58

ARIMA (3,1,7) of time series Radon with the following equation:

$$(1 - \phi_1 L - \phi_2 L^2 - \phi_3 L^3)(1 - L)y_t \;=\; c \;+\; (1 + \theta_1 L - \ldots - \theta_7 L^7)\varepsilon_t$$

Table 6.4. Goodness of Fit.

AIC	2124.8824
BIC	2171.6812

Table 6.3 shows the estimation result with 12 parameters and **Table 6.4** illustrates the goodness of fit using Akaike information criterion and Bayesian information criterion.

➢ **ARIMA Model for Interpolated Radon data in this study:**

- ADFT

$$y_t = c + \delta t + \phi y_{t-1} + \beta_1 \Delta y_{t-1} + ... + \beta_p \Delta y_{t-p} + \varepsilon_t$$

$$H_0 : \phi = 1$$

$$H_a : \phi < 1$$

Table 6.5. Parameters of Test.

	Lags	Model	Statistic of Test	Level of Significance
1	20	AR	t1	0.05

Table 6.6. Results of Test.

	Null-Rejected	P value	Test Statistic	Critical value
1	true	0.001	-5.3144	-1.9414

Table 6.5 and **Table 6.6** display the parameters and results of the interpolated Radon time series. For this range of data, the p-value is (0.001), statistic of test is (-5.3144), and critical value is (-1.9414).

- ARIMA (7,1,3) Model (Gaussian Distribution) (ARIMA_Radon1)

Equation for ARIMA (7,1,3) model of Radon1 time series:

$$(1 - \phi_1 L - ... - \phi_7 L^7)(1 - L)y_t = c + (1 + \theta_1 L + \theta_2 L^2 + \theta_3 L^3)\varepsilon_t$$

- Model Estimation

Table 6.7. Estimation Results.

Parameter	Value	Standard Error	t Statistic	P value
constant	-0.0033201	0.015205	-0.21836	0.82715
AR{1}	0.62078	0.27527	2.2552	0.024123
AR{2}	-0.19997	0.36184	-0.55263	0.58052
AR{3}	0.34413	0.26913	1.2787	0.20101
AR{4}	-0.013893	0.075374	-0.18432	0.85376
AR{5}	0.02532	0.056409	0.44886	0.65354
AR{6}	-0.069494	0.041318	-1.682	0.092577
AR{7}	0.11349	0.033547	3.3829	0.00071715
MA{1}	-0.52785	0.27848	-1.8955	0.058027
MA{2}	0.0021482	0.34421	0.0062409	0.99502
MA{3}	-0.30008	0.24711	-1.2144	0.22461
Variance	5.2466	0.17796	29.4816	4.9586e-191

Table 6.8. Goodness of Fit.

AIC	3575.4175
BIC	3631.3598

Table 6.7 shows the estimation result with 12 parameters and **Table 6.8** illustrates the goodness of fit using Akaike information criterion and Bayesian information criterion.

6.1.2. Multi-Linear Regression

Multiple regression's primary goal is to learn more about the relationship between a dependent or criterion variable and several independent or predictive factors. A relationship between one dependent (response or output parameters) variable and a single independent (predictor or input parameters) variable is identified using simple linear regression. However, a more advanced kind of regression approach known as multiple linear regression is extensively employed to study the relationship between a single dependent and several independent variables. [26]. When working with fewer variables and huge amounts of accurate and valid data, regression-based prediction is most effective [222]. The variables used in the MLR are shown in **Figure 6.1**.

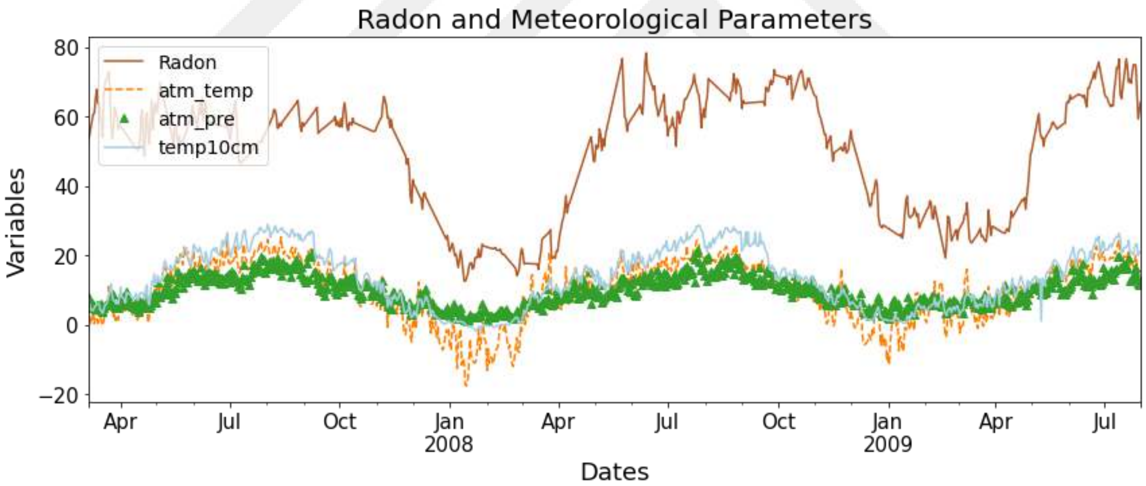

Figure 6.1. The input data to multi-linear regression model.

The multiple regression equation is given as:

$$y = \alpha_1 x_1 + \alpha_2 x_2 + ... + \alpha_n x_n + c \quad (66.6)$$

where, α_1, α_2, α_n is a coefficient of regression showing the dependent amount (output parameters) variable y that changes when the corresponding independent (input parameters) variables change by (one unit). Where the regression line intercepts the y-axis, c is constant, when all the independent variables are zero, showing the amount of the dependent variable y [223].

The response variable in this study is radon, while the predictor factors are meteorological variables (atm. temperature, atm. pressure and soil temperature_10cm). When using multiple linear regression, it's common to find that all of the predefined independent variables will not contribute significantly to the prediction of the response variable. Accordingly, we selected the number of independent variables (three) to obtain a better fit and minimize error in predicting the dependent variable. The scatter plot and Correlogram for the data used in the multi-regression model are displayed in **Figure 6.2** and **Figure 6.3** which displays high correlation between the radon concentration and meteorological parameters.

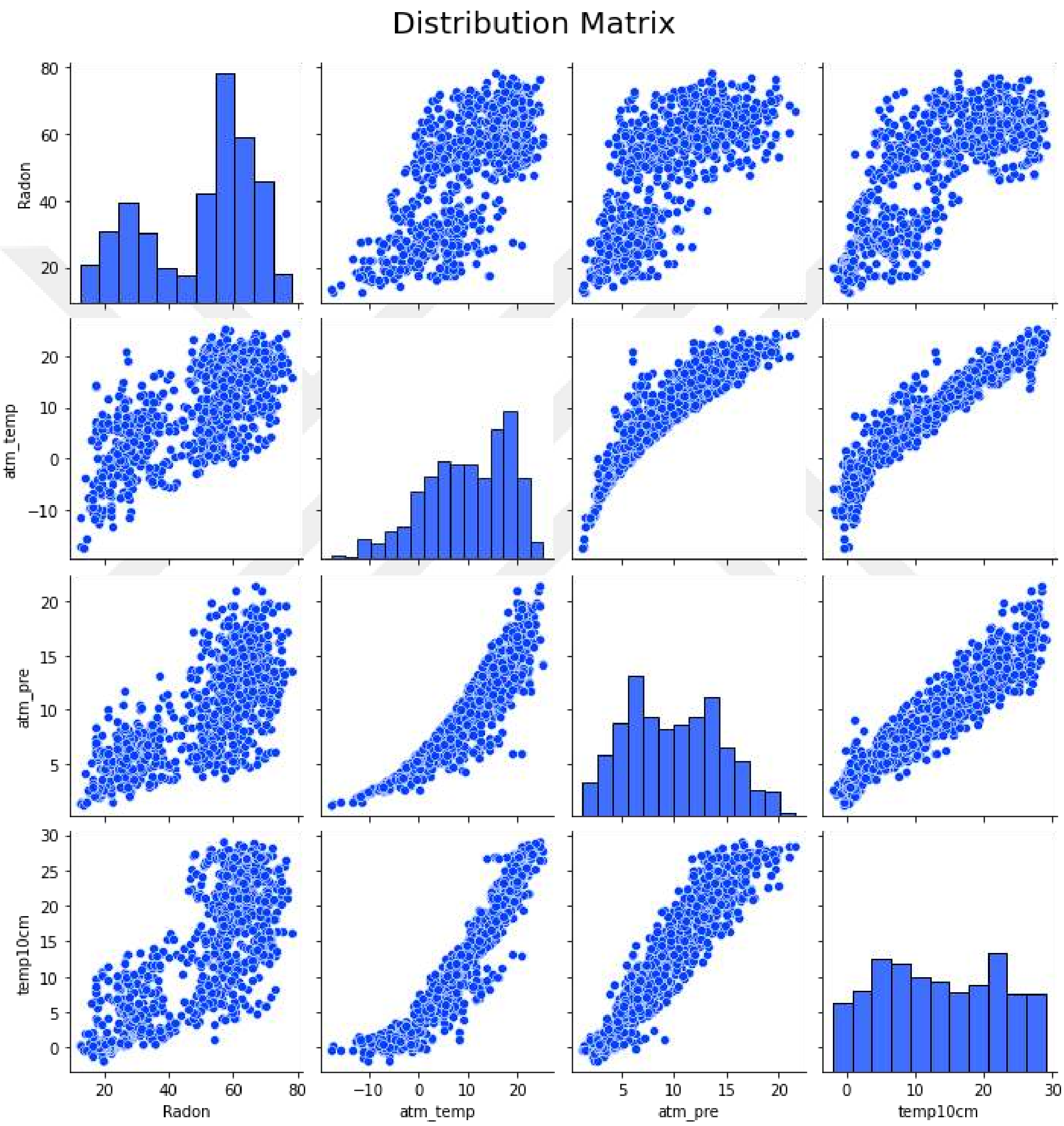

Figure 6.2. Scatter plot between radon concentration and atmospheric temperature, atmospheric pressure, and soil temperature_10cm.

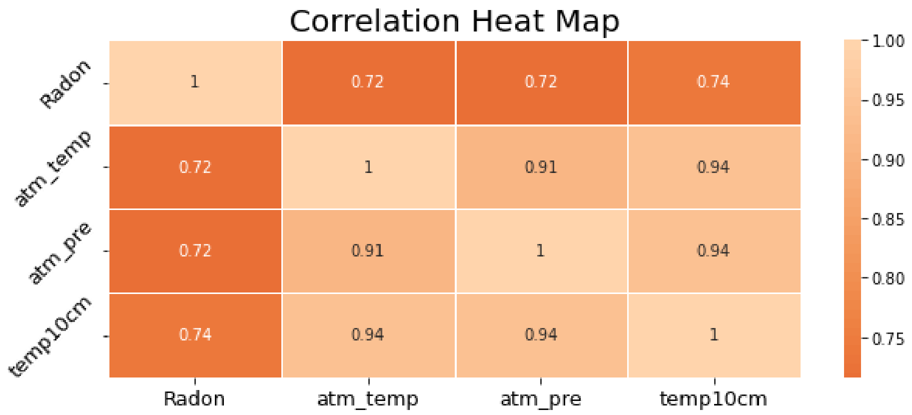

Figure 6.3. Pearson correlation between radon concentration and atmospheric temperature, atmospheric pressure, and soil temperature_10cm.

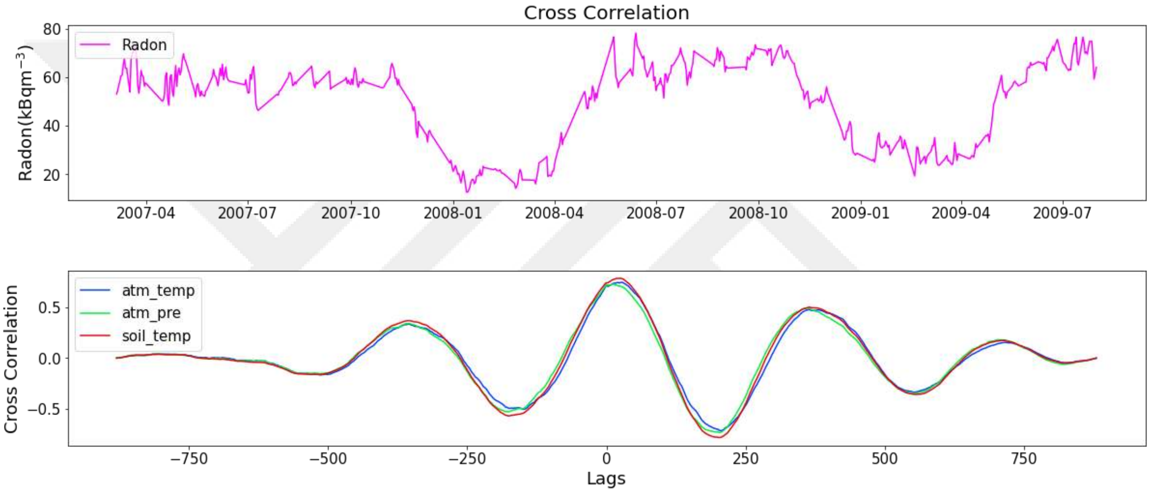

Figure 6.4. Cross-correlation between radon, atmospheric temperature, atmospheric pressure, and soil temperature_10cm.

The cross-correlation can be seen in **Figure 6.4**, where the maximum correlation for soil temperature (at lag 25), atmospheric temperature (at lag 28) and pressure (at lag 12) is 0.7832, 0.7432, and 0.7256 respectively.

In this study, the multiple regression equation is given as:

$$Rn_{(222)} = \alpha_0 + \alpha_1 T_{atm} + \alpha_2 P_{atm} + \alpha_3 T_{soil\_10cm} + \varepsilon_{Mreg} \qquad (66.7)$$

where α_0, α_1, α_2, *and* α_3 stands for regression coefficients that are predicted to best capture radon behavior.

6.1.3. Multi-Artificial Neural Network and Monte-Carlo Simulation

Artificial neural network (ANN) is a mathematical model that is used to treat a variety of problems and is based on the biological activity of neurons and the structure of the brain. Artificial neurons, also known as nodes, are a type of biological neuron that are highly interconnected, making up the basic processing parts of ANNs. Three main components can be used to define a network: transfer function, network architecture, and learning law.

The ability of ANNs to model the learning process is one of its most outstanding properties. They are given pairs of input and output signals from which general rules are established automatically, allowing the ANN to generate the proper output for a signal that has never been utilized before.

The multiple regression equation (66.7) can be improved to enhance the predicted data by implementing artificial neural network (ANN) model on the multi-regression residuals, such as time series prediction by [224]. In this study, Python was utilized in three-layer feed-forward for neural network analyses, the first layer that comprises of the layer of input and output (4 neurons), second layer (86 neurons), third layer (17 neurons), and the product (biological neuron) as shown in **Figure 6.5**. Adam was chosen to promote learning and a mean square error (MSE) was chosen to EPOCH.

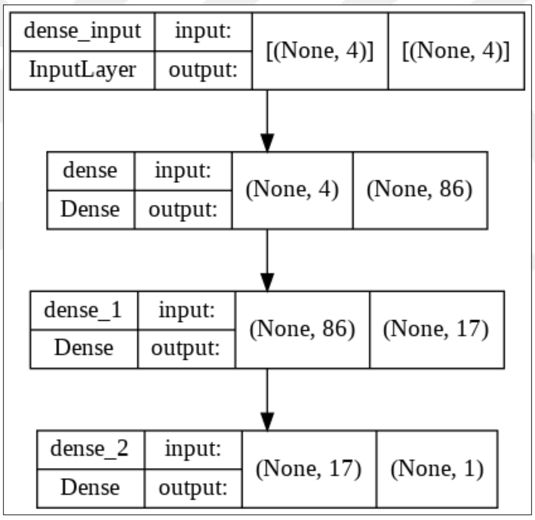

Figure 6.5. Artificial Neural Network structure used to model the residual of multi-regression model.

Therefore, the multiple regression equation can be written as given below:

$$Rn_{(222)} = \alpha_0 + \alpha_1 T_{atm} + \alpha_2 P_{atm} + \alpha_3 T_{soil\_10cm} + \varepsilon_{Mreg}(ANN) + \varepsilon \quad (66.8)$$

where $\varepsilon_{Mreg}(ANN)$ stands for ANN model for regression residuals and ε is the error of integrated models' combination. The data was separated into input and target sequences, and then processed as follows:

If $\varepsilon_{Mreg} = \{x_n\}$ is a residual data set from a multiple regression model, and is the length of the residual data string, we can describe it using index numbers as follows:

$$\varepsilon_{Mreg} = \{x_k,\ x_{k+1}, \dots,\ x_{k+n-1}\} \quad (66.9)$$

They are given input and output arrays in pairs, the input array is used by the model to learn the responses, and the target is predicted.

For ε_{Mreg} , n = 704 and window = 4, the input and target arrays are divided into training (80%) and validation (20%), which are fed into the feed-forward artificial neural network architecture presented in **Figure 6.5**.

Subsequently, Monte Carlo simulation (19 paths) was achieved using the multi-ANN function to predict radon values which were used in [225]. For the model performance on the radon data, root mean square error, R^2, and Pearson correlation were considered.

6.2. TEC Models

In this section, Models for TEC variations were obtained using ARIMA model and attempted to forecast TEC values using the model and optimize this forecast with Monte-Carlo simulation method. Then seek the relationship between TEC and earthquake. Also, TEC values were modelled using median TEC for detecting pre-anomalies and post- anomalies for selected earthquakes. For moderate earthquakes, we also explore the temporal and spatial properties of ionospheric disturbances.

6.2.1. ARIMA

Box and Jenkins developed the Auto Regressive Integrated Moving Average (ARIMA) model [70]. ARIMA (p, I, q) formed from the combination of the (AR (p)) section, integrated (I (d)) section and (MA (q)) section. By regressing the VTEC values on their previous values, the AR component denotes the drawn-out influence of earlier VTEC. The degree of differencing is indicated by the integrated (I) section. ARIMA model has been utilized to forecast the seasonal variations and diurnal of VTEC values. Box and Jenkins define the ARIMA model in its most general form [70],

$$\phi_p(B)(1-B)^d X_t = c + \theta_q(B)\varepsilon_t \tag{66.10}$$

where p is Autoregressive Orders processes, q is Orders of Moving average processes, θ_q ϕ_p are Coefficients of MA and AR sections, X_t is VTEC at time t, d stands for the number of times the VTEC has been differenced, B is the operator for $BV_t = V_{t-1}$'s backward shift, c stands for constant term, ε_t is Error, a normal distribution with zero mean and standard deviation, σ.

The stationary AR operator's mathematical expression is as follows,

$$\phi_p(B) = \left(1 - \phi_1 B - \phi_2 B^2 - \ldots - \phi_{p-1} B^{p-1} - \phi_p B^p\right) \tag{66.11}$$

In the same way, the invertible MA operator is defined as,

$$\theta_q(B) = \left(1 - \theta_1 B - \theta_2 B^2 - \ldots - \theta_{q-1} B^{q-1} - \theta_q B^q\right) \quad (66.12)$$

For the lowest Akaike Information Criterion, the proper ARIMA model for VTEC data may be found (AIC). For determining the order of a time series, AIC holds the maximum likelihood function. AIC's mathematical expression is as follows,

$$AIC_{(r,s)} = \ln \hat{\delta}^2 + \frac{2(r+s+1)}{N} \quad (66.13)$$

$$AIC(p,q) = \min_{0 \leqslant s \leq 1} AIC(r,s) \quad (66.14)$$

If the following equation is fulfilled, the ARIMA model's order is (p, q), where, s lies in between 0 and Q, r lies in between P and 0, $\hat{\delta}^2$ is the max. probability estimate for VTEC time series.

- **ARIMA Model for TEC data in this study:**
  - ADFT

$$y_t = c + \delta t + \phi y_{t-1} + \beta_1 \Delta y_{t-1} + \ldots + \beta_p \Delta y_{t-p} + \varepsilon_t$$

$$H_0 : \phi = 1 \quad H_a : \phi < 1$$

Table 6.9. Parameters of Test.

	Lags	Model	Statistic of Test	Level of Significance
1	20	AR	t1	0.05

Table 6.10. Results of Test.

	Null-Rejected	P value	Statistic of Test	Critical value
1	true	0.001	-12.6338	-1.9416

Table 6.9 and **Table 6.10** display the parameters and results of the VTEC time series. For this range of data, the p-value is (0.001), statistic of test is (-12.6338), and critical value is (-1.9416).

Equation for ARIMA (14,1,10) model of time series TEC:

$$(1 - \phi_1 L - \ldots - \phi_{14} L^{14})(1 - L)y_t = c + (1 + \theta_1 L - \ldots - \theta_{10} L^{10})\varepsilon_t$$

Table 6.11. Goodness of Fit.

AIC	658.3901
BIC	756.7696

Table 6.12 shows the model estimation result with 26 parameters including autoregressive orders processes, moving average, standard error, t statistics, and p value. **Table 6.11** illustrates the goodness of fit using Akaike information criterion (658.3901) and Bayesian information criterion (756.7696).

Table 6.12. Model estimation Results.

Parameter	Value	Standard Error	t Statistic	P value
constant	0.019185	0.035343	0.54283	0.58725
AR{1}	0.32499	0.18161	1.7895	0.073526
AR{2}	0.17801	0.12874	1.3828	0.16673
AR{3}	-0.42407	0.21868	-1.9393	0.052469
AR{4}	0.40807	0.28354	1.4392	0.15009
AR{5}	-0.035655	0.21524	-0.16565	0.86844
AR{6}	-0.23546	0.1522	-1.547	0.12186
AR{7}	0.32615	0.24552	1.3284	0.18405
AR{8}	-0.18731	0.23247	-0.80571	0.42041
AR{9}	-0.25192	0.12535	-2.0097	0.044466
AR{10}	-0.29613	0.1512	-1.9585	0.050168
AR{11}	0.12052	0.098479	1.2239	0.22101
AR{12}	0.0539	0.086893	0.6203	0.53506
AR{13}	-0.044841	0.092221	-0.48624	0.6268
AR{14}	-0.35694	0.089172	-4.0029	6.2582e-05
MA{1}	0.17411	0.19001	0.91633	0.35949
MA{2}	-0.46004	0.1119	-4.1113	3.9337e-05
MA{3}	0.34965	0.22315	1.5669	0.11714
MA{4}	-0.40975	0.19377	-2.1146	0.034462
MA{5}	-0.43523	0.15417	-2.823	0.0047571
MA{6}	0.32065	0.24384	1.315	0.18851
MA{7}	-0.23829	0.2407	-0.98999	0.32218
MA{8}	-0.12091	0.14474	-0.83532	0.40354
MA{9}	0.50175	0.13297	3.7734	0.00016102
MA{10}	0.57182	0.23811	2.4015	0.01633
Variance	0.34846	0.027949	12.4676	1.1215e-35

6.2.2. Median and Relative VTEC

In this section, vertical TEC variations caused by seismic activity were modelled for detecting pre-anomalies and post- anomalies per earthquake. Median TEC values as illustrated in **Figure 6.6**, DTEC, upper and lower bounds were calculated. Anomalies for moderate earthquakes during 2007-2010 were investigated. The ionospheric changes were analyzed including solar and geomagnetic activity data as shown **Table 6.13**. The Dobrovolsky preparation zone for the earthquakes was computed. Earthquakes inside (De/R) <1 and outside (De/R) <2 preparation zone were selected. Finally, the positive and negative anomalies were identified for earthquakes in quiet condition of geomagnetic and solar activity using the following equations:

$$Median(TEC) = \begin{cases} TEC\left[\frac{n}{2}\right] & \text{if } n \text{ is even} \\ \dfrac{TEC\left[\frac{n-1}{2}\right] + TEC\left[\frac{n+1}{2}\right]}{2} & \text{if } n \text{ is odd} \end{cases} \tag{66.15}$$

$$UB = M \quad + (1.5\,\sigma) \;\rightarrow (65\%\ Confidence\ level) \quad Upper\ boundary \tag{66.16}$$

$$LB = M \quad - (1.5\,\sigma) \;\rightarrow (65\%\ Confidence\ level) \quad Lower\ boundary \tag{66.17}$$

$$\text{DTEC} = \frac{TEC - UB}{UB} \quad \text{DTEC} = \frac{TEC - LB}{LB} \qquad Relative\ TEC\ deviation \tag{66.18}$$

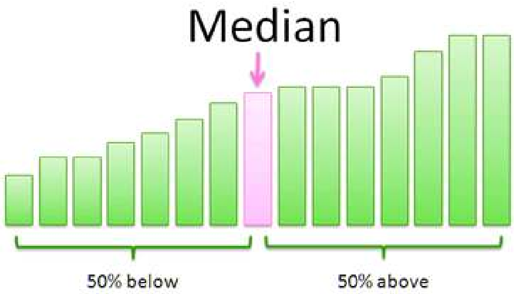

Figure 6.6. Shows median value of a time series.

Table 6.13. Threshold level for quiet conditions.

Indices	Range
F10.7 (OMNI)	F10.7 ≥ 100 SFU
Dst	-40 nT ≥ Dst ≥ 40 nT
kp index 0-90 (OMNI)	kp ≥ 33

6.2.3. Temporal and Spatial TEC

Seismo-ionospheric disturbances have been studied in general utilizing temporal fluctuations in ionospheric factors around the epicenter, as well as research on spatial fluctuations of seismo-ionospheric disturbances using global TEC maps [208,226]. The temporal and spatial properties during moderate earthquakes are investigated in this work. To provide it, first compute the median diurnal variation of the TEC for the interval centered around the earthquake date. It was also utilized to determine the temporal TEC deviation, as shown in Equation (66.19),

$$mTEC \quad = \frac{TEC - M}{M} \quad Temporal\, TEC\ deviation \qquad (66.19)$$

In the literature, research revealed that ionospheric anomalies prior to seismic events exhibited local patterns inside the preparation region, thus we obtained a spatial study to see if the TEC was instantly affected above a large area around the earthquake location [226]. We examine the spatial distribution anomalies prior to the seismic event as well as those that happened post to the seismic event to confirm the TEC anomalies related to the seismic event, in addition to their temporal and spatial fluctuations.

6.3. Monte-Carlo Simulation

In this research, we will use Monte Carlo simulation as a simulation method shown in **Figure 6.7.** Flow chart of simulation.. Any analytical procedure aiming to mirror a real-life system is referred to as simulation. This is especially true when other studies are too mathematically difficult to replicate. Clearly, flipping a coin thousands of times will give us an approximation of how frequent heads and tails are for a specific coin. However, it is illogical to believe that flipping the coin millions of times can provide information about what is going on in a nuclear reactor, the weather tomorrow, or the current recession. MCS is fundamentally a series of coin flips that can be used to investigate these and other areas. Because Monte Carlo (MC) simulations are stochastic procedures that rely on random numbers and probability statistics. A complicated system's simulation model can only be a rough representation of the real thing. Monte Carlo simulation creates a model of possible outcomes by assigning random values to each input variable from a predetermined distribution of all possible values. The model then recalculates the results using a new set of random values drawn from the probability distribution of the defined variable, this sampling approach is known as Markov sampling which in [227–229], more information about Markov sampling and its uses with MC technique can be found. The purpose of Monte Carlo methods is to:

A) Generate samples $\{x^{(r)}\}_{r=1}^{R}$ from a specified probability distribution $P(x)$.

B) Estimate the functions' expected values under this distribution, for example.

$$\Phi = \langle \phi(x) \rangle \equiv \int d^N x \, P(x) \;\; \phi(x) \tag{66.20}$$

The second aim can be obtained with the random samples $\{x^{(r)}\}_{r=1}^{R}$ to obtain the estimator

$$\hat{\Phi} = \frac{1}{R} \sum_{r} \phi(x^r) \tag{66.21}$$

If the vectors $\{x^{(r)}\}_{r=1}^{R}$ are produced from $P(x)$ then the expectation of $\hat{\Phi}$ is Φ. The variance of $\hat{\Phi}$ will decrease as samples number R rises $(\frac{\sigma^2}{R})$, where σ^2 is the variance of ϕ, so the accurateness of the Monte Carlo estimate depends only on the variance of ϕ, not on the space sampled dimensionality.

$$\sigma^2 = \int d^N x \, P(x) (\phi(x) - \Phi)^2 \tag{66.22}$$

A pseudo-random number generator, often known as RNG, is a deterministic computer program that generates a series of integers that resemble true random samples in many ways. Most RNGs sample positive integer values between 0 and N in a uniform manner, most RNGs allow N to be large enough. A RNG sample is divided by N to sample the uniform distribution on [0,1]. The double precision numbers between 0 and 1 are uniformly sampled by this method.

The linear congruential generator (LCG) is a popular pseudo-random number generator (RNG). It is simple to comprehend and implement. n^{th} sample, L_n, the other sample is

$$L_{n+1} = (aL_n + b) \bmod c \tag{66.23}$$

For the best results, a, b, and c must be carefully chosen. The LCG takes a "seed" L_0 and generates a series of numbers that, depending on the values of a, b, and c, can satisfy the Monte Carlo criteria. Our random numbers must meet three criteria for this method to succeed:

1) They need to be distributed uniformly.
2) They must be uncorrelated.
3) We need a lot of points.

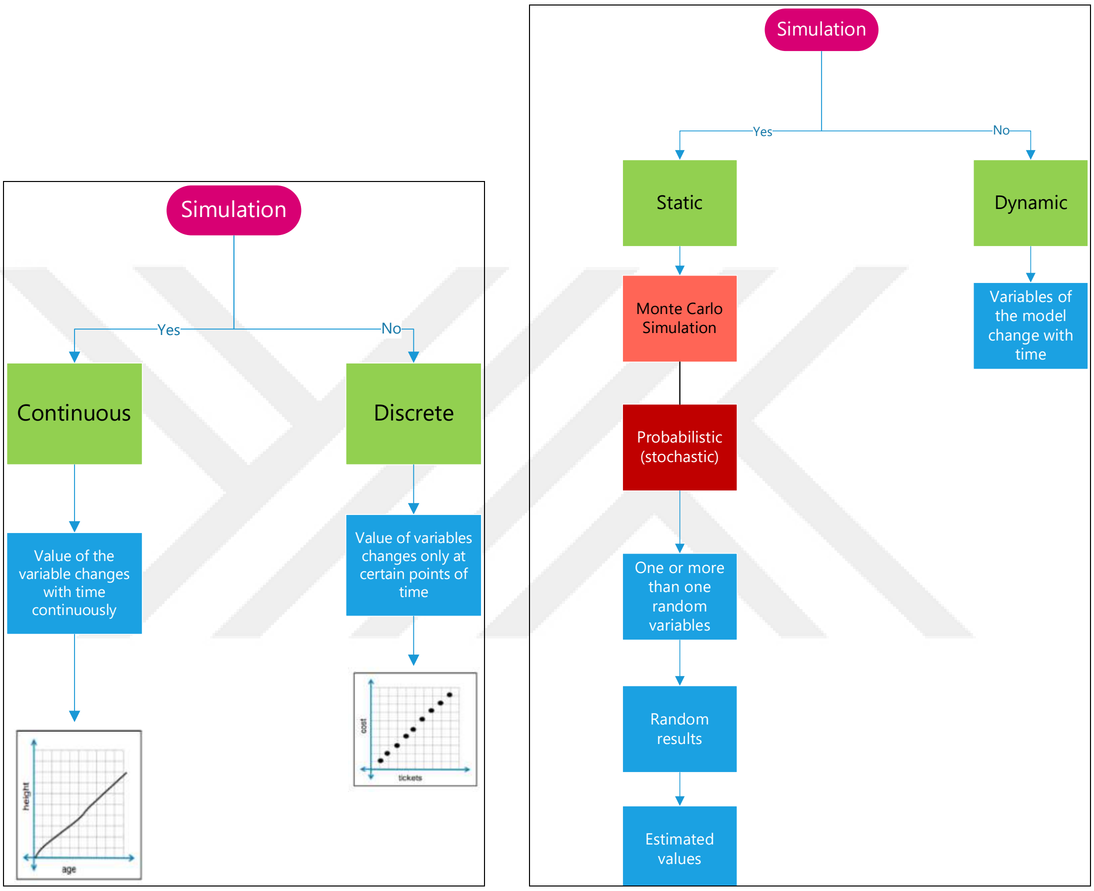

Figure 6.7. Flow chart of simulation.

6.4. Radon and TEC Correlation

The statistical relationship between Rn-222 and TEC can be obtained using cross correlation analysis. Cross correlation is a metric that measures how two data series move in relation to one another. The data differs from -1 to 1, so the nearer the cross-correlation value is to 1, the closer the information sets are with each other. The goal of this study is to see if there is any correlation between TEC fluctuation anomalies and soil radon concentration. The cross correlations at *lag l* are as follows:

$$\rho_{ij}(l) = corr\left[z_{it}, z_{j,t+l}\right] = \frac{\gamma_{ij}(l)}{\left\{\gamma_{ii}(0)\gamma_{jj}(0)\right\}^{1/2}} \qquad (66.24)$$

with $\gamma_{ii}(0) = \text{var}[z_{it}]$. Thus, for $i \neq j, \rho_{ij}(l) = \rho_{ji}(-l)$ represents the function of cross-correlation among the two series z_{it} and z_{jt}. The $k \times k$ cross-correlation matrix $\rho(l)$ at $lag\, l$, with $(i, j)^{th}$ element equal to $\rho_{ij}(l)$, , is obtained by

$$\rho(l) = \mathbf{V}^{-1/2}\mathbf{\Gamma}(l)\mathbf{V}^{-1/2} = \{\rho_{ij}(l)\} \tag{66.25}$$

Furthermore, the $\mathbf{\Gamma}(l)$ and $\rho(l)$ cross-covariance and cross-correlation matrices have the feature of nonnegative definiteness, because

$$\text{var}\left[\sum_{i=1}^{n} \boldsymbol{b}_i' \boldsymbol{Z}_{t-i}\right] = \sum_{i=1}^{n}\sum_{j=1}^{n} \boldsymbol{b}_i' \mathbf{\Gamma}(i-j)\boldsymbol{b}_j \geq 0 \tag{66.26}$$

In **Figure 6.8** the cross correlations $\rho_{ij}(l)$, of this progression are shown, up to 18 lags [230],

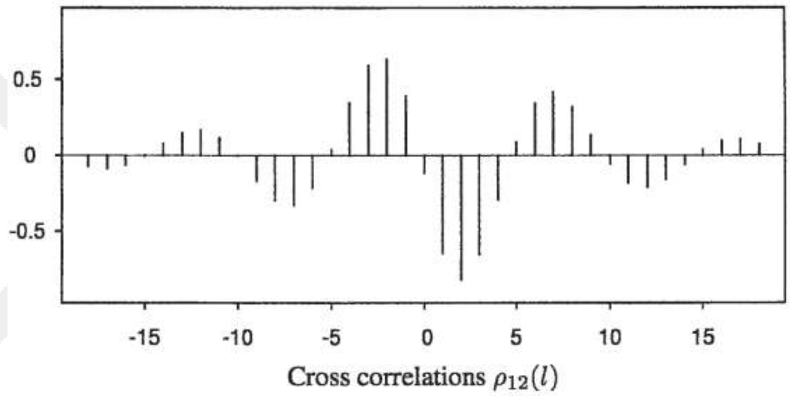

Figure 6.8. Theoretical cross correlations $\rho_{ij}(l)$, for the bivariate AR (1) process example: cross correlations $\rho_{12}(l)$.

7. RESULTS AND DISCUSSION

7.1. ARIMA and MC Simulations

In this section, the obtained results for ARIMA and MC simulations for Radon and TEC data are given in two subsections as follows.

7.1.1. Radon Results

The Radon time series was modelled using autoregressive integrated moving average (ARIMA) models. In data investigations aimed to determine the number of the lag in an autoregressive model, the partial autocorrelation function (PACF) of time series plays a significant role. The usage of PACF was first established as part of the Box-Jenkins technique, in which the suitable lags p in an AR (p) model or an extended ARIMA (p, d, q) model might be denoted by graphing partial auto correlative functions. In this study, ARIMA (3, 1, 7) for Radon data without interpolation and ARIMA (7, 1, 3) for interpolated Radon data were used. AIC and BIC were used for selecting the best model. The future values were predicted using ARIMA forecast with an error bound width from the curve; it is ±2 standard deviations (upper and lower bounds). Ljung-Box Test is utilized to check whether the fitted model residuals are independent and identically distributed random variables in ARIMA modelling. Augmented Dickey-Fuller test (ADFT) is used to ensure the time series stationarity of radon-222 data. **Figure 7.2** illustrates the ARIMA training fit and ARIMA forecast for radon-222 time series.

Subsequently, ARIMA model and Monte-Carlo simulation jointly are performed on radon data and interpolated radon data, then the results of both are compared. Some of the obtained results are as followings:

1- Radon data without interpolation

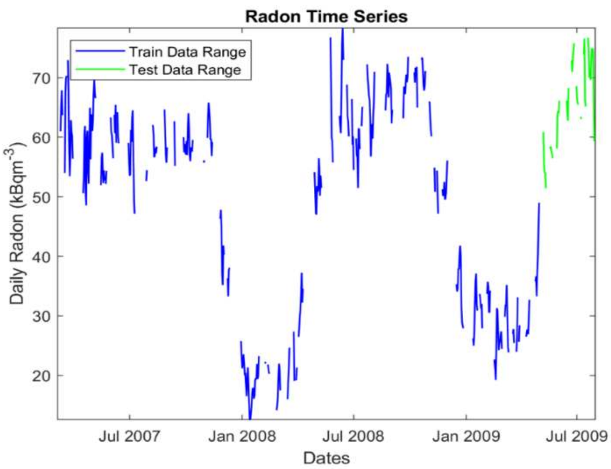

Figure 7.1. Time series plot of radon data, training (80%) and testing (20%) parts.

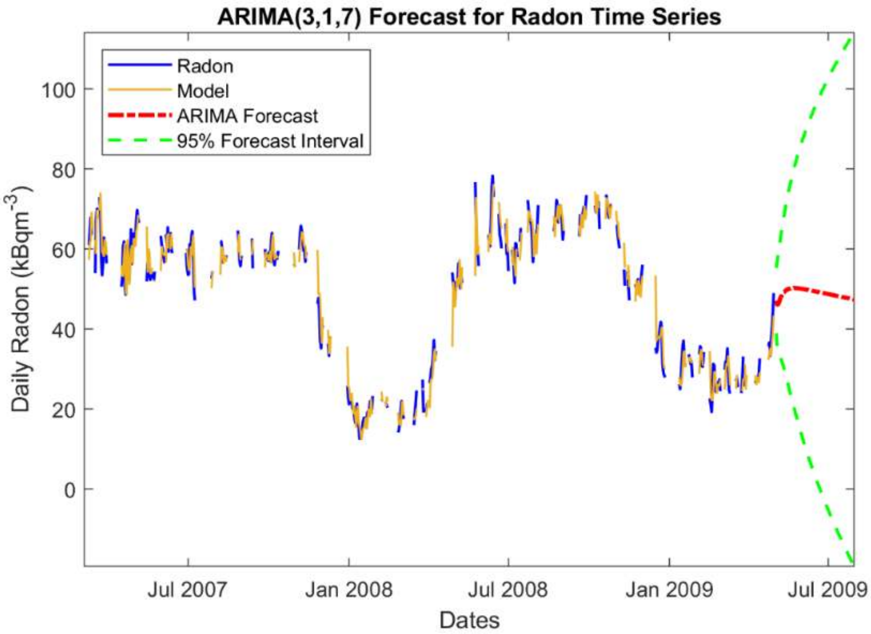

Figure 7.2. ARIMA (3,1,7) model fit and ARIMA forecast for radon time series.

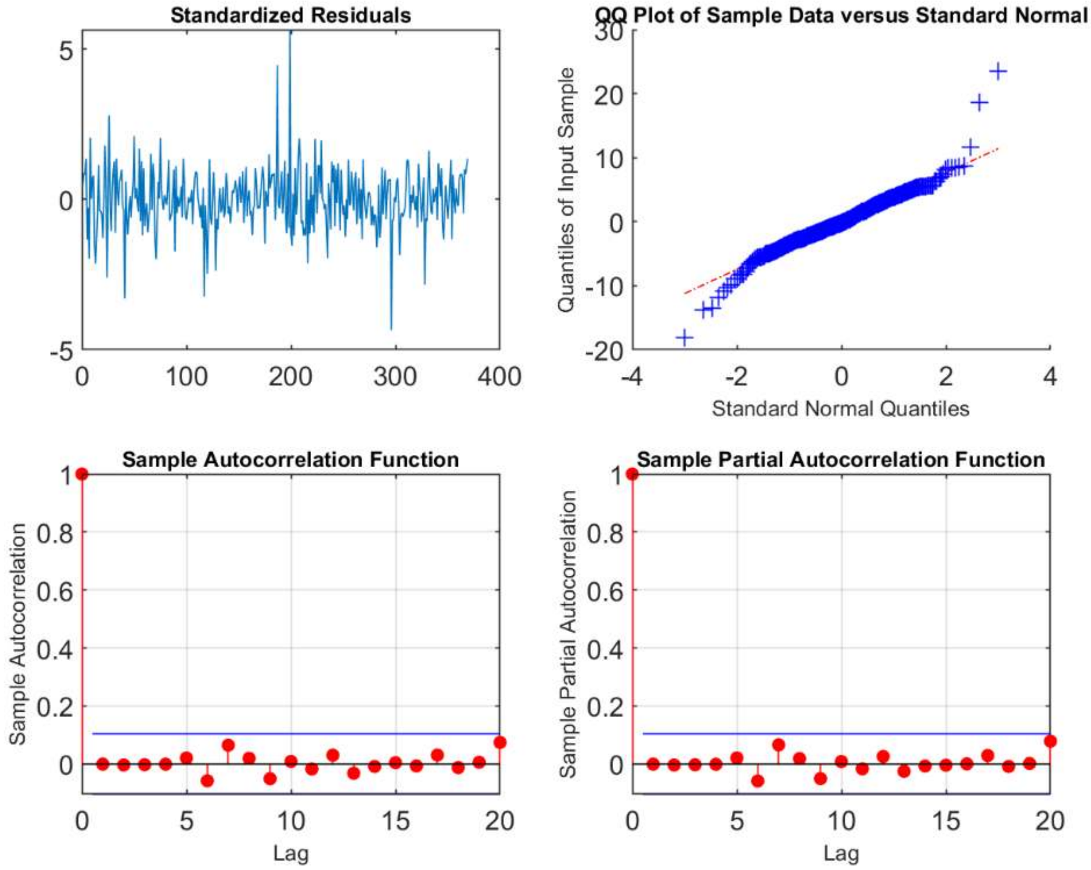

Figure 7.3. Plot of ARIMA model residuals for radon time series (up-left), residuals' quantile-quantile plot (up-right), sample ACF of the residuals (down-left) and sample PACF of the residuals (down-right).

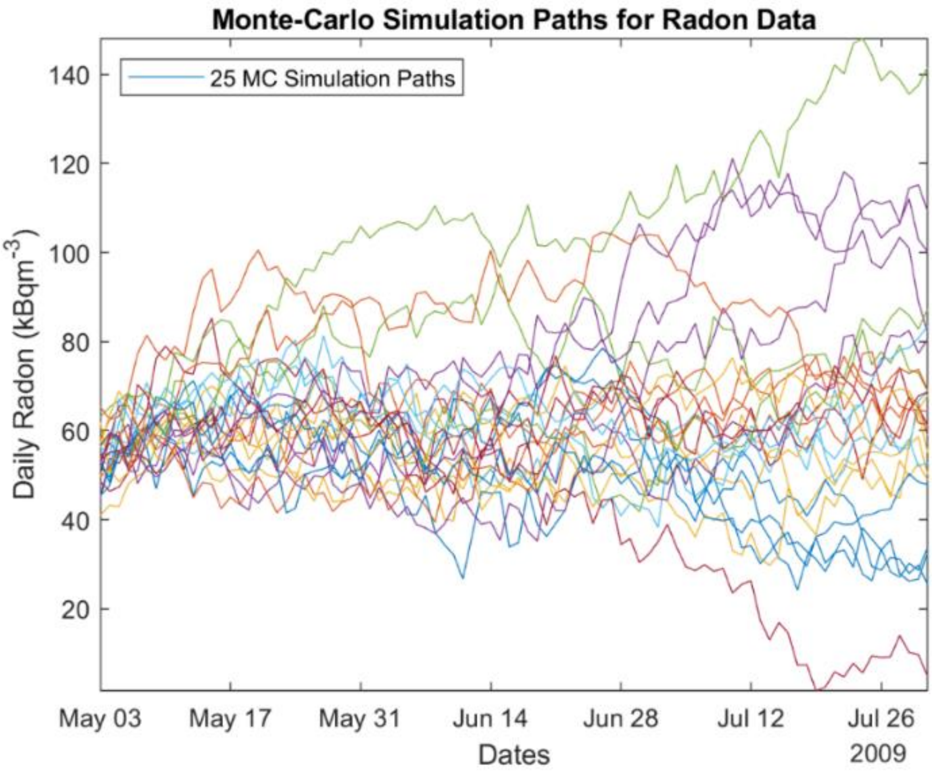

Figure 7.4. Monte-Carlo simulation paths on ARIMA model forecast for radon time series.

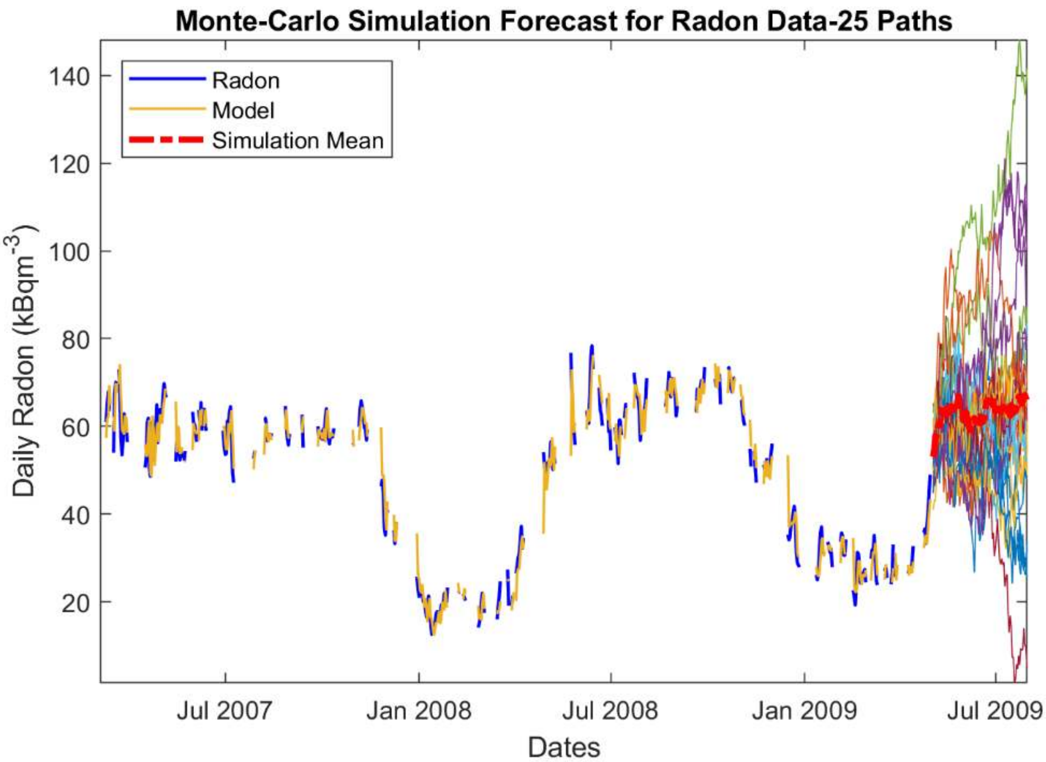

Figure 7.5. Monte-Carlo simulation paths and simulation mean for radon time series.

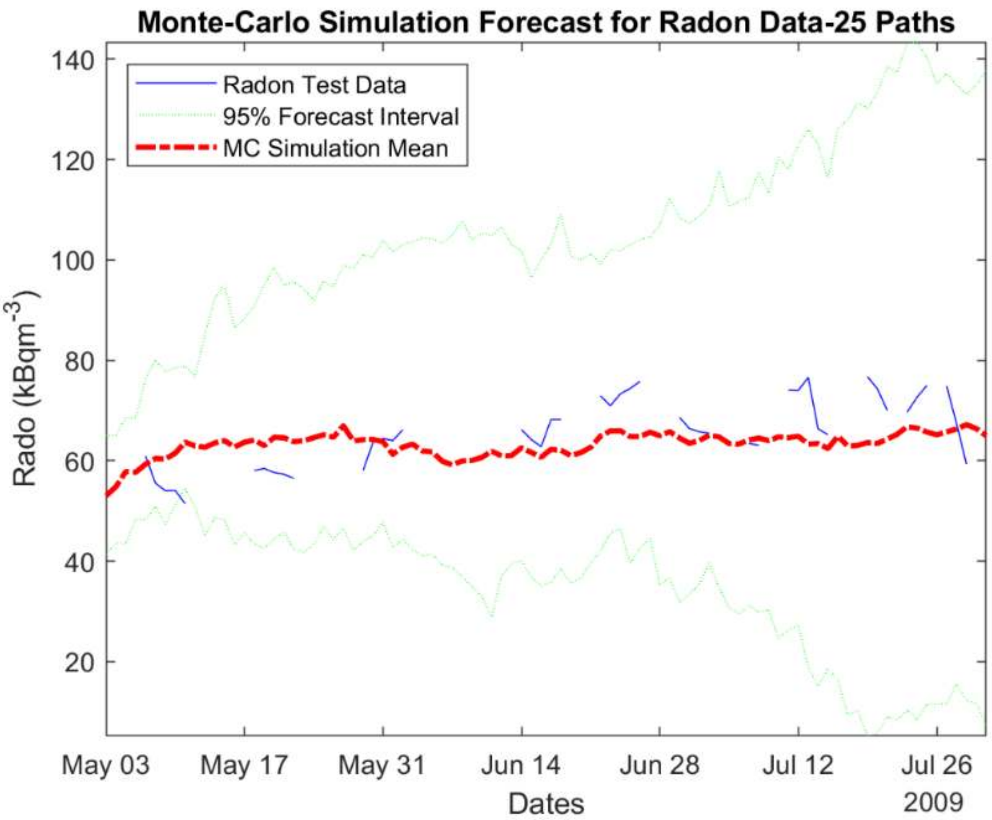

Figure 7.6. Monte-Carlo simulation mean for radon time series.

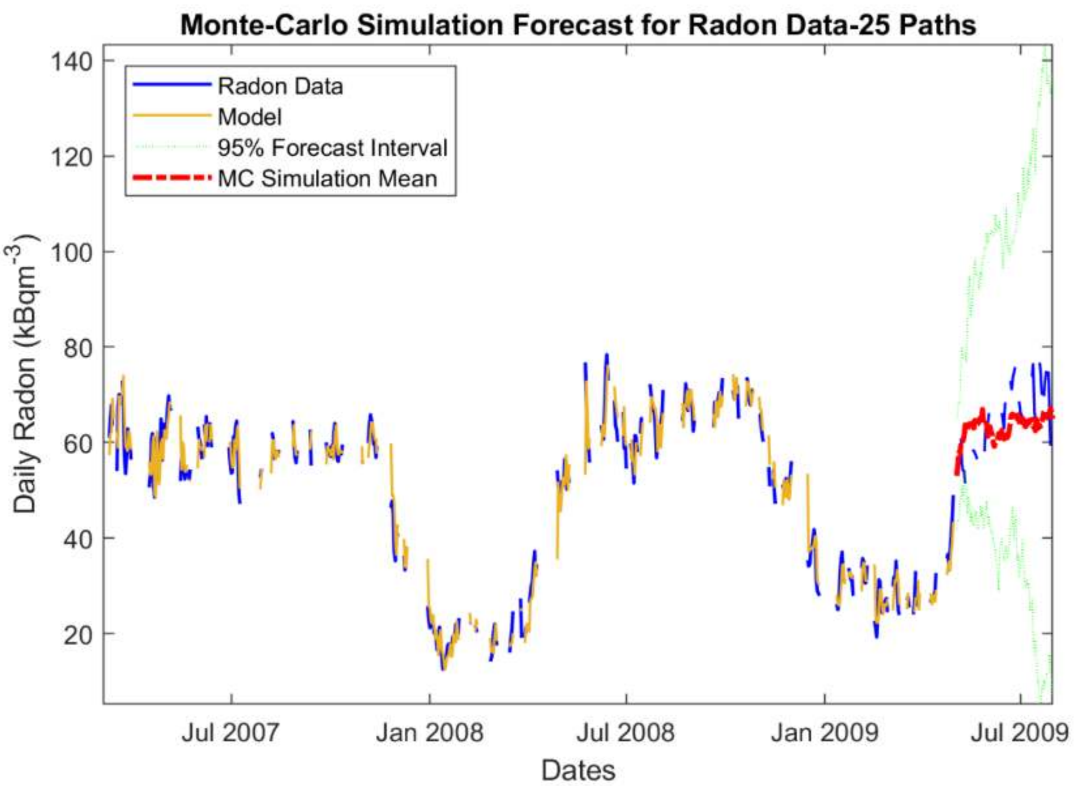

Figure 7.7. ARIMA model fit and Monte-Carlo simulation mean for radon time series.

Figure 7.1-7 shows the results for the radon time series, the radon data is divided into two parts, training (80%) and testing (20%) parts as shown in **Figure 7.1**. Then the Augmented Dickey-Fuller Test (ADFT) is taken for the training section to verify the stationarity of the Rn-222-time series. Because of the non-stationarity of the training radon, the first difference was taken, then an ADF test applied on training data and stationarity was obtained. After many trails, a proper ARIMA model (for Gaussian Distribution) was selected which Sample Autocorrelation (ACF) and Partial Autocorrelation (PACF) were considered in the model selection. ARIMA (3,1,7) model and ARIMA forecast was obtained for radon time series as illustrated in **Figure 7.2**. Moreover, histogram, quantile-quantile plot, sample ACF and sample PACF of the residuals, squared residual sample (ACF) were obtained as shown in **Figure 7.3**. Finally, Monte-Carlo simulation applied on ARIMA model forecast to enhance forecasted radon data as displayed in **Figure 7.4** and **Figure 7.5**. Therefore, the forecasted radon data was simulated and simulation mean calculated for 25 MC simulation paths as shown in **Figure 7.6** and **Figure 7.7**.

2- Radon data with interpolation

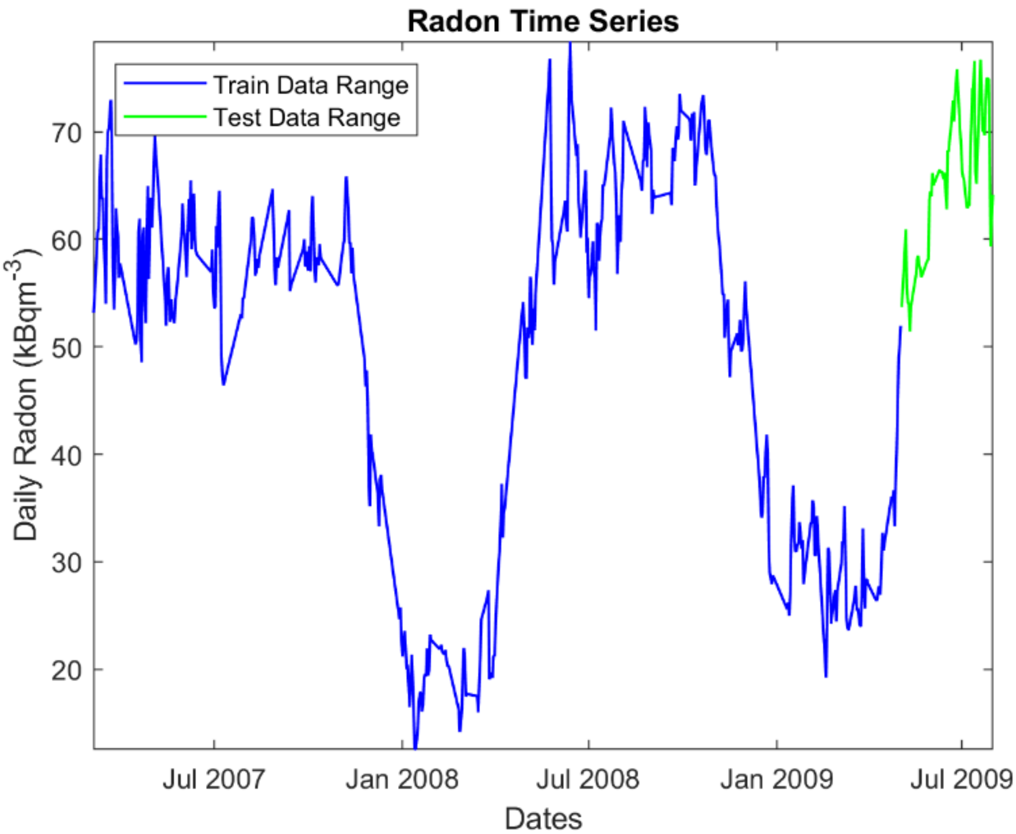

Figure 7.8. Time series plot of interpolated radon data, training (80%) and testing (20%) parts.

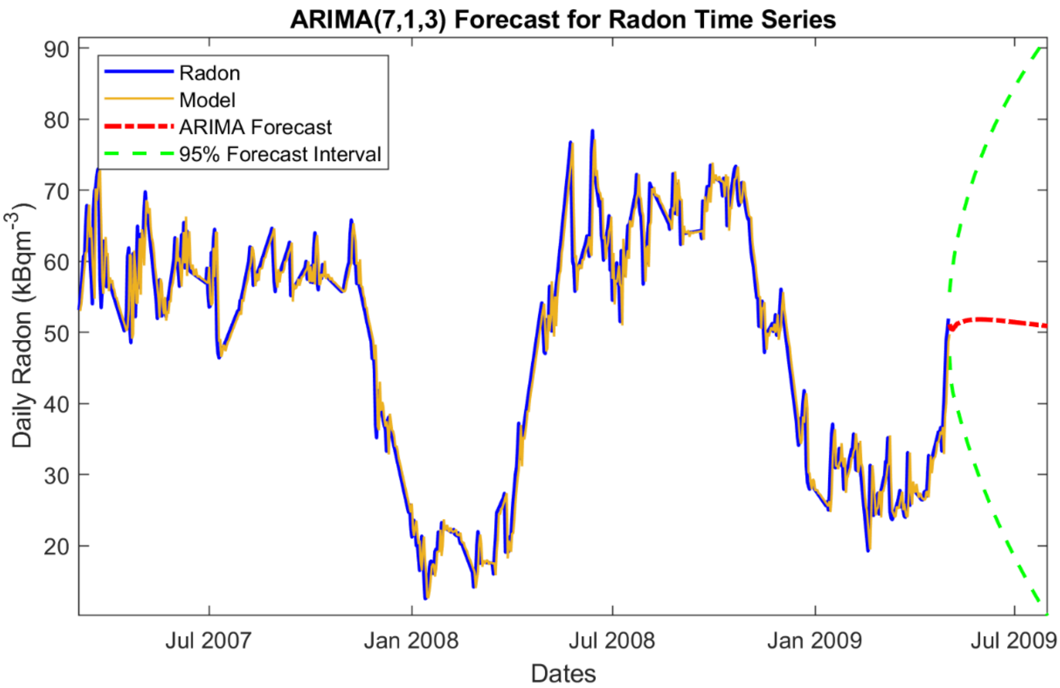

Figure 7.9. ARIMA (7,1,3) model fit and ARIMA forecast for interpolated radon time series.

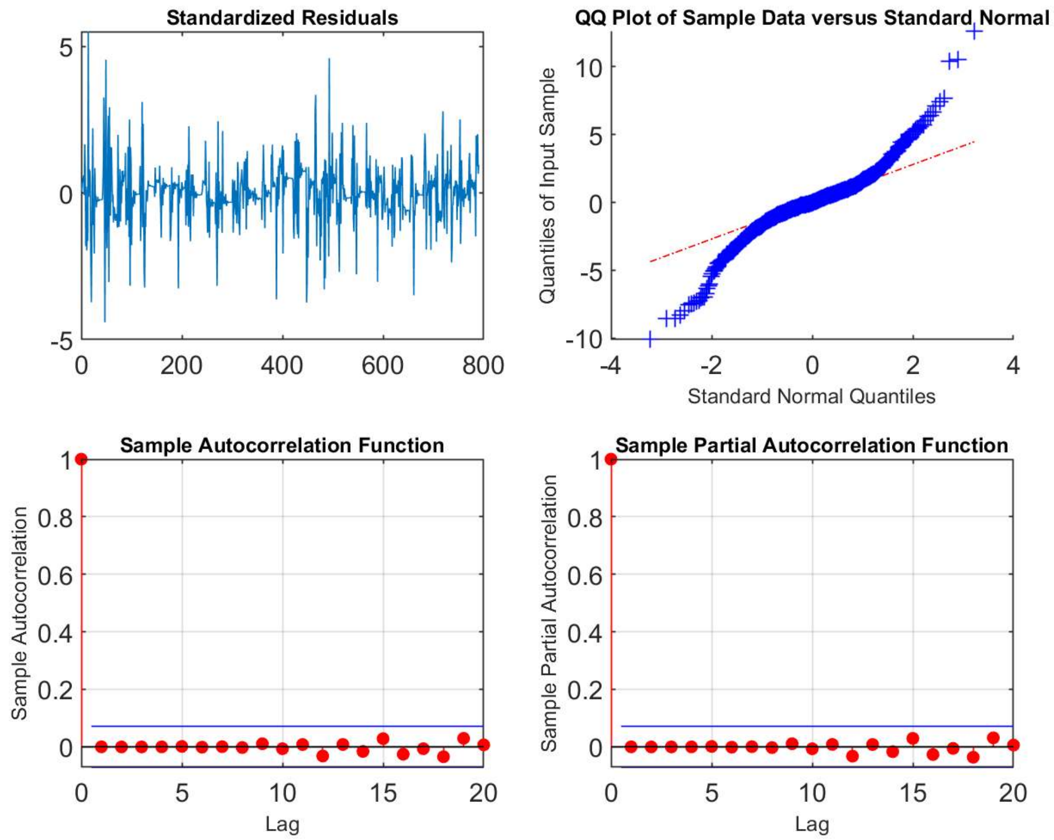

Figure 7.10. Plot of ARIMA model residuals for interpolated radon time series (up-left), residuals' quantile-quantile plot (up-right), sample ACF of the residuals (down-left) and sample PACF of the residuals (down-right).

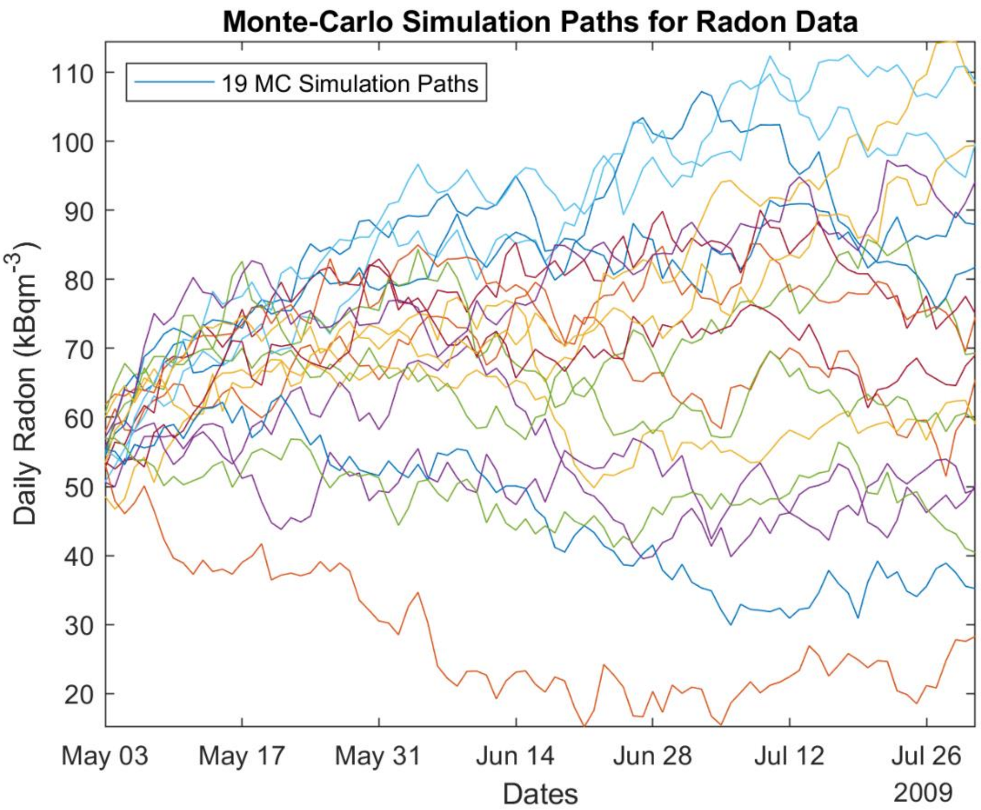

Figure 7.11. Monte-Carlo simulation paths on ARIMA model forecast for interpolated radon time series.

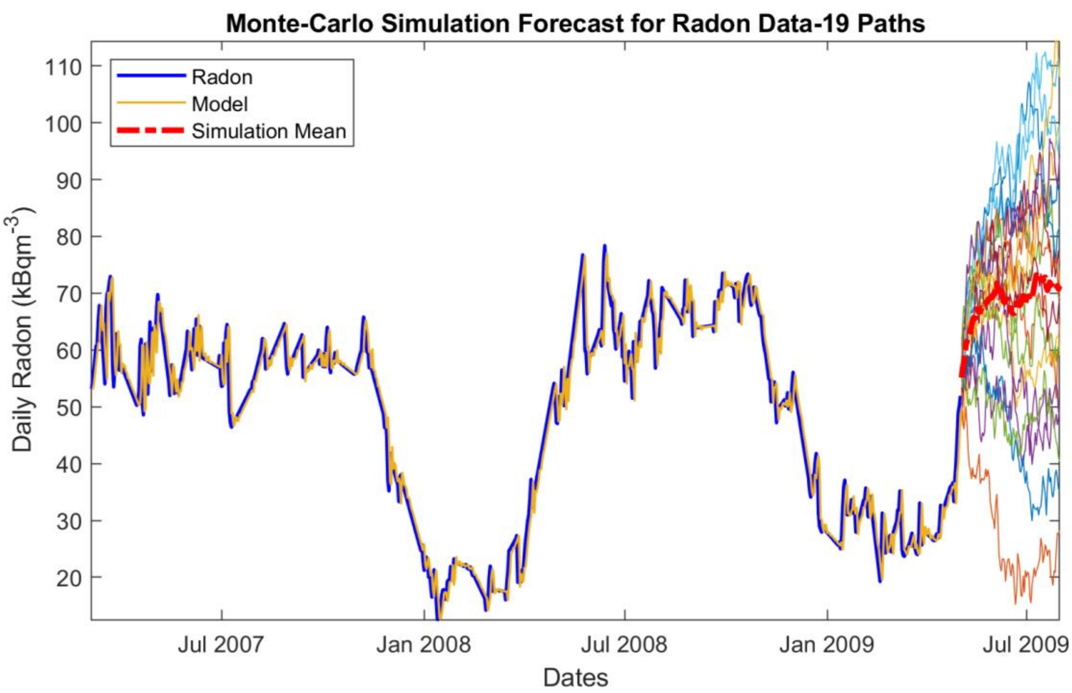

Figure 7.12. Monte-Carlo simulation paths and simulation mean for interpolated radon time series.

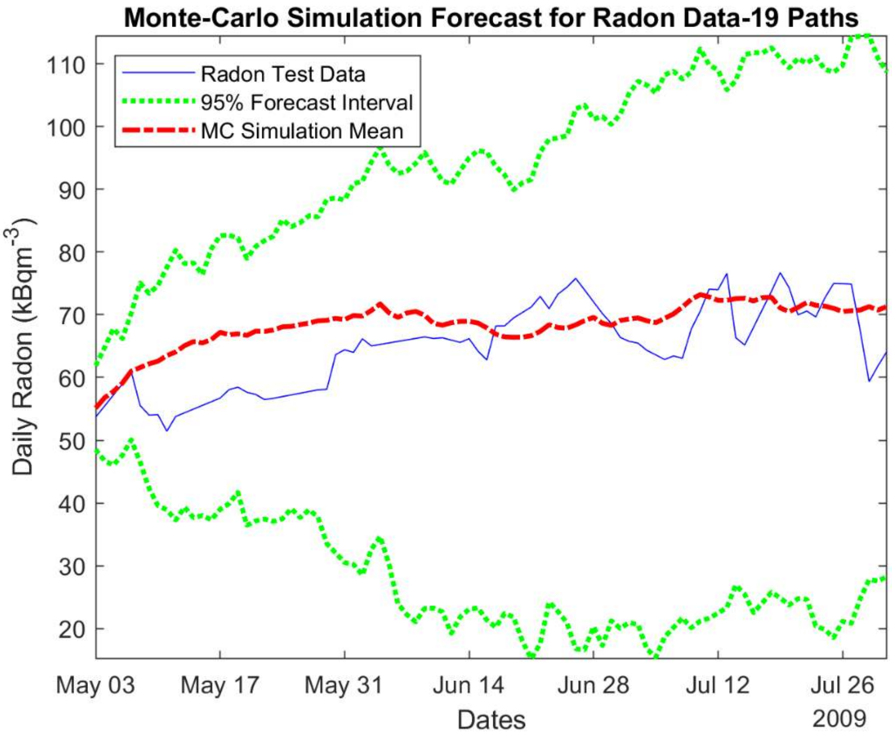

Figure 7.13. Monte-Carlo simulation mean for interpolated radon time series.

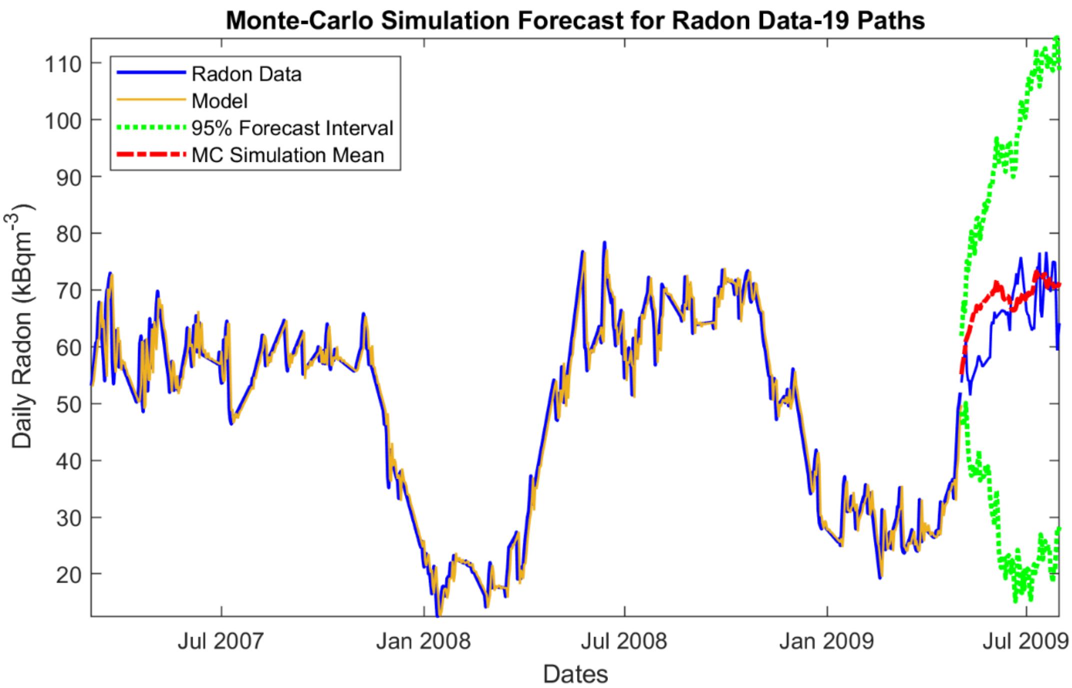

Figure 7.14. ARIMA model fit and Monte-Carlo simulation mean for interpolated radon time series.

Figure 7.8-14 demonstrates the results for the interpolated radon time series; the interpolated radon data is divided into two parts, training (80%) and testing (20%) parts as shown in **Figure 7.8**. Similarly, the Augmented Dickey-Fuller Test (ADFT) is taken for the training section to verify the stationarity of the Rn-222 time series. Because of the non-stationarity of the training Rn-222, the first difference was taken, then an ADF test applied on training data and stationarity was obtained.

Subsequently, a proper ARIMA model was selected which sample Autocorrelation (ACF) and Partial Autocorrelation (PACF) were considered in the model selection as displayed in **Figure 7.9**. ARIMA (7,1,3) model and ARIMA forecast was obtained for radon time series. Moreover, histogram, quantile-quantile plot, sample ACF and sample PACF of the residuals, squared residual sample (ACF) were obtained as illustrated in **Figure 7.10**. Finally, Monte-Carlo simulation applied on ARIMA model forecast to enhance forecasted radon data as shown in **Figure 7.11** and **Figure 7.12**. Therefore, the forecasted radon data was simulated and simulation mean calculated for 19 MC simulation paths as illustrated in **Figure 7.13** and **Figure 7.14**.

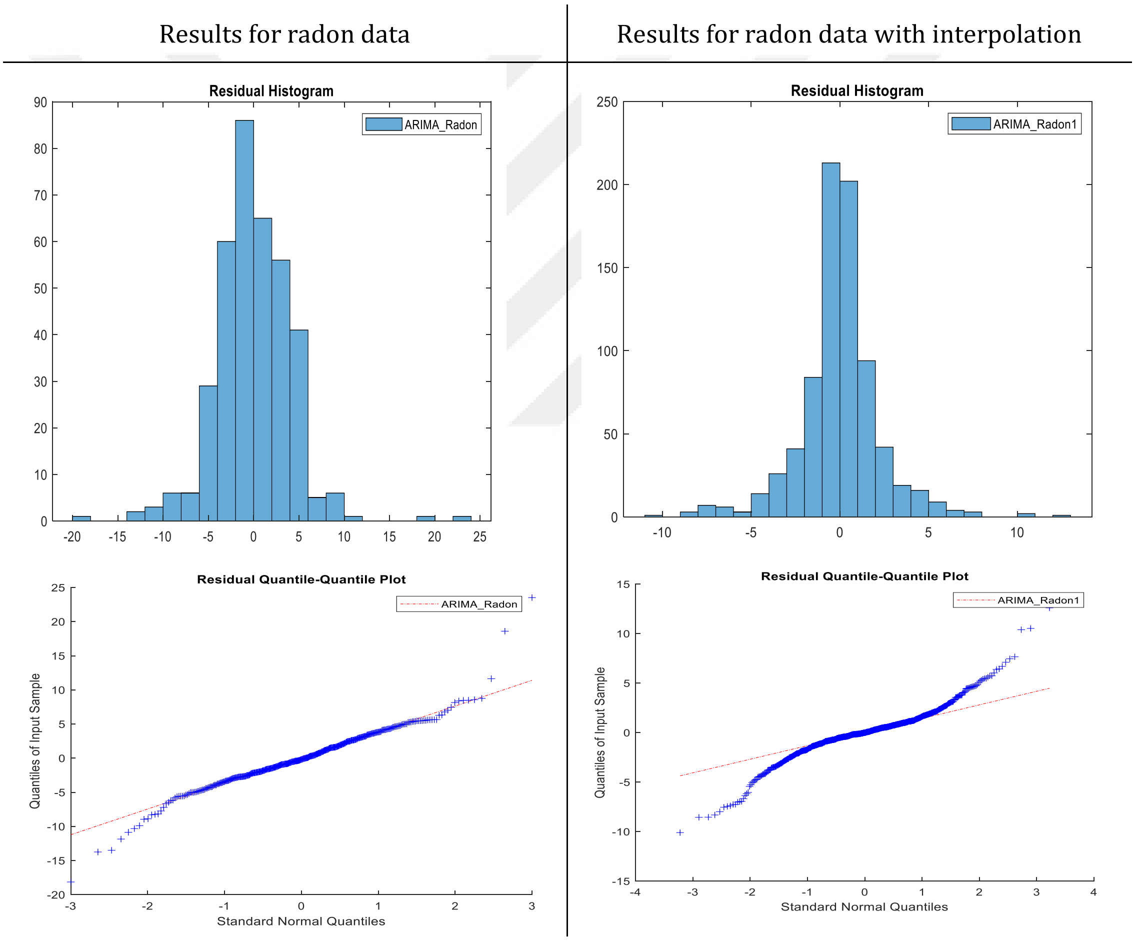

Figure 7.15. Comparison between the results of radon data and interpolated radon data of the same data range. Histogram and residuals' quantile-quantile plot of ARIMA model for radon time series

Figure 7.15 illustrates the comparison between the results of radon data and interpolated radon data of the same data range. From the Histogram and residuals' quantile-quantile plot of ARIMA model for radon time series, we can state that, the residuals of radon data better fitted with the standard normal quantile than the interpolated radon data. Also, the histogram of radon data compared to the interpolated one is closer to normal distribution. Certainly, modelling large data with missing values is not easy, because the data should be resampled, then during the modelling and sketching, we need manually to handle some steps to fix the missing ranges as shown in **Figure 7.16**.

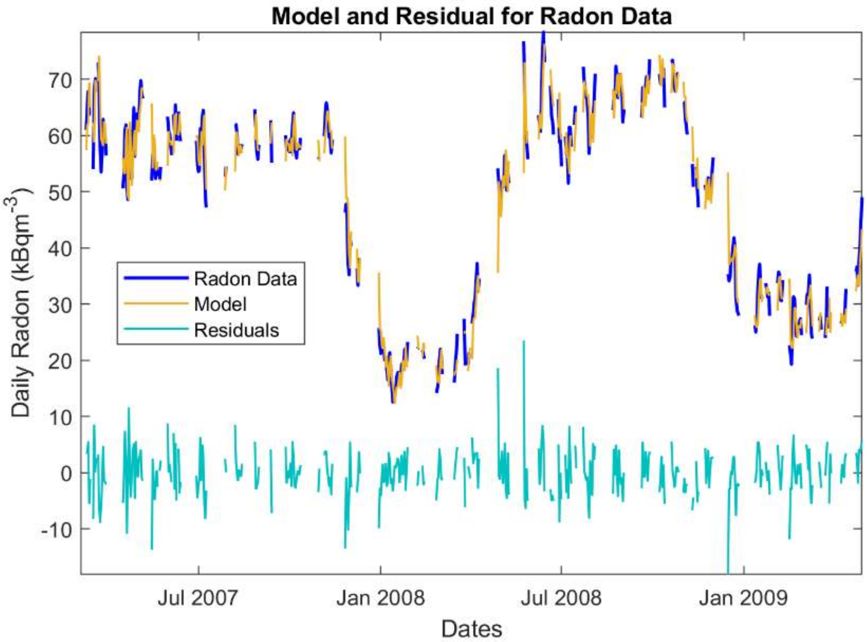

Figure 7.16. ARIMA model fit and Residuals of ARIMA model for the radon data with missing values.

7.1.2. VTEC Results

Similarly, The ARIMA model and Monte-Carlo simulation jointly are undertaken on TEC data. The following are the results obtained:

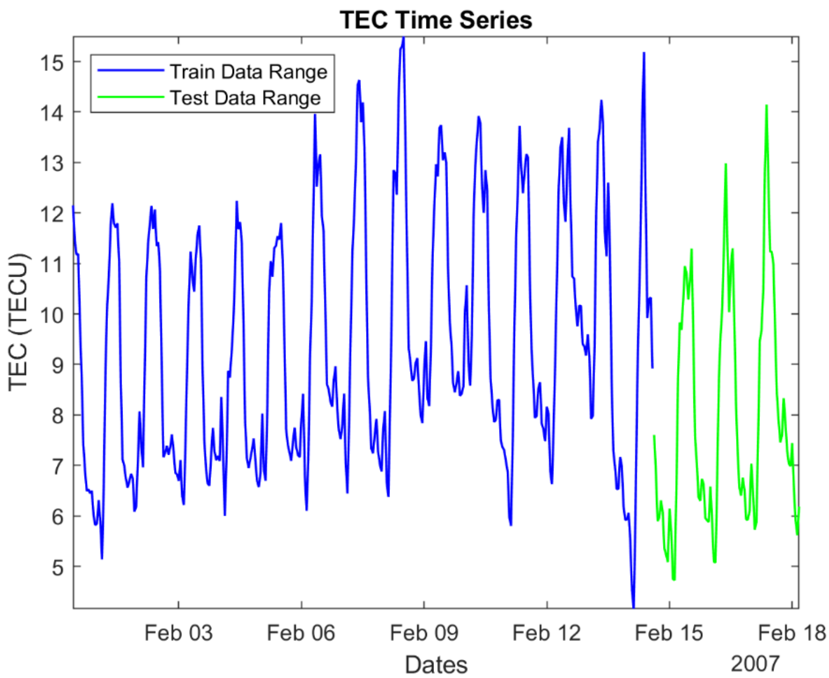

Figure 7.17. Time series plot of TEC data, training (80%) and testing (20%) parts.

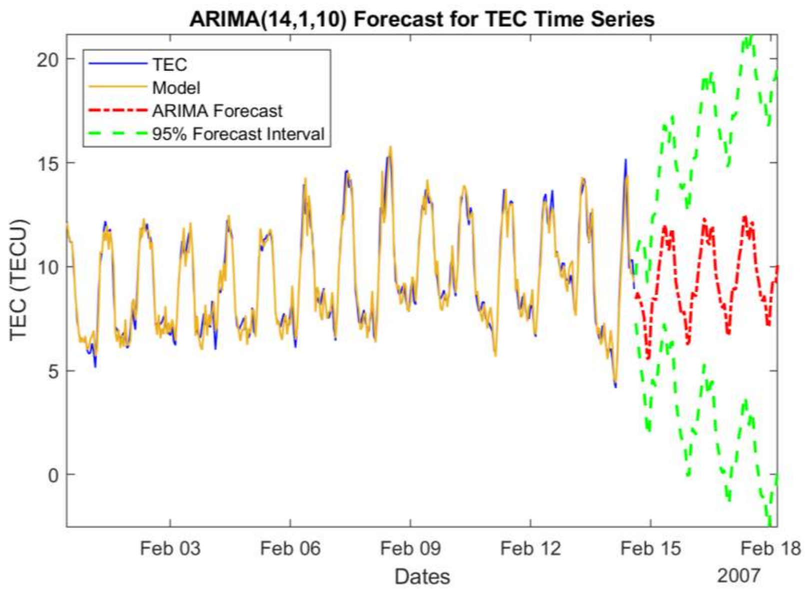

Figure 7.18. ARIMA (14,1,10) model fit and ARIMA forecast for TEC time series.

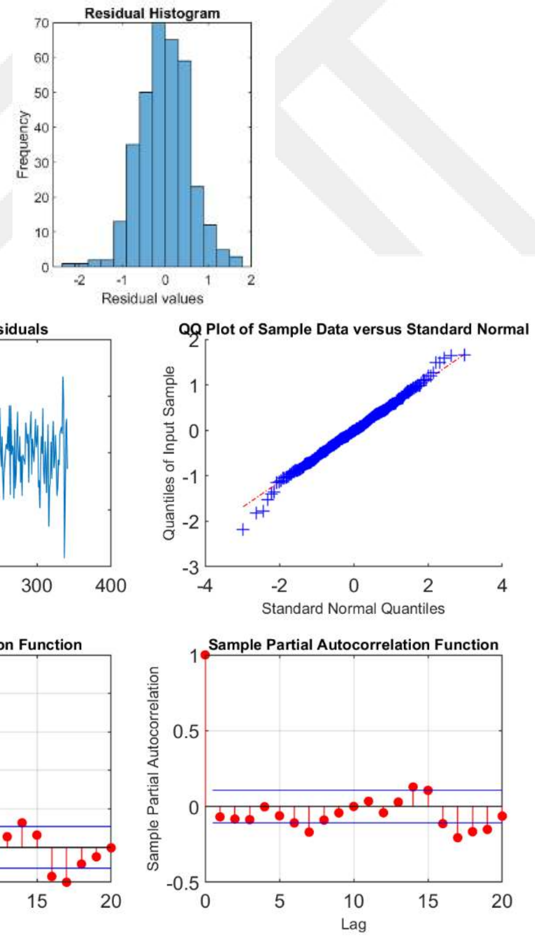

Figure 7.19. Histogram plot of the residuals of ARIMA model for TEC time series (top-middle), the residuals of ARIMA model for TEC time series (up-left), quantile-quantile plot of the residuals (up-right), sample ACF of the residuals (down-left) and sample PACF of the residuals (down-right).

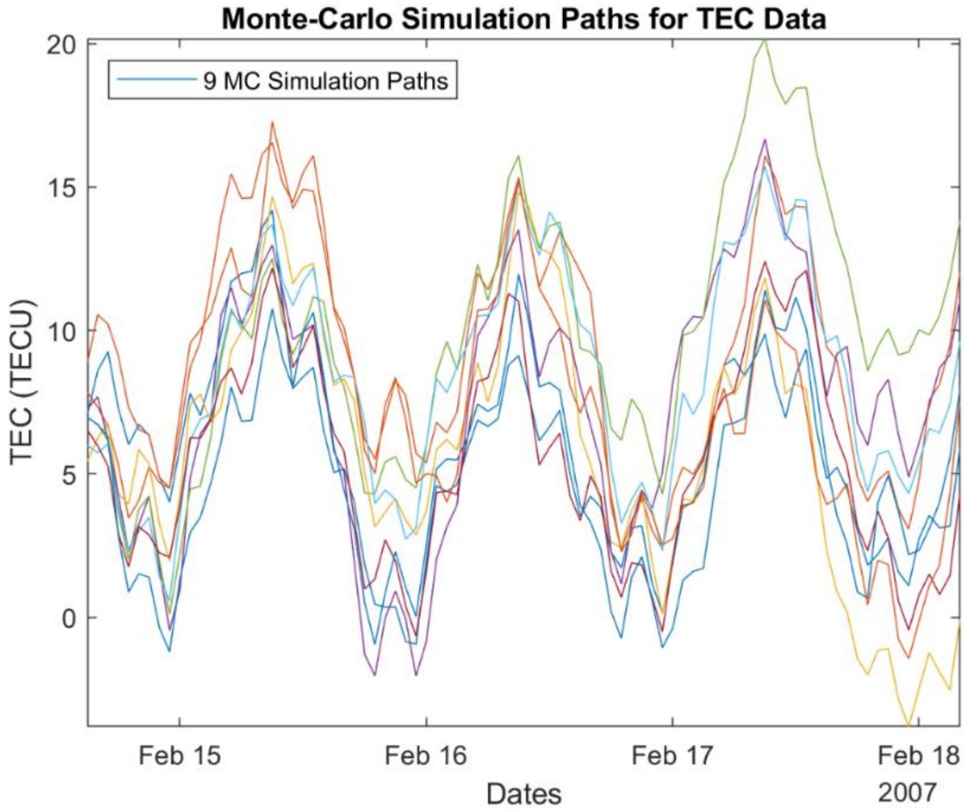

Figure 7.20. Monte-Carlo simulation paths on ARIMA model forecast for TEC time series.

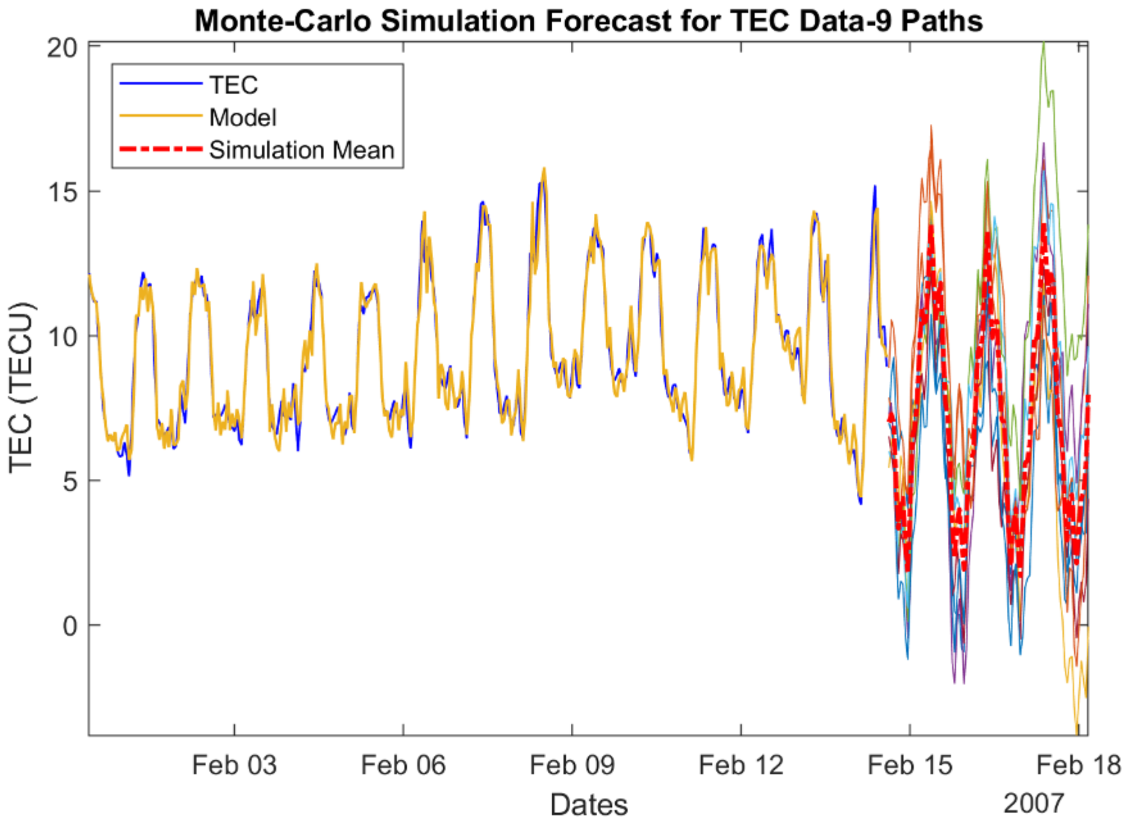

Figure 7.21. Monte-Carlo simulation paths and simulation mean for TEC time series.

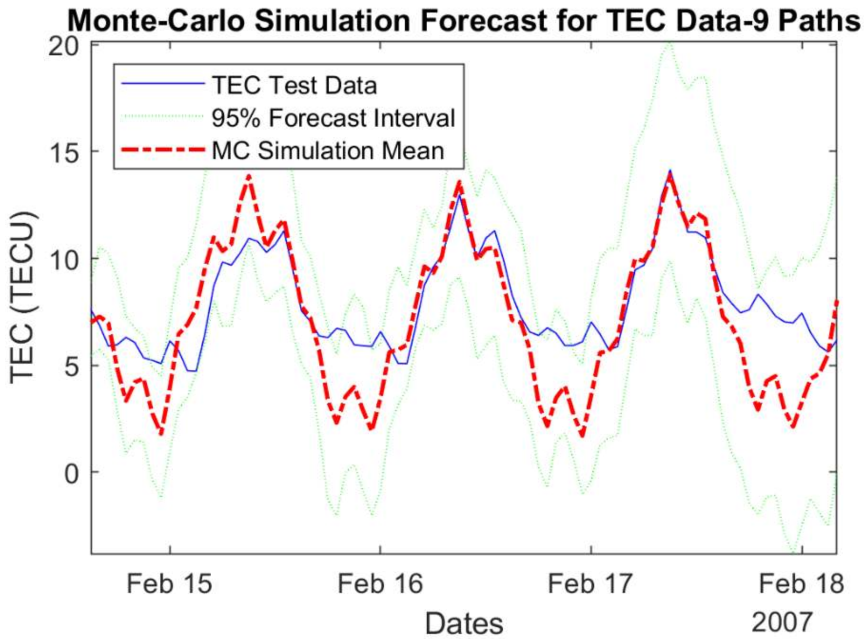

Figure 7.22. Monte-Carlo simulation mean for TEC time series.

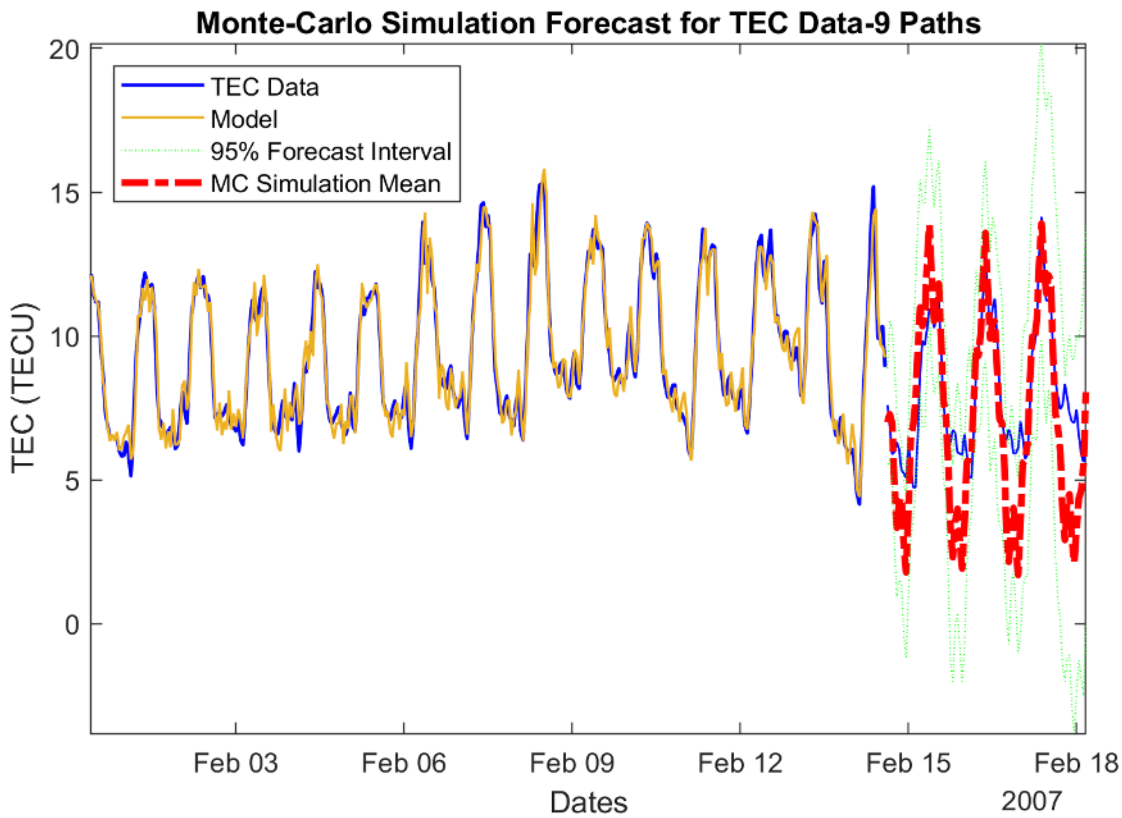

Figure 7.23. ARIMA model fit and Monte-Carlo simulation mean for TEC time series.

Figure 7.17-23 presents the TEC time series results, which are divided into two divisions: training (80%) and testing (20%) as displayed in **Figure 7.17**. In the training section, the Augmented Dickey-Fuller Test (ADFT) is used to verify the stationarity of the time series. Because the training data had been non-stationary, the first difference was obtained, then the ADF test was performed on the data, and stationarity was achieved.

Thereafter, a suitable ARIMA model was selected which sample Autocorrelation and Partial Autocorrelation were considered in the model selection as shown in **Figure 7.18**. For the TEC time series, the ARIMA (14,1,10) model and ARIMA forecast have been used. Moreover, histogram, quantile-quantile plot, sample ACF, sample PACF of the residuals, and squared residual sample (ACF) were achieved as illustrated in **Figure 7.19**. Finally, Monte-Carlo simulation was also used to improve the TEC data forecasted by the ARIMA model as displayed in **Figure 7.20** and **Figure 7.21**. The forecasted TEC data was simulated by 9 simulation paths, and the simulation mean was calculated as illustrated in **Figure 7.22** and **Figure 7.23**.

7.2. Multi-LR

Form the outcomes of multiple regression model, the regression coefficients can be imported to the multi-regression and multi-ANN equation as shown:

$$Rn_{(222)} = 32.73 + 0.42\, T_{atm} + 0.41\, P_{atm} + 0.73\, T_{soil\_10cm} + \varepsilon_{Mreg} \quad (77.1)$$

$$Rn_{(222)} = 32.73 + 0.42\, T_{atm} + 0.41\, P_{atm} + 0.73\, T_{soil\_10cm} + \varepsilon_{Mreg\,(ANN)} + \varepsilon \quad (77.2)$$

Consequently, the multiple regression residuals as shown in **Figure 7.25** can be obtained from $\varepsilon_{Mreg\,(ANN)}$ using ANN model. Whereas ε is the error of integrated models' combination and enhancing the multi-regression and the ANN from the above equation. The predicted Radon data from the multi-regression equation are illustrated in **Figure 7.24** for train and test data. The product executed well during training and testing range. This can be linked to the high correlation of radon with the used meteorological parameters which previously the related correlogram presented.

The calculated R-squared of multi-regression forecast (0.93) for calculation of Equation (77.1) illustrates that the multivariate regression model can describe 93% of the Radon variance and the RMSE (11.3) gives an error of 11.3 kBqm^{-3}. Therefore, the multi-regression model is required to be improved through multi-ANN model which mention in the next section.

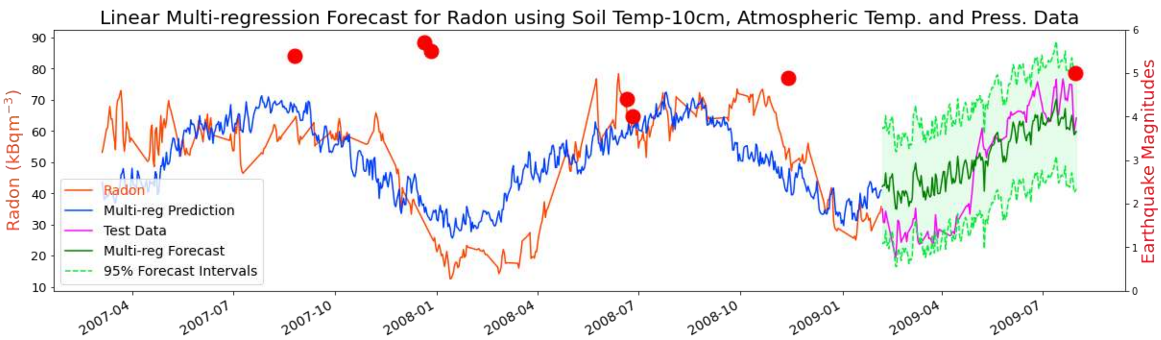

Figure 7.24. Shows the predicted radon data for multi-linear regression model and earthquake events.

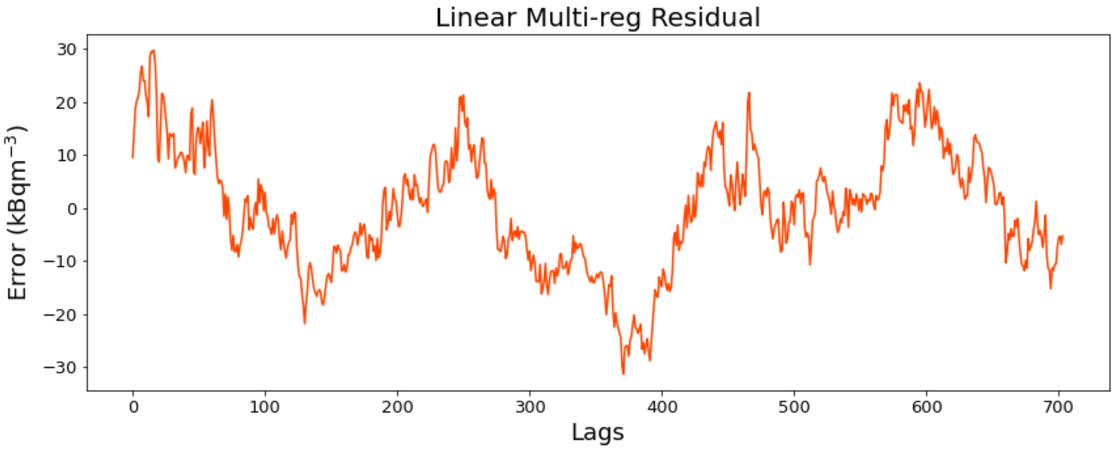

Figure 7.25. Shows the residuals of the predicted radon data for multi-linear regression model and earthquake events.

7.3. Multi-ANN and MC Simulation

As stated in section (6.1.3), we apply multi-ANN on the residuals ε_{Mreg} from the MLR model to enhance the predicted radon data as shown in **Figure 7.26**. In the **Figure 7.27**, the training and enhanced loss product of $\varepsilon_{Mreg}(ANN)$ are presented. The significant result was obtained after EPOCHS 86 training.

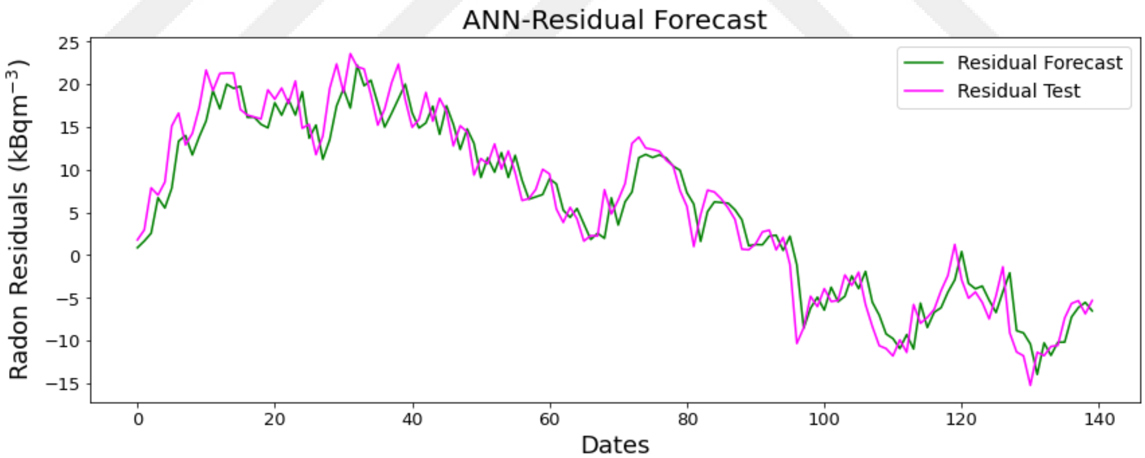

Figure 7.26. ANN forecast for residuals of MLR.

The multi-ANN model has meaningfully enhanced multiple data products. RMSE (4.21) is decreased and R-squared value (0.9745) is increased. It means, the multi-ANN model can describe 97.45% of the Radon variance and the RMSE (4.21) gives an error of 4.21 $kBqm^{-3}$.

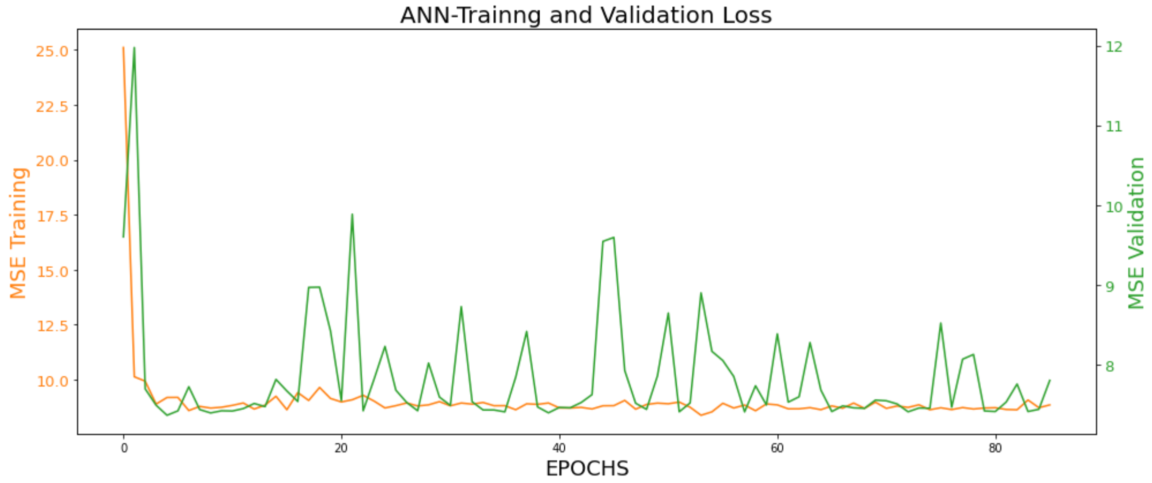

Figure 7.27. ANN training and validation loss on residuals of multi-regression model (MSE)

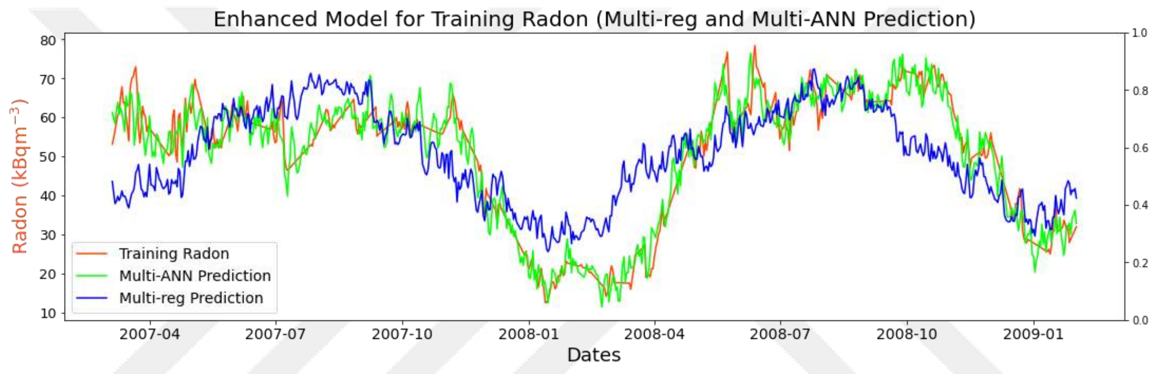

Figure 7.28. ANN training on Multi regression model residual.

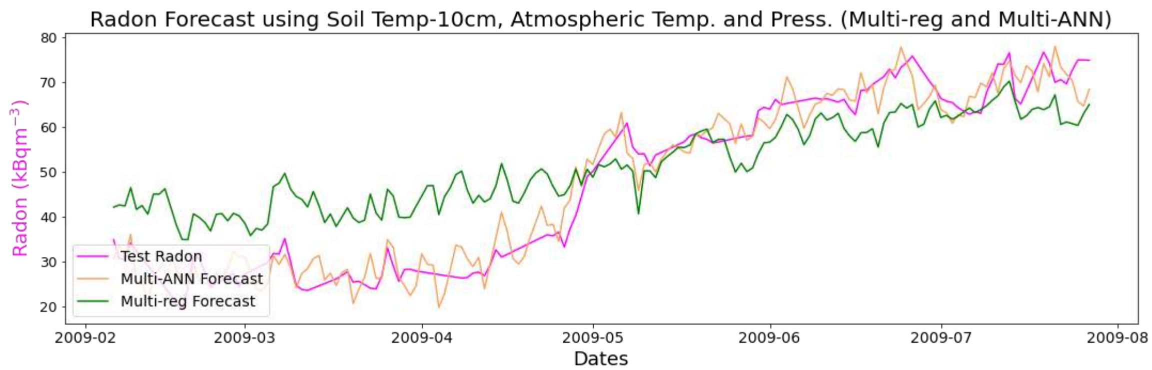

Figure 7.29. ANN validation loss on Multi regression model residual.

Then multi-ANN prediction data which illustrated in **Figure 7.28** and **Figure 7.29** is simulated within intervals. Thus, it is required to confirm that residuals of multi-ANN model are distributed normally. For this purpose, the residuals fitted with the theoretical quantile as shown in the **Figure 7.30**. From the **Figure 7.31**, we can see that residuals fit the normal distribution in a good manner. Therefore, the MC simulation can be applied to simulate radon data and to improve the data again as shown in **Figure 7.32**.

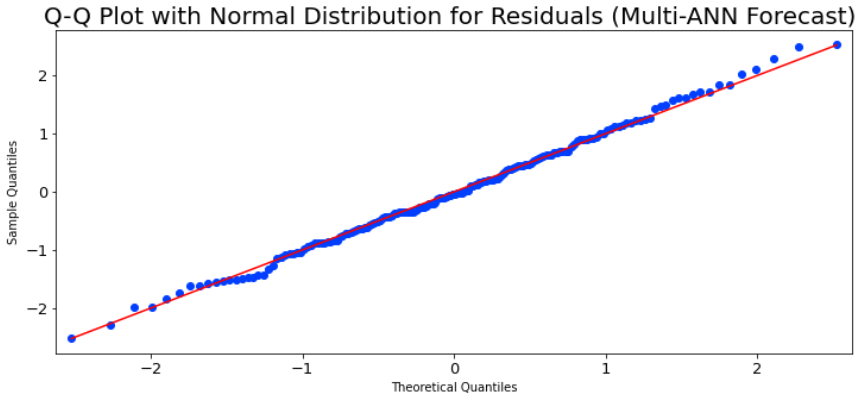

Figure 7.30. Q-Q plot of multi-ANN residuals.

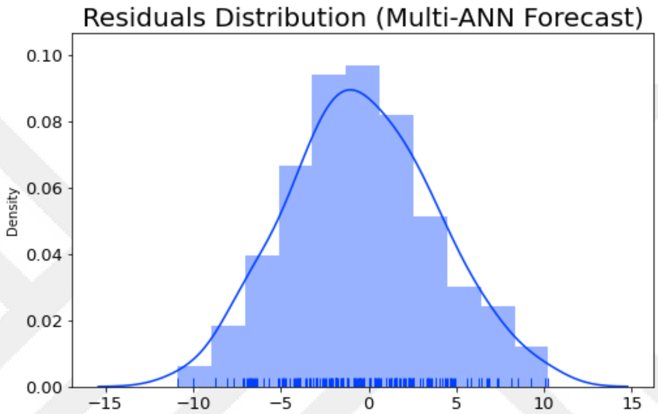

Figure 7.31. Histogram of Multi-ANN residuals.

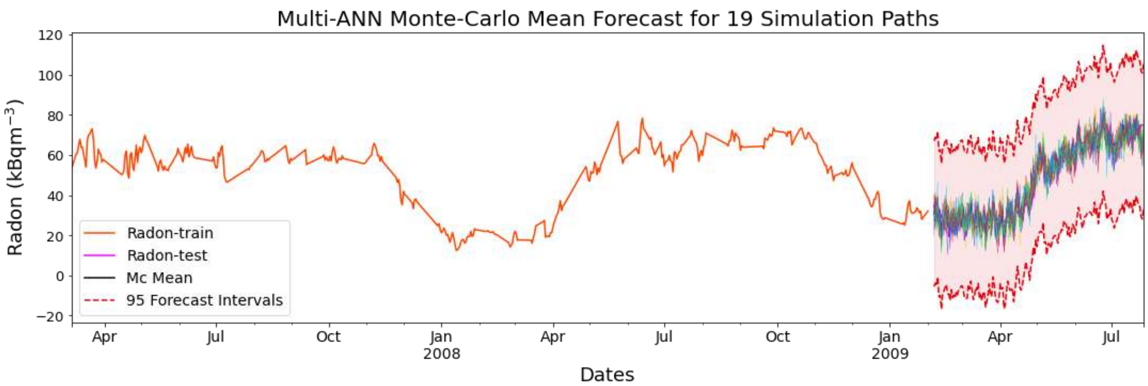

Figure 7.32. Rolling mean MC forecast for 19 simulation paths of the multi-ANN model.

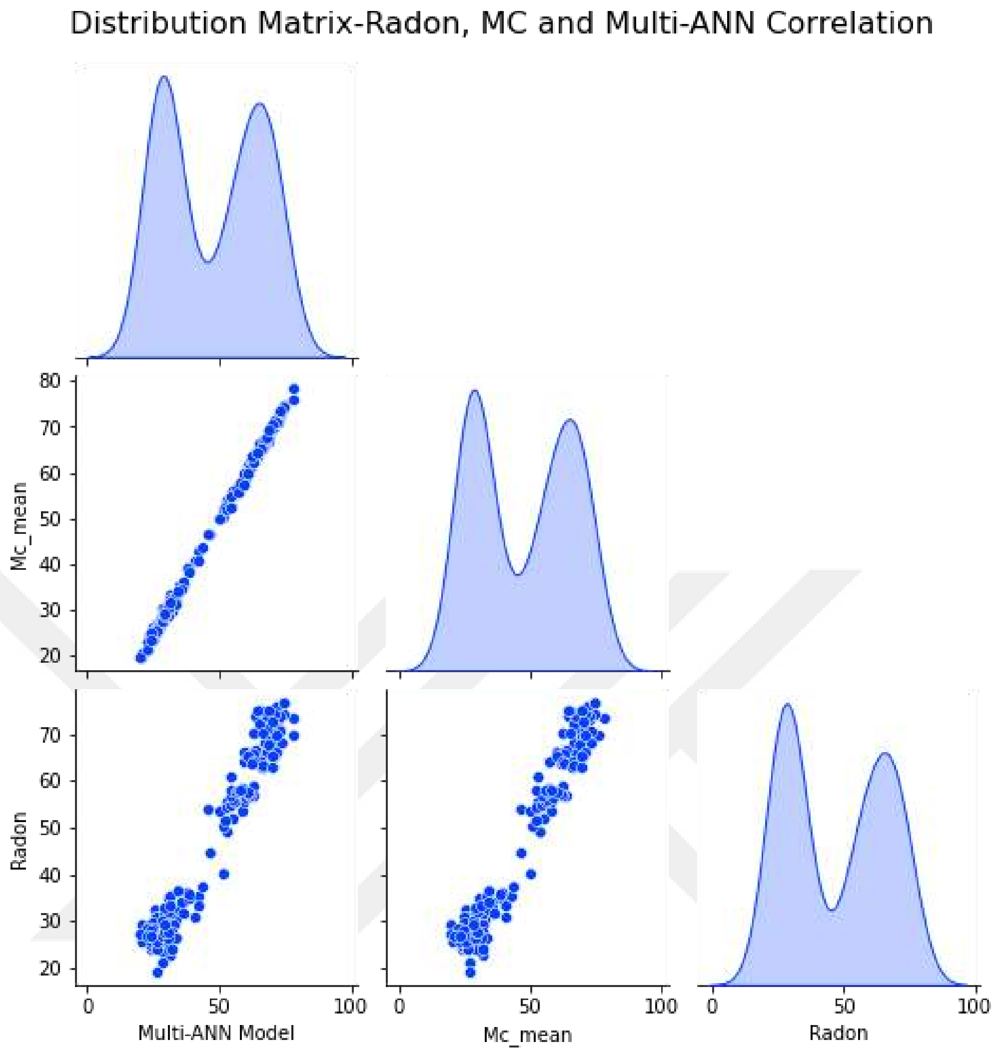

Figure 7.33. Scatter plot for radon, multi-ANN model, and MC mean.

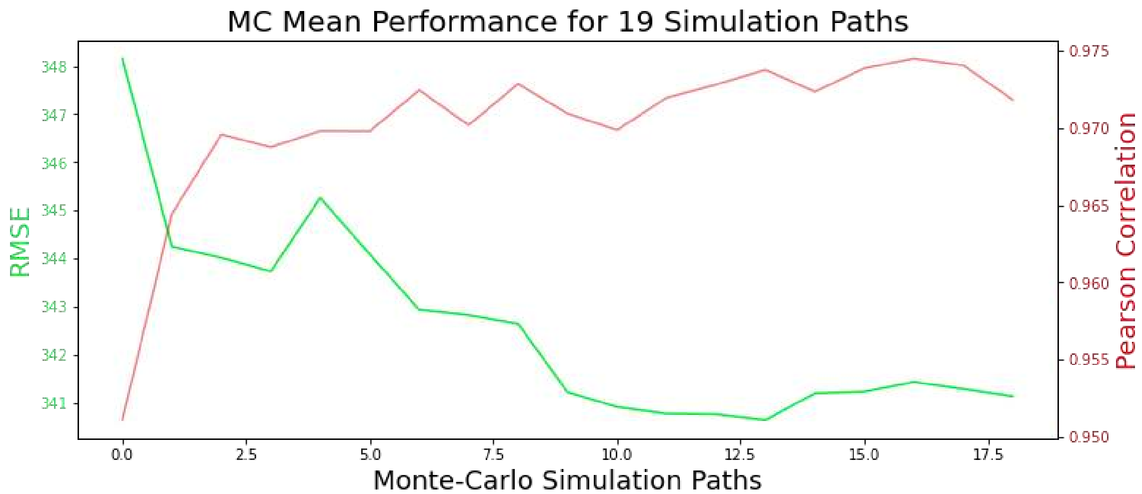

Figure 7.34. The Root Mean Square error and Pearson Correlation (R) for each MC mean path

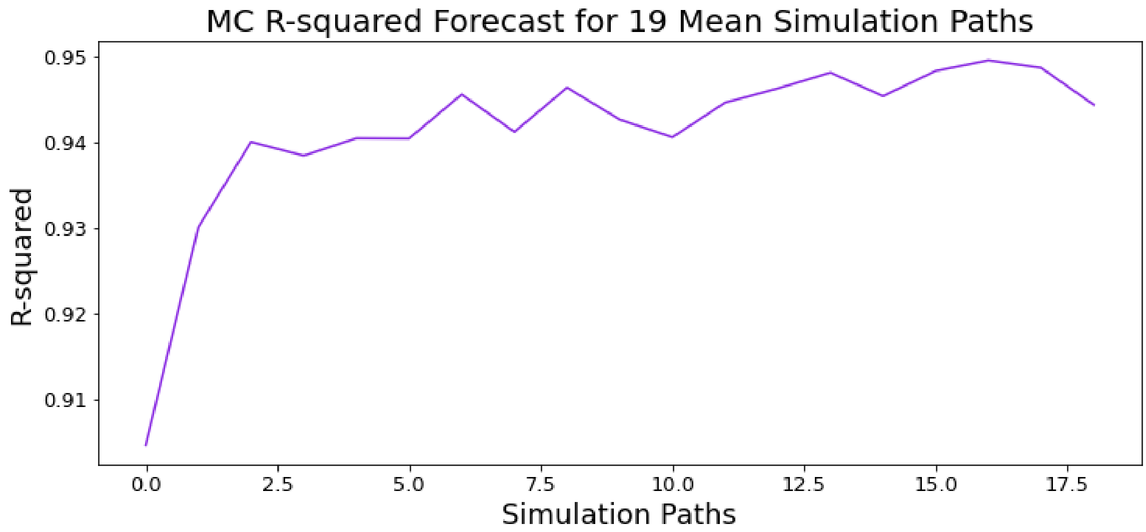

Figure 7.35. R-squared for the rolling mean MC simulation paths

The Monte-Carlo simulation slightly enhanced radon data as shown in **Figure 7.32**. For this purpose, root mean square error, Pearson correlation, and R-squared were considered as illustrated in **Figure 7.34** and **Figure 7.35**. In **Figure 7.33**, scatter plot for radon, multi-ANN model, and MC mean were obtained. RMSE (4.19) is decreased and R-squared value (0.9746) is increased. It means, the multi-ANN model can describe 97.46% of the Radon variance and the RMSE (4.19) gives an error of 4.19 $kBqm^{-3}$.

Table 7.1. Model performances for multi-linear regression model, multi-ANN and MC simulation.

Models	SSE	RMSE	R-squared
MLR	22601.92	11.33225	0.929466
Multi-ANN	3050.873	4.211607	0.974557
MCS	3024.038	4.193044	0.974612

7.4. Median and Temporal VTEC

In this section, vertical TEC variations from two stations caused by seismic activity were modelled for detecting pre-anomalies and post- anomalies per earthquake as illustrated in **Figure 7.36**. For the first time range of TEC data from Ankara station, Median TEC values, mTEC, upper and lower bounds were calculated. Anomalies for a moderate earthquake with M=5.9 during 2007-2010 were investigated. The ionospheric changes were analyzed including solar and geomagnetic activity data as displayed in **Figure 7.37**. Three adjacent earthquakes during 20 days were chosen.

The related past and recent studies were reviewed in the literature. The Dobrovolsky preparation zones for the earthquakes were computed. Earthquakes inside (De/R) <1 and outside (De/R) <2 preparation zone were selected. Some of the obtained results are as followings:

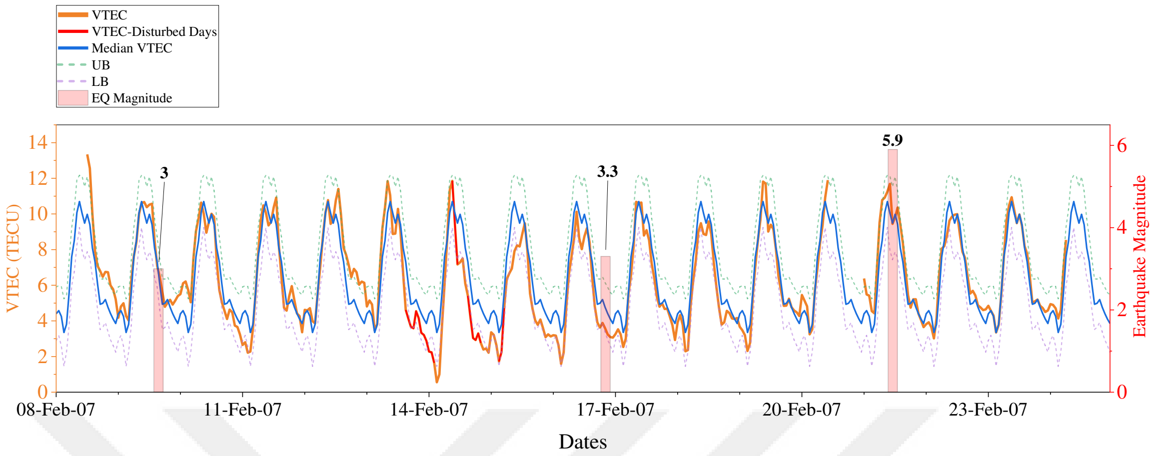

Figure 7.36. Diurnal Variation of TEC, Variation of TEC in disturbed days, Median TEC, lower and upper boundary (UB, LB), earthquake magnitude (Ankara station).

As a result of this study, the positive and negative anomalies were identified for three earthquakes in quiet conditions of geomagnetic and solar activity.

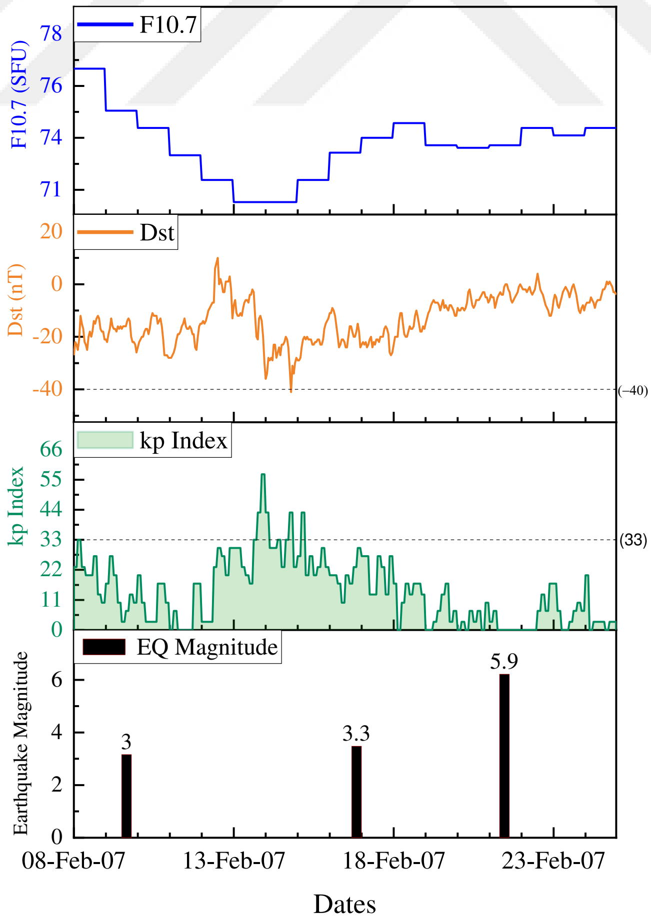

Figure 7.37. kp index, Dst, F10.7 and earthquake magnitude.

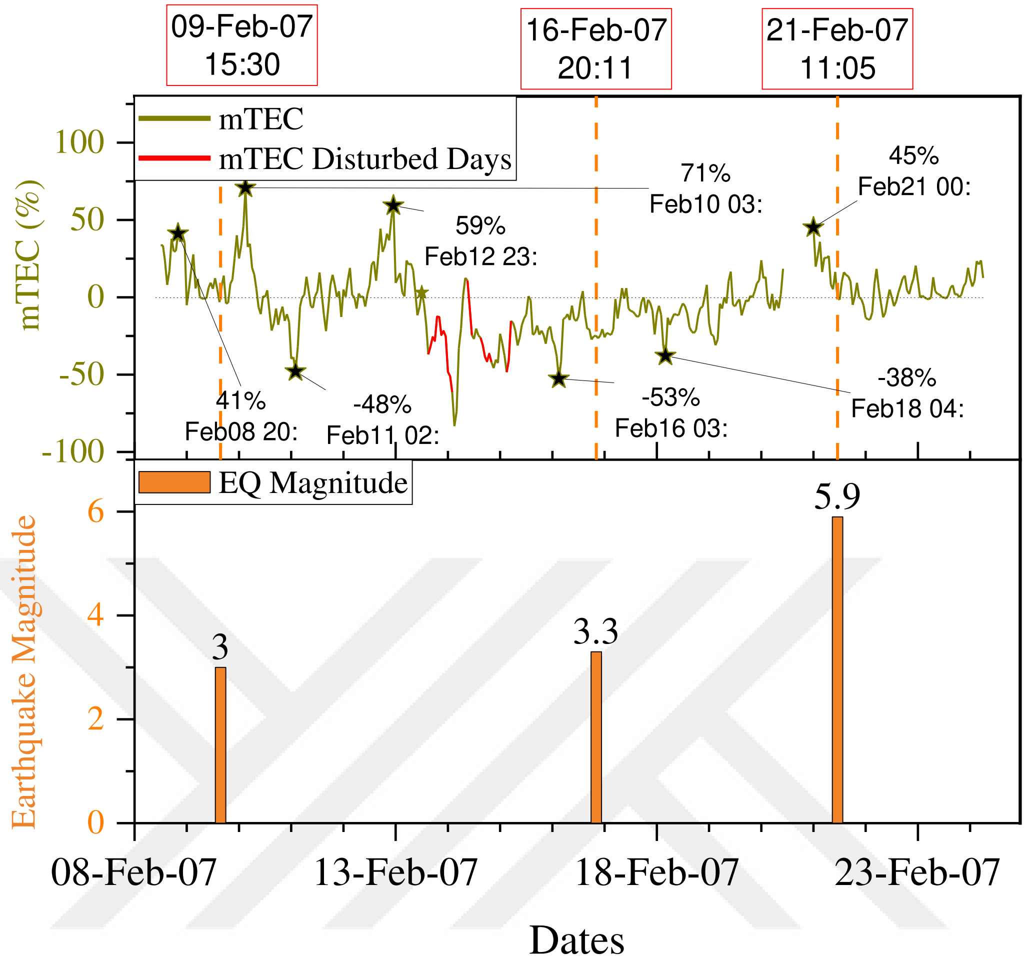

Figure 7.38. Temporal TEC and earthquake magnitude (Ankara station).

Figure 7.38 displays the fluctuations in the temporal-TEC when the EQ1, EQ2, and EQ3 earthquakes with a magnitude of M = 3, 3.3, and 5.9 occurred on February 9-21, 2007 respectively, denoted by the unit of TECU = 10^{16} el/m^2, and mTEC, denoted in %, exhibited numerous incidents of significant fluctuations prior and post to the earthquakes. Specifically, high positive peaks were detected with mTEC reaching ~45% on February 21, 2007 at 00:00 before EQ3 earthquake, and high peaks with 59% were observed on February 12, 2007 at 23:00 before EQ2 earthquake, also high peaks with 41% were detected on February 8, 2007 at 20:00 before EQ1 earthquake,71% on February 9, 2007 at 23:00 after EQ1 earthquake. Strong mTEC peaks observed after the daily-TEC peaks and before the TEC minima, indicating that the variances happened mostly between late afternoon to dawn.

For ensuring and confirming the model validity done in previous work, we obtained the TEC values from Trabzon station. Similarly, vertical TEC fluctuations produced by seismic activity were modelled for detecting pre-anomalies and post- anomalies per earthquake as illustrated in **Figure 7.40**. Median TEC values, upper and lower bounds were calculated. Anomalies for moderate earthquakes with M=5.9, 5.5 and 5.1 during 2007-2010 were investigated. The ionospheric changes were analyzed including solar and geomagnetic activity data as shown in **Figure 7.39**. Seven adjacent earthquakes during 40 days were chosen. The related past and recent studies were reviewed in the literature. The Dobrovolsky preparation zone for the earthquakes were computed. Earthquakes inside (De/R) <1 and outside (De/R) <2 preparation zone were selected. Some of the obtained results are as followings:

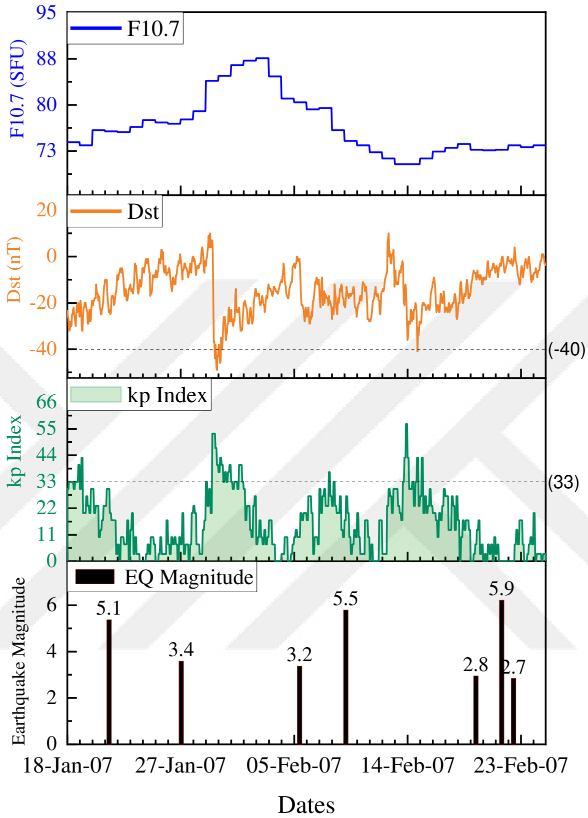

Figure 7.39. Kp index, Dst, F10.7 and earthquake magnitude.

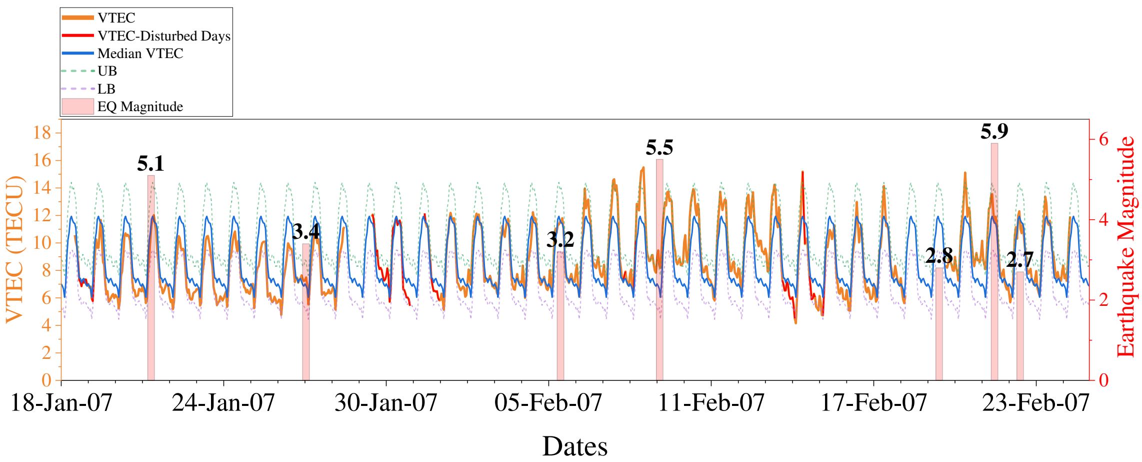

Figure 7.40. Diurnal Variation of TEC, Variation of TEC in disturbed days, Median TEC, lower and upper boundary (UB, LB), earthquake magnitude (Trabzon station).

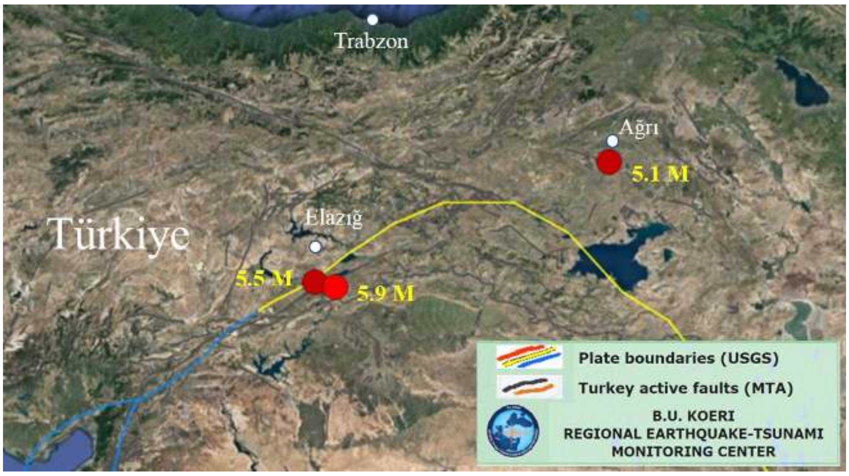

Figure 7.41. Locations of the Trabzon station and the epicenter of the main earthquakes.

Figure 7.41 displays the place of the earthquakes that happened during the time range of this study. On the other hand, **Figure 7.39** illustrates the geomagnetic storm and solar activity within the time range. Threshold level for disturbed condition is adjusted as shown in **Table 6.13**;

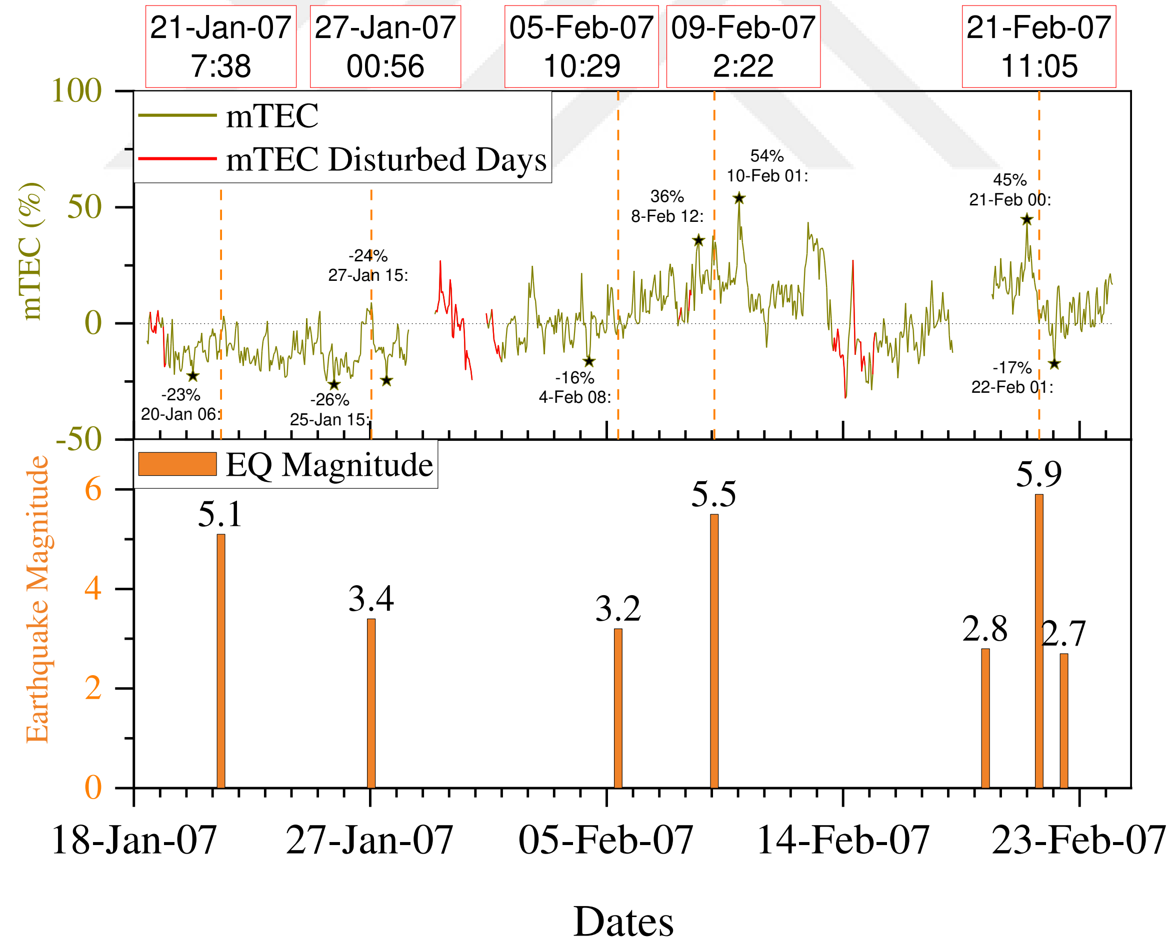

Figure 7.42. Temporal TEC and earthquake magnitude (Trabzon station).

Figure 7.42 displays the fluctuations in the temporal-TEC when the EQ1-EQ7 earthquakes with a magnitude of M = 5.1, 3.4, 3.2, 5.5, 2.8, 5.9, and 2.7 occurred between January 18, 2007 and February 24, 2007 respectively, denoted by TECU = 10^{16} el/m^2, and mTEC, denoted in %, exhibited numerous incidents of significant vagaries prior and pot to the earthquakes. Especially, high positive peaks were detected with mTEC reaching ~54% on February 10, 2007 at 01:00 after EQ4 earthquake, and high peaks with 45% were observed on February 21, 2007 at 00:00 before EQ6 earthquake, also high peaks with 36% were observed on February 8, 2007 at 12:00 before EQ4 earthquake. Strong mTEC peaks seen after the daily-TEC peaks and before the TEC minima, indicating that the anomalies happened mostly between late afternoon to dawn.

7.5. Spatial and Relative TEC

Another method to detect TEC anomalies due to earthquakes can be done by plotting a DTEC histogram. Also, more accurate results can be obtained by plotting the spatial characteristics of ionospheric disturbances over certain regions. In this research, we investigate the relative and spatial properties for moderate earthquakes. The obtained results for the two stations are shown as followings:

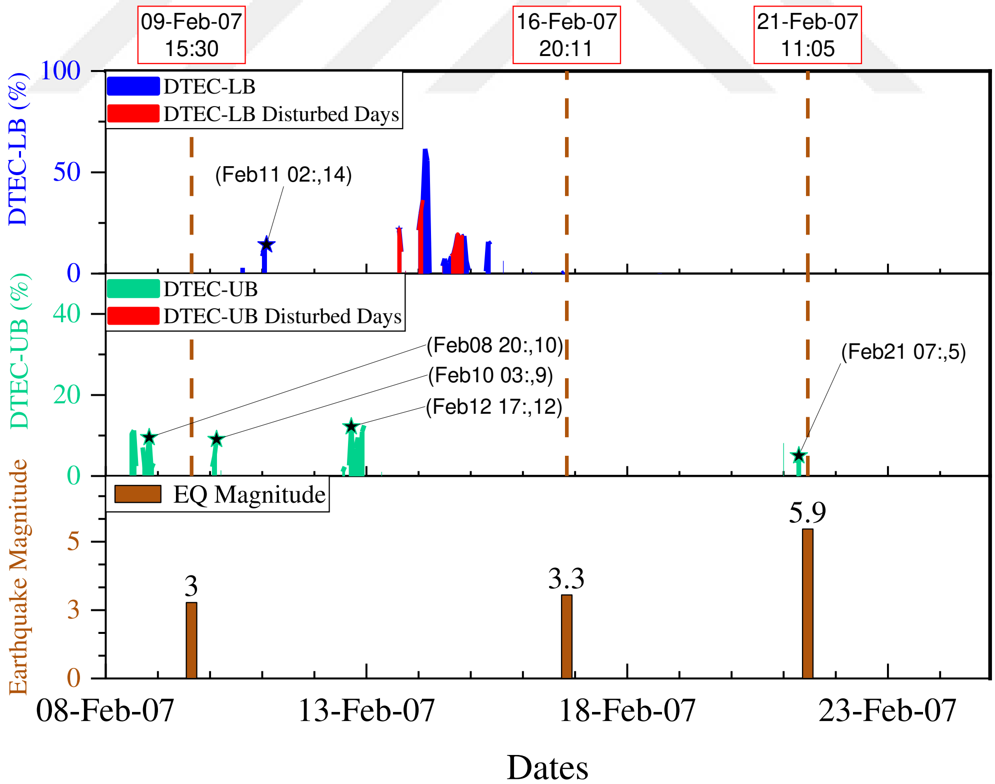

Figure 7.43. DTEC-LB, DTEC-UB, EQ magnitude; relative TEC deviation for lower and upper boundary, earthquake magnitude, respectively (Ankara station).

In **Figure 7.43**, the DTEC histogram depicts the changes in the TEC correlating to the anomalies in percentage. Because F10.7 values were at a low level (70–77 SFU) throughout the analysis period, the anomalies that happened throughout low geomagnetic activity periods are highlighted in red, and those related with geomagnetically disturbed days (Dst -40 nT or kp > 33), also the anomalies that occurred before and after earthquakes indicated by a star.

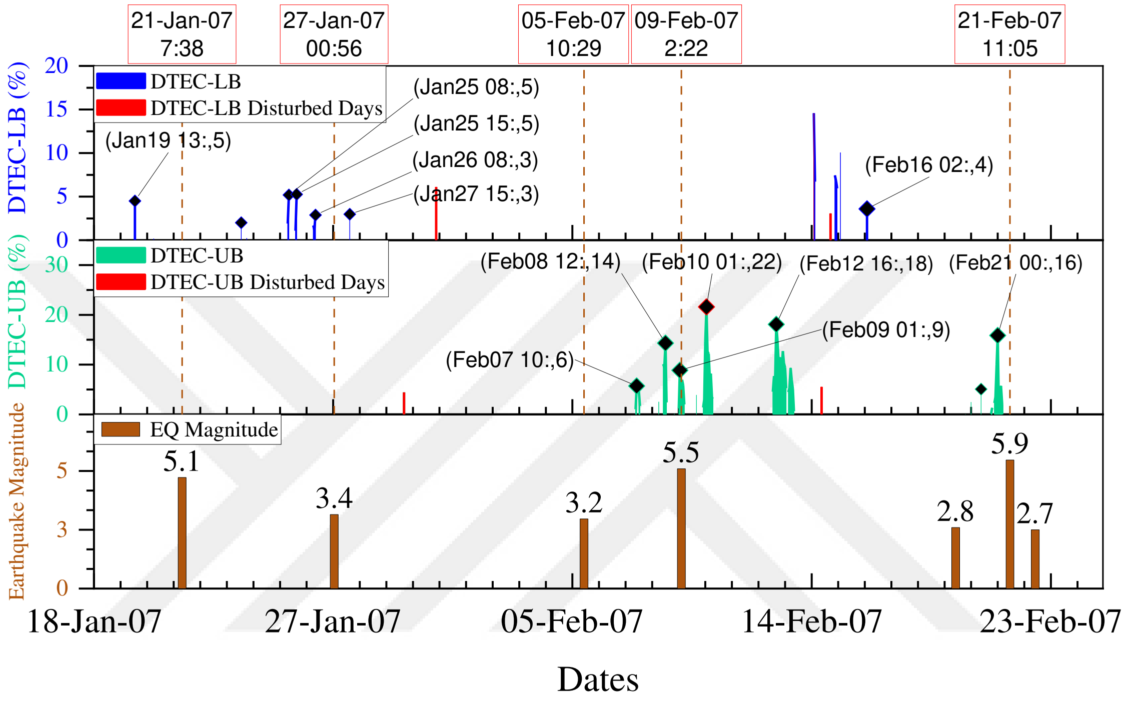

Figure 7.44. DTEC-LB, DTEC-UB, EQ magnitude; relative TEC deviation for lower and upper boundary, earthquake magnitude, respectively (Trabzon station).

In **Figure 7.44**, the DTEC histogram depicts the changes in the TEC relative to upper and lower boundaries correlating to the anomalies in percentage. Because F10.7 values were at a low level (62–88 SFU) throughout the analysis period, the anomalies that happened throughout low geomagnetic activity periods are highlighted in red, and those related with geomagnetically disturbed days (Dst < -40 nT or kp > 33), also the anomalies that occurred before and after earthquakes indicated by a rhombus. In particular, TEC anomalies (before, during, after EQ4) were observed reaching ~6% on February 07, 2007 at 10:00 and~14% on February 08, 2007 at 12:00 before EQ4 earthquake, ~9% on February 09, 2007 at 01:00 during EQ4 earthquake, ~22% on February 10, 2007 at 01:00 after EQ4 earthquake. Also, TEC anomalies were observed reaching ~16% on February 21, 2007 at 00:00 before the EQ6 earthquake.

Figure 7.45, illustrates spatial characteristics of ionospheric disturbances in relation to the EQ6 earthquake. The red dot denotes the epicenter of the earthquake. The maps obtained for the EQ6 earthquake clearly show TEC anomalies observed over the earthquake area on February 17, 2007 at 00:00 and February 19, 2007 at 00:00 before the EQ6 earthquake. Also, TEC anomalies observed on February 22, 2007 at 20:00 and February 23, 2007 at 22:00 after EQ6 earthquake.

Before Earthquake (5.9 M) After Earthquake (5.9 M)

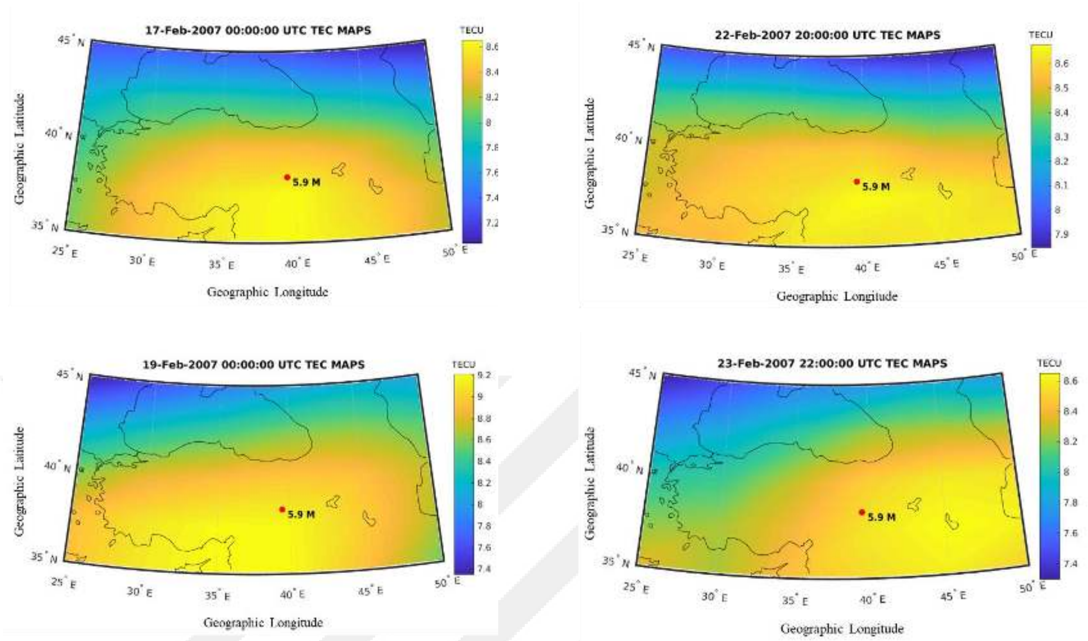

Figure 7.45. TEC maps (from IONOLAB) showing TEC anomalies prior and post to the earthquake (5.9 M). The red dot denotes the epicenter (Trabzon station).

7.6. Radon and TEC Cross-Correlation

Cross correlation is a technique for checking two-time series and obtaining how well they fit each other, as well as precisely where the best match occurs. Any periodicities can be exposed to the time series. In this study, the correlation between radon and TEC time series obtained, firstly the time series of both plotted as shown in **Figure 7.46**, then the scatter plot shown in **Figure 7.47**, finally the cross-correlation achieved as shown in **Figure 7.48**.

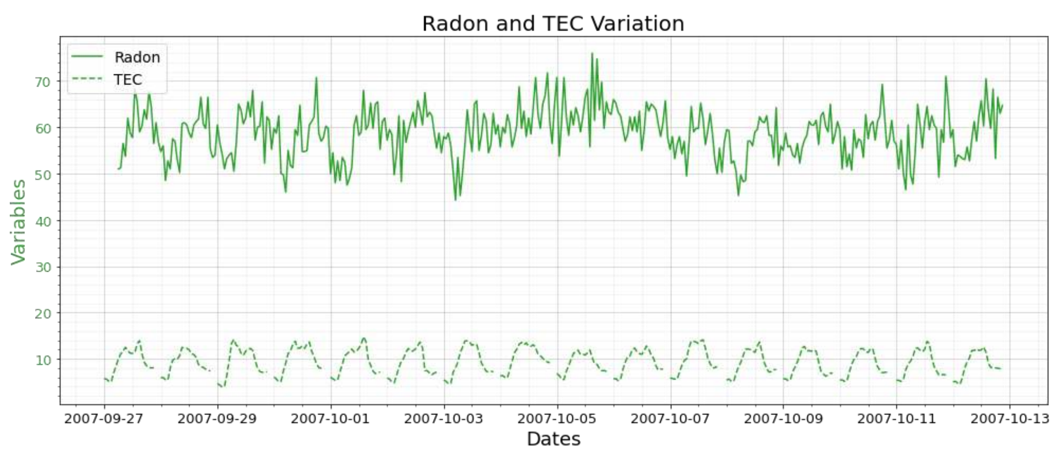

Figure 7.46. Time series of Radon and TEC data for analyzing their cross-correlation.

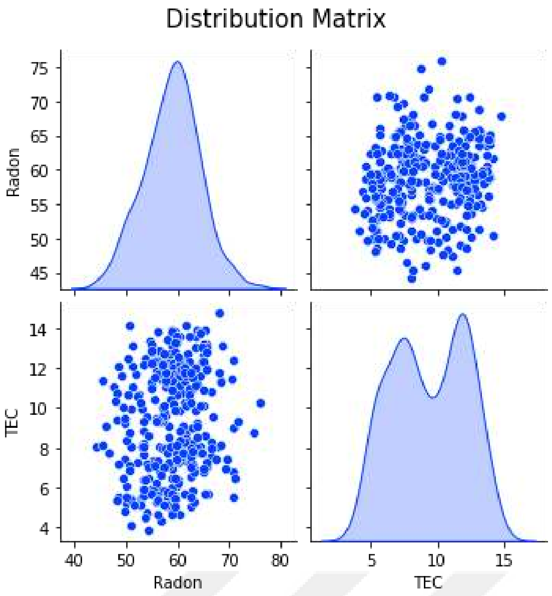

Figure 7.47. Scatter plot of Radon and TEC data.

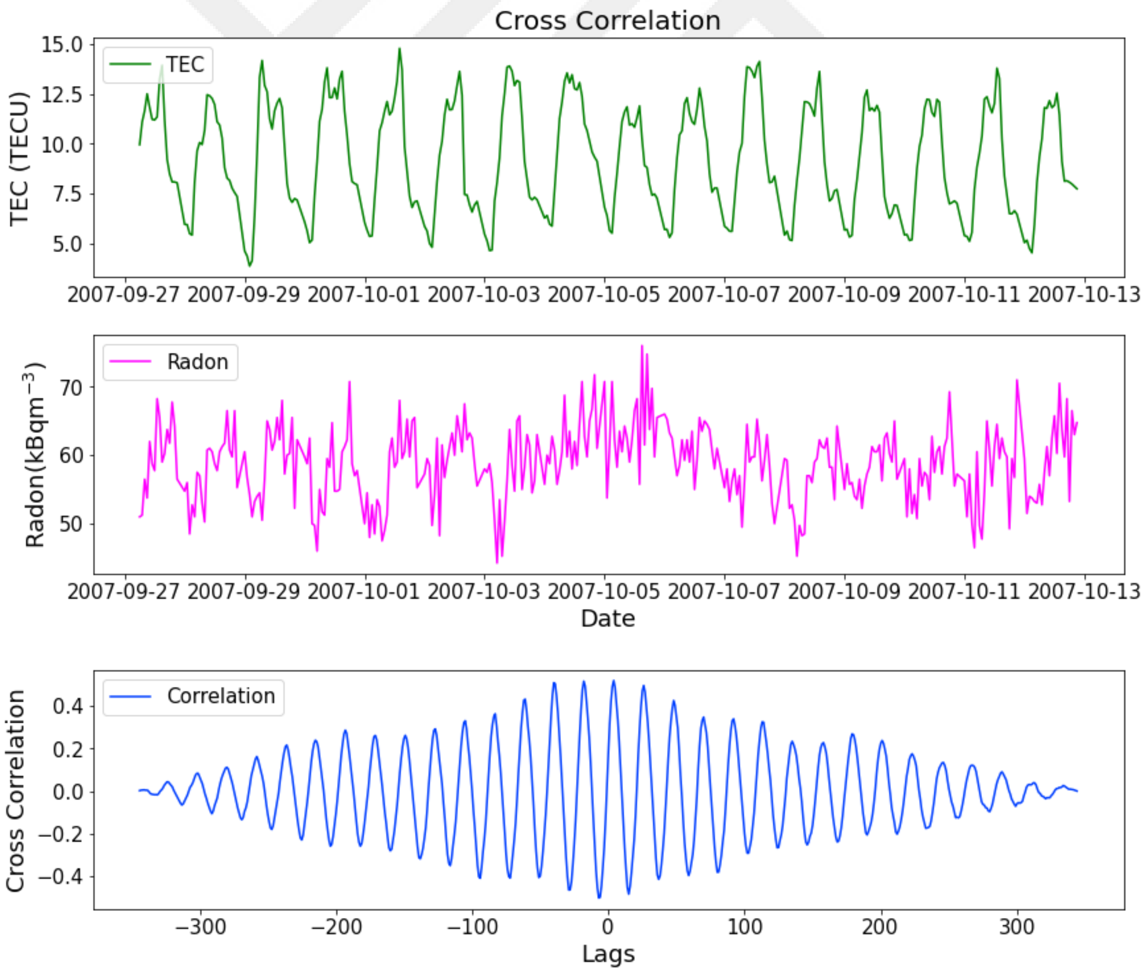

Figure 7.48. Cross-correlation of Radon and TEC (correlation coefficient versus lag). From the top panel TEC is plotted, the middle panel is radon time series, and the Correlogram at the bottom. The abscissae are in 60 minutes' intervals.

The lag exhibits how far the series are changed, while the sign explains which series have been moved. Because the series "hang out" at the endpoints and do not overlap, the number of possible matches decreases as the lag increases. The maximum correlation for total electron content is at lag 4 and is 0.52 which is the best match. The pattern is symmetrical with positive and negative lags. Oscillation in the correlation coefficients with lag shows periodicities in the original time series. When the two series are in phase, the coefficients of correlation will be large and positive. Whenever the two series are out of phase, they are large and negative.

8. CONCLUSIONS

The purpose of the present study was to model and forecast Rn-222 and TEC time series. The second target of this research was to study the seismo-ionospheric coupling, and evaluate the possibility of earthquake forecasting. This study established the combination of ARIMA model and Monte Carlo simulations (MCSs) together on Rn-222 and TEC time series which are efficient in stochastic evaluations to forecast radon concentration and TEC values. The results of ARIMA model and MCSs show a good fit with the test range, especially the forecasted TEC values in a good manner that represent the actual values.

On the other hand, multi-linear regression and multi-artificial neural network are presented that allows certain meteorological parameters to be combined to forecast Radon-222 data. The model forecasts radon behavior using meteorological parameters such as soil temperature, atmospheric temperature, and pressure. The multi-ANN model combines multi-regression and artificial neural network models. The model was applied to forecast radon behavior at the Reşadiye monitoring station, and the outcomes were satisfactory. Monte-Carlo forecasting was implemented using the multi-ANN model, and likely future Rn-222 variations were predicted. The model was then verified using real data that was not the same as that utilized in the study, with promising results. The model looks to be pretty capable of detecting anomalies. Additionally, the model may allow Seismo-Ionospheric models to include more meteorological parameters, allowing for a more detailed investigation of the findings. The model could be used to detect anomalies, especially in seismo-ionospheric studies where anomaly detection is critical.

As a result, the obtained Rn-222 concentrations and TEC values were analyzed to grasp seismo-ionospheric coupling phenomena utilizing TEC signatures for early earthquake warning in the study area. However, detecting TEC anomalies linked to earthquakes less than 6.0 M is a challenge due to the level of influence and dynamic complexity in the ionosphere. In this research, we analyzed the spatial and temporal properties in relation to a selection of M < 6.0 earthquakes in Türkiye during 2007 to identify possible seismo-ionospheric precursors. Anomalies of VTEC changes were established for a sequence of seven earthquakes by using a 40-day moving median approach of solar and geomatic quiet conditions. And then positive and negative TEC anomalies prior to the earthquakes were detected in quiet days, which occurred 1 to 9 days prior to the associated earthquake. Ionospheric anomalies caused by earthquakes vary from 16 to 54 % TECU over Trabzon station close to the epicenter (~300 km). The findings about spatial characteristics of ionospheric disturbances in relation to the earthquake with M = 5.9 reveal clear TEC anomalies over the earthquake area before and after the earthquake. Consequently, these studies have shown evidence that daily fluctuations in TEC anomalies might provide important precursors to earthquakes (M < 6.0) in the earthquake prediction of short-term for foreshocks and main shocks.

Finally, statistical relationship between Rn-222 and TEC using cross correlation analysis obtained. The maximum correlation for total electron content was 0.52. Radon-222's involvement in seismo-ionospheric coupling is still being investigated. This would be a fruitful area for further work.

RECOMMENDATIONS

The following are some implications for future research based on these findings. It is suggested that the association of these factors (All meteorological parameters) and more data ranges with fewer missing values is investigated in future studies. More Radon-222 data on the Radon-222 anomaly would enable us to improve the accuracy of this research. More research is needed to develop a deeper comprehension of the relationships between Radon-222, TEC data, and seismic activities.

REFERENCES

[1] A.J.S.C. Pereira, S.M. Barbosa, L.J.P.F. Neves, F. Aumento, Soil-gas radon monitoring in an active granite quarry from central Portugal, Nat. Hazards Earth Syst. Sci. 11 (2011) 1845–1849. https://doi.org/10.5194/nhess-11-1845-2011.

[2] N. Künze, M. Koroleva, C.D. Reuther, 222Rn activity in soil gas across selected fault segments in the Cantabrian Mountains, NW Spain, Radiat. Meas. 47 (2012) 389–399. https://doi.org/10.1016/J.RADMEAS.2012.02.013.

[3] WHO, WHO handbook on indoor radon, 2009. https://www.who.int/.

[4] C.Y. King, Radon emanation on San Andreas Fault, Nature. 271 (1978) 516–519. https://doi.org/10.1038/271516a0.

[5] T. Rikitake, Biosystem behaviour as an earthquake precursor, Tectonophysics. 51 (1978) 1–20. https://doi.org/10.1016/0040-1951(78)90048-3.

[6] T. Gold, S. Soter, Fluid ascent through the solid lithosphere and its relation to earthquakes, Pure Appl. Geophys. PAGEOPH. 122 (1984) 492–530. https://doi.org/10.1007/BF00874614.

[7] J.P. Toutain, J.C. Baubron, Gas geochemistry and seismotectonics: A review, Tectonophysics. 304 (1999) 1–27. https://doi.org/10.1016/S0040-1951(98)00295-9.

[8] O. Baykara, M. Doğru, M. Inceöz, E. Aksoy, Measurements of radon emanation from soil samples in triple-junction of North and East Anatolian active faults systems in Turkey, Radiat. Meas. 39 (2005) 209–212. https://doi.org/10.1016/j.radmeas.2004.04.011.

[9] V.I. Utkin, E. Mamyrov, M. V. Kan, S. V. Krivasheev, A.K. Yurkov, I.I. Kosyakin, A.N. Shishkanov, Radon monitoring in the Northern Tien Shan with application to the process of tectonic earthquake nucleation, Izv. Phys. Solid Earth. 42 (2006) 775–784. https://doi.org/10.1134/S1069351306090072.

[10] R.D. Cicerone, J.E. Ebel, J. Britton, A systematic compilation of earthquake precursors, Tectonophysics. 476 (2009) 371–396. https://doi.org/10.1016/j.tecto.2009.06.008.

[11] S.M. Barbosa, R. V. Donner, G. Steinitz, Radon applications in geosciences – Progress & perspectives, Eur. Phys. J. Spec. Top. 224 (2015) 597–603. https://doi.org/10.1140/epjst/e2015-02393-y.

[12] H. Woith, Radon earthquake precursor: A short review, Eur. Phys. J. Spec. Top. 224 (2015) 611–627.

[13] M. Baskaran, Radon: A Tracer for Geological, Geophysical and Geochemical Studies, Springer International Publishing, 2016. https://doi.org/10.1007/978-3-319-21329-3.

[14] Martin Paul, Lange Karina, Ishimori Yuu, Mayya YS, Phaneuf Marcelle, Fesenko Sergey, Measurement and calculation of radon releases from NORM residues: development of new IAEA document, Iaea, 2011.

[15] G.S. Gusain, G. Prasad, Y. Prasad, R.C. Ramola, Comparison of indoor radon level with radon exhalation rate from soil in Garhwal Himalaya, Radiat. Meas. 44 (2009) 1032–1035. https://doi.org/10.1016/j.radmeas.2009.10.033.

[16] UNSCEAR, Effects of Ionizing Radiation. Annex E - Sources-to-effects assessment for radon in homes and workplaces. UNSCEAR 2006 Report Vol. II, UNSCEAR 2006 Rep. Volume II (2006)

1–138. http://www.unscear.org/docs/reports/2006/09-81160_Report_Annex_E_2006_Web.pdf.

[17] S.D. Schery, D.H. Gaeddert, M.H. Wilkening, Factors Affecting Exhalation of Radon From a Gravelly Sandy Loam., J. Geophys. Res. 89 (1984) 7299–7309. https://doi.org/10.1029/JD089iD05p07299.

[18] W.W. Nazaroff, Radon transport from soil to air, Rev. Geophys. 30 (1992) 137–160. https://doi.org/10.1029/92RG00055.

[19] J.L. Pinault, J.C. Baubron, Signal processing of soil gas radon, atmospheric pressure, moisture, and soil temperature data: A new approach for radon concentration modeling, J. Geophys. Res. B Solid Earth. 101 (1996) 3157–3171. https://doi.org/10.1029/95jb03121.

[20] I. Barnet, J. Procházka, L. Skalský, Do the earth tides have an influence on short-term variations in radon concentration?, Radiat. Prot. Dosimetry. 69 (1997) 51–60. https://doi.org/10.1093/oxfordjournals.rpd.a031887.

[21] T.F. Yang, C.Y. Chou, C.H. Chen, L.L. Chyi, J.H. Jiang, Exhalation of radon and its carrier gases in SW Taiwan, Radiat. Meas. 36 (2003) 425–429.

[22] P. Richon, F. Perrier, E. Pili, J.C. Sabroux, Detectability and significance of 12 hr barometric tide in radon-222 signal, dripwater flow rate, air temperature and carbon dioxide concentration in an underground tunnel, Geophys. J. Int. 176 (2009) 683–694. https://doi.org/10.1111/j.1365-246X.2008.04000.x.

[23] G. Steinitz, O. Piatibratova, N. Gazit-Yaari, Influence of a component of solar irradiance on radon signals at 1 km depth, Gran Sasso, Italy, Proc. R. Soc. A Math. Phys. Eng. Sci. 469 (2013) 20130411. https://doi.org/10.1098/rspa.2013.0411.

[24] G. Steinitz, O. Piatibratova, P. Kotlarsky, Possible effect of solar tides on radon signals, J. Environ. Radioact. 102 (2011) 749–765. https://doi.org/10.1016/j.jenvrad.2011.04.002.

[25] C. Cigolini, P. Poggi, M. Ripepe, M. Laiolo, C. Ciamberlini, D. Delle Donne, G. Ulivieri, D. Coppola, G. Lacanna, E. Marchetti, D. Piscopo, R. Genco, Radon surveys and real-time monitoring at Stromboli volcano: Influence of soil temperature, atmospheric pressure and tidal forces on 222Rn degassing, J. Volcanol. Geotherm. Res. 184 (2009) 381–388. https://doi.org/10.1016/j.jvolgeores.2009.04.019.

[26] R.G.M. Crockett, C.J. Groves-Kirkby, A.R. Denman, P.S. Phillips, Significant annual and sub-annual cycles in indoor radon concentrations: Seasonal variation and correction, Geol. Soc. Spec. Publ. 451 (2018) 35–47. https://doi.org/10.1144/SP451.2.

[27] V. Udovičić, I. Aničin, D. Joković, A. Dragić, R. Banjanac, B. Grabež, N. Veselinović, Radon time-series analysis in the underground low-level laboratory in Belgrade, Serbia, Radiat. Prot. Dosimetry. 145 (2011) 155–158. https://doi.org/10.1093/rpd/ncr074.

[28] V. Udovičić, J. Filipović, A. Dragić, R. Banjanac, D. Joković, D. Maletić, B. Grabež, N. Veselinović, Daily and seasonal radon variability in the underground low-background laboratory in Belgrade, Serbia, Radiat. Prot. Dosimetry. 160 (2014) 62–64. https://doi.org/10.1093/rpd/ncu109.

[29] R. Yan, H. Woith, R. Wang, G. Wang, Decadal radon cycles in a hot spring, Sci Rep. 7 (2017) 12120. https://doi.org/10.1038/s41598-017-12441-0.

[30] A. Piersanti, V. Cannelli, G. Galli, The Pollino 2012 seismic sequence: Clues from continuous radon monitoring, Solid Earth. 7 (2016) 1303–1316. https://doi.org/10.5194/se-7-1303-2016.

[31] K.K. Liu, T.F. Yui, Y.H. Yeh, Y.B. Tsai, T.L. Teng, Variations of radon content in groundwaters and possible correlation with seismic activities in northern Taiwan, Pure Appl. Geophys. PAGEOPH. 122 (1984) 231–244. https://doi.org/10.1007/BF00874596.

[32] H. Friedmann, K. Aric, R. Gutdeutsch, C.Y. King, C. Altay, H. Sav, Radon measurements for earthquake prediction along the North Anatolian Fault Zone: a progress report, Tectonophysics. 152 (1988) 209–214. https://doi.org/10.1016/0040-1951(88)90047-9.

[33] M. Singh, M. Kumar, R.K. Jain, R.P. Chatrath, Radon in ground water related to seismic events, Radiat. Meas. 30 (1999) 465–469. https://doi.org/10.1016/S1350-4487(99)00049-9.

[34] H.S. Virk, V. Walia, A.K. Sharma, N. Kumar, R. Kumar, Correlation of radon anomalies with microseismic events in Kangra and Chamba valleys of N-W Himalaya, Geofis. Int. 39 (2000) 221–227. https://doi.org/10.22201/igeof.00167169p.2000.39.3.327.

[35] H.S. Virk, V. Walia, Helium/radon precursory signals of Chamoli Earthquake, India, Radiat. Meas. 34 (2001) 379–384. https://doi.org/10.1016/S1350-4487(01)00190-1.

[36] S. Pulinets, K. Boyarchuk, Ionospheric precursors of earthquakes, Springer Berlin Heidelberg, 2005. https://doi.org/10.1007/b137616.

[37] V. Walia, H.S. Virk, T.F. Yang, S. Mahajan, M. Walia, B.S. Bajwa, Earthquake prediction studies using radon as a precursor in NW Himalayas, India: a case study, TAO Terr. Atmos. Ocean. Sci. 16 (2005) 775.

[38] F. Külahcı, Ş. Çiçek, Time-series analysis of water and soil radon anomalies to identify micro–macro-earthquakes, Arab. J. Geosci. 8 (2015) 5239–5246. https://doi.org/10.1007/s12517-014-1513-9.

[39] H.P. Jaishi, S. Singh, R.P. Tiwari, R.C. Tiwari, Temporal variation of soil radon and thoron concentrations in Mizoram (India), associated with earthquakes, Nat. Hazards. 72 (2014) 443–454. https://doi.org/10.1007/s11069-013-1020-4.

[40] E. Stranden, A.K. Kolstad, B. Lind, The influence of moisture and temperature on radon exhalation, Radiat. Prot. Dosimetry. 7 (1984) 55–58. https://doi.org/10.1093/rpd/7.1-4.55.

[41] K. Wattananikorn, M. Kanaree, S. Wiboolsake, Soil gas radon as an earthquake precursor: some considerations on data improvement, Radiat. Meas. 29 (1998) 593–598.

[42] S. Singh, H.P. Jaishi, R.P. Tiwari, R.C. Tiwari, Variations of soil radon concentrations along chite fault in Aizawl district, Mizoram, India, Radiat. Prot. Dosimetry. 162 (2014) 73–77. https://doi.org/10.1093/rpd/ncu221.

[43] M. Janik, P. Bossew, Analysis of simultaneous time series of indoor, outdoor and soil air radon concentrations, meteorological and seismic data, Nukleonika. 61 (2016) 295–302. https://doi.org/10.1515/nuka-2016-0049.

[44] D. Xie, M. Liao, H. Wang, K.J. Kearfott, A study of diurnal and short-term variations of indoor radon concentrations at the University of Michigan, USA and their correlations with environmental factors, Indoor Built Environ. 26 (2016) 1051–1061. https://doi.org/10.1177/1420326x16660755.

[45] J.W. Kim, H.Y. Joo, R. Kim, J.H. Moon, Investigation of the relationship between earthquakes and indoor radon concentrations at a building in Gyeongju, Korea, Nucl. Eng. Technol. 50 (2018) 512–518. https://doi.org/10.1016/j.net.2017.12.010.

[46] J.Y. Liu, Y.I. Chen, S.A. Pulinets, Y.B. Tsai, Y.J. Chuo, Seismo-ionospheric signatures prior to M ≥

6.0 Taiwan earthquakes, Geophys. Res. Lett. 27 (2000) 3113–3116. https://doi.org/10.1029/2000GL011395.

[47] D. Ouzounov, S. Pulinets, K. Hattori, M. Kafatos, P. Taylor, Atmospheric Signals Associated with Major Earthquakes. A Multi-Sensor Approach., Electromagn. Phenom. Assoc. with Earthquakes. (2011) 1–23.

[48] M. Parrot, M. Li, DEMETER Results Related to Seismic Activity, Radio Sci. Bull. 355 (2015) 18–25. https://www.ursi.org/content/RSB/RSB_355_2015_12.pdf.

[49] S. Pulinets, D. Ouzounov, Lithosphere-Atmosphere-Ionosphere Coupling (LAIC) model - An unified concept for earthquake precursors validation, J. Asian Earth Sci. 41 (2011) 371–382. https://doi.org/10.1016/j.jseaes.2010.03.005.

[50] C.J. Hegarty, J.M. Foley, S.K. Kalyanaraman, Global positioning system, Springer Wien, 2017. https://doi.org/10.1201/b17545.

[51] S.A. Pulinets, A.N. Kotsarenko, L. Ciraolo, I.A. Pulinets, Special case of ionospheric day-to-day variability associated with earthquake preparation, Adv. Sp. Res. 39 (2007) 970–977. https://doi.org/10.1016/j.asr.2006.04.032.

[52] J.Y. Liu, Y.I. Chen, C.H. Chen, C.Y. Liu, C.Y. Chen, M. Nishihashi, J.Z. Li, Y.Q. Xia, K.I. Oyama, K. Hattori, C.H. Lin, Seismoionospheric GPS total electron content anomalies observed. before the 12 May 2008 Mw7.9 Wenchuan earthquake, J. Geophys. Res. Sp. Phys. 114 (2009). https://doi.org/10.1029/2008JA013698.

[53] S. Kalita, M. Devi, A. K. Barbara, P. H. Talukdar, Soft Computing Technique for Recognition of Earthquake Precursor from Low Latitude Total Electron Content (TEC) Profiles, Int. J. Comput. Appl. 44 (2012) 11–14. https://doi.org/10.5120/6354-8775.

[54] K. Hattori, S. Hirooka, M. Kunimitsu, T. Ichikawa, P. Han, Ionospheric anomaly as an earthquake precursor: Case and statistical studies during 1998–2012 around Japan, in: 2014 XXXIth URSI Gen. Assem. Sci. Symp. (URSI GASS), IEEE, 2014: pp. 1–1. https://doi.org/10.1109/ursigass.2014.6929866.

[55] D. Pundhir, Study of Ionospheric precursors related to an earthquake (M=7.8) of 16 April, 2013 using GPS-TEC measurements: Case study, J. Geogr. Nat. Disasters. 05 (2015) 1–3. https://doi.org/10.4172/2167-0587.1000137.

[56] C. Oikonomou, H. Haralambous, B. Muslim, Investigation of ionospheric TEC precursors related to the M7.8 Nepal and M8.3 Chile earthquakes in 2015 based on spectral and statistical analysis, Nat. Hazards. 83 (2016) 97–116. https://doi.org/10.1007/s11069-016-2409-7.

[57] G. Sharma, P.K. Champati ray, S. Mohanty, S. Kannaujiya, Ionospheric TEC modelling for earthquakes precursors from GNSS data, Quat. Int. 462 (2017) 65–74. https://doi.org/10.1016/j.quaint.2017.05.007.

[58] M. Akhoondzadeh, A. De Santis, D. Marchetti, A. Piscini, G. Cianchini, Multi precursors analysis associated with the powerful Ecuador (M W = 7.8) earthquake of 16 April 2016 using Swarm satellites data in conjunction with other multi-platform satellite and ground data, Adv. Sp. Res. 61 (2018) 248–263. https://doi.org/10.1016/j.asr.2017.07.014.

[59] W. Li, J. Yue, J. Guo, Y. Yang, B. Zou, Y. Shen, K. Zhang, Statistical seismo-ionospheric precursors

of M7.0+ earthquakes in Circum-Pacific seismic belt by GPS TEC measurements, Adv. Sp. Res. 61 (2018) 1206–1219. https://doi.org/10.1016/j.asr.2017.12.013.

[60] L. Perrone, A. De Santis, C. Abbattista, L. Alfonsi, L. Amoruso, M. Carbone, C. Cesaroni, G. Cianchini, G. De Franceschi, A. De Santis, R. Di Giovambattista, D. Marchetti, F.J. Pavòn-Carrasco, A. Piscini, L. Spogli, F. Santoro, Ionospheric anomalies detected by ionosonde and possibly related to crustal earthquakes in Greece, in: Ann. Geophys., 2018: pp. 361–371. https://doi.org/10.5194/angeo-36-361-2018.

[61] F. Huang, M. Li, Y. Ma, Y. Han, L. Tian, W. Yan, X. Li, Studies on earthquake precursors in China: A review for recent 50 years, Geod. Geodyn. 8 (2017) 1–12. https://doi.org/10.1016/j.geog.2016.12.002.

[62] C.J. Schrijver, G.L. Siscoe, Heliophysics: Space storms and radiation: Causes and effects, Cambridge University Press, 2010. https://doi.org/10.1017/CBO9781139194532.

[63] P. Wang, Solar Physics Research Trends, Sol. Phys. Res. Trends, Ed. by Pingzhi Wang. ISBN 1-60021-987-x. Nov. Publ. (2008).

[64] S.A. Pulinets, P. Biagi, V. Tramutoli, A.D. Legen’ka, V.K. Depuev, Irpinia earthquake 23 November 1980 - Lesson from nature reviled by joint data analysis, Ann. Geophys. 50 (2007) 61–78.

[65] S.A. Pulinets, T.B. Gaivoronska, A. Leyva Contreras, L. Ciraolo, Correlation analysis technique revealing ionospheric precursors of earthquakes, Nat. Hazards Earth Syst. Sci. 4 (2004) 697–702. https://doi.org/10.5194/nhess-4-697-2004.

[66] D. Marchetti, A. De Santis, X. Shen, S.A. Campuzano, L. Perrone, A. Piscini, R. Di Giovambattista, S. Jin, A. Ippolito, G. Cianchini, C. Cesaroni, D. Sabbagh, L. Spogli, Z. Zhima, J. Huang, Possible Lithosphere-Atmosphere-Ionosphere Coupling effects prior to the 2018 Mw = 7.5 Indonesia earthquake from seismic, atmospheric and ionospheric data, J. Asian Earth Sci. 188 (2020). https://doi.org/10.1016/j.jseaes.2019.104097.

[67] J.-Y.G. Liu, F.Y. Chang, D. Ouzounov, S.A. Pulinets, V. Tramutoli, K. Hattori, X. Shen, D.-P. Liu, R. Yan, Seismo-ionospheric Precursors of the 5 August 2018 M6.9 Loloan Earthquake Observed by CSES and Ground-based GNSS Receivers, (2019). https://agu-do03.confex.com/agu/fm19/meetingapp.cgi/Paper/571009 (accessed August 5, 2020).

[68] M.A. Titova, V.I. Zakharov, S.A. Pulinets, Determination of ionospheric disturbances over seismic sources during large earthquakes of 2010 by radiophysical methods under conditions of quiet geomagnetic field, in: 2019 Russ. Open Conf. Radio Wave Propagation, RWP 2019 - Proc., Institute of Electrical and Electronics Engineers Inc., 2019: pp. 160–162. https://doi.org/10.1109/RWP.2019.8810168.

[69] F. Huang, M. Li, Y. Ma, Y. Han, L. Tian, W. Yan, X. Li, Studies on earthquake precursors in China: A review for recent 50 years, Geod. Geodyn. 8 (2017) 1–12. https://doi.org/10.1016/j.geog.2016.12.002.

[70] G.. Box, G.E. and Jenkins, Time series analysis. Forecasting and control. in Holden-Day Series in Time Series Analysis, Revised ed, Holden-Day, 1976.

[71] G.P. Zhang, Time series forecasting using a hybrid ARIMA and neural network model, Neurocomputing. 50 (2003) 159–175.

[72] K.W. Hipel, A.I. McLeod, Time series modelling of water resources and environmental systems, Elsevier, 1994. https://doi.org/10.1016/0022-1694(95)90010-1.

[73] M.J. Fryer, R.Y. Rubinstein, Simulation and the Monte Carlo Method., John Wiley & Sons, 1983. https://doi.org/10.2307/2981504.

[74] F. Külahcı, S. Aközcan, O. Günay, Monte Carlo simulations and forecasting of Radium-226, Thorium-232, and Potassium-40 radioactivity concentrations, J. Radioanal. Nucl. Chem. 324 (2020) 55–70. https://doi.org/10.1007/s10967-020-07059-y.

[75] A.D.K. Tareen, K.M. Asim, K.J. Kearfott, M. Rafique, M.S.A. Nadeem, T. Iqbal, S.U. Rahman, Automated anomalous behaviour detection in soil radon gas prior to earthquakes using computational intelligence techniques, J. Environ. Radioact. 203 (2019) 48–54. https://doi.org/10.1016/j.jenvrad.2019.03.003.

[76] S.A. Pulinets, V.A. Alekseev, A.D. Legen'ka, V. V. Khegai, Radon and metallic aerosols emanation before strong earthquakes and their role in atmosphere and ionosphere modification, Adv. Sp. Res. 20 (1997) 2173–2176. https://doi.org/10.1016/S0273-1177(97)00666-2.

[77] J. Vaupotič, A. Riggio, M. Santulin, B. Zmazek, I. Kobal, A radon anomaly in soil gas at Cazzaso, NE Italy, as a precursor of an ML = 5.1 earthquake, Nukleonika. 55 (2010) 507–511.

[78] B. Zmazek, M. Živčić, L. Todorovski, S. Džeroski, J. Vaupotič, I. Kobal, Radon in soil gas: how to identify anomalies caused by earthquakes, Appl. Geochemistry. 20 (2005) 1106–1119.

[79] J.W. Washington, A.W. Rose, Regional and temporal relations of radon in soil gas to soil temperature and moisture, Geophys. Res. Lett. 17 (1990) 829–832. https://doi.org/10.1029/GL017i006p00829.

[80] S. Inan, T. Akgül, C. Seyis, R. Saatçilar, S. Baykut, S. Ergintav, M. Baş, Geochemical monitoring in the Marmara region (NW Turkey): A search for precursors of seismic activity, J. Geophys. Res. Solid Earth. 113 (2008) 1–15. https://doi.org/10.1029/2007JB005206.

[81] S. Inan, K. Ertekin, C. Seyis, Ş. Şimşek, F. Kulak, A. Dikbaş, O. Tan, S. Ergintav, R. Çakmak, A. Yörük, M. Çergel, H. Yakan, H. Karakuş, R. Saatçilar, Z. Akçiğ, Y. Iravul, B. Tüzel, Multi-disciplinary earthquake researches in Western Turkey: Hints to select sites to study geochemical transients associated to seismicity, Acta Geophys. 58 (2010) 767–813. https://doi.org/10.2478/s11600-010-0016-7.

[82] D. Iskandar, H. Yamazawa, T. Iida, Quantification of the dependency of radon emanation power on soil temperature, Appl. Radiat. Isot. 60 (2004) 971–973. https://doi.org/10.1016/j.apradiso.2004.02.003.

[83] R.C. Ramola, M. Singh, A.S. Sandhu, S. Singh, H.S. Virk, The use of radon as an earthquake precursor, Nucl. Geophys. 4 (1990) 275–287.

[84] J. Planinić, B. Vuković, V. Radolić, Radon time variations and deterministic chaos, J. Environ. Radioact. 75 (2004) 35–45. https://doi.org/10.1016/j.jenvrad.2003.10.007.

[85] S.M. Barbosa, G. Steinitz, O. Piatibratova, M.E. Silva, P. Lago, Radon variability at the Elat granite, Israel: Heteroscedasticity and nonlinearity, Geophys. Res. Lett. 34 (2007). https://doi.org/10.1029/2007GL030065.

[86] F. Külahcı, Z. Şen, On the Correction of Spatial and Statistical Uncertainties in Systematic Measurements of 222 Rn for Earthquake Prediction, Surv. Geophys. 35 (2014) 449–478.

https://doi.org/10.1007/s10712-013-9273-8.

[87] M. Kamişlioğlu, F. Külahci, Chaotic Behavior of Soil Radon Gas and Applications, Acta Geophys. 64 (2016) 1563–1592. https://doi.org/10.1515/acgeo-2016-0077.

[88] S. Baykut, T. Akgül, S. Inan, C. Seyis, Observation and removal of daily quasi-periodic components in soil radon data, Radiat. Meas. 45 (2010) 872–879. https://doi.org/10.1016/j.radmeas.2010.04.002.

[89] S. Baykut, T. Akgul, S. Inan, Seismic activity-related anomaly detection in Soil Radon Emanation, in: Eur. Signal Process. Conf., IEEE, 2011: pp. 908–912.

[90] V.M. Choubey, N. Kumar, B.R. Arora, Precursory signatures in the radon and geohydrological borehole data for M4.9 Kharsali earthquake of Garhwal Himalaya, Sci. Total Environ. 407 (2009) 5877–5883. https://doi.org/10.1016/j.scitotenv.2009.08.010.

[91] V.M. Choubey, P.K. Mukherjee, R.C. Ramola, Radon variation in Spring water before and after Chamoli earthquake, Garhwal Himalaya , India, in: Elev. Int. Congr. Int. Radiat. Prot. Assoc., 2004: pp. 1–7.

[92] S.C. Cohen, Postseismic viscoelastic surface deformation and stress. 1. Theoretical considerations, displacement, and strain calculations., J. Geophys. Res. 85 (1980) 3131–3150. https://doi.org/10.1029/JB085iB06p03131.

[93] I.P. Dobrovolsky, S.I. Zubkov, V.I. Miachkin, Estimation of the size of earthquake preparation zones, Pure Appl. Geophys. PAGEOPH. 117 (1979) 1025–1044. https://doi.org/10.1007/BF00876083.

[94] J. Hartmann, J.K. Levy, Hydrogeological and gasgeochemical earthquake precursors - A review for application, Nat. Hazards. 34 (2005) 279–304. https://doi.org/10.1007/s11069-004-2072-2.

[95] C.Y. King, Episodic radon changes in subsurface soil gas along active faults and possible relation to earthquakes., J. Geophys. Res. 85 (1980) 3065–3078. https://doi.org/10.1029/JB085iB06p03065.

[96] F. Külahci, M. Inceöz, M. Doğru, E. Aksoy, O. Baykara, Artificial neural network model for earthquake prediction with radon monitoring, Appl. Radiat. Isot. 67 (2009) 212–219. https://doi.org/10.1016/j.apradiso.2008.08.003.

[97] R.C. Ramola, Y. Prasad, G. Prasad, S. Kumar, V.M. Choubey, Soil-gas radon as seismotectonic indicator in Garhwal Himalaya, Appl. Radiat. Isot. 66 (2008) 1523–1530. https://doi.org/10.1016/j.apradiso.2008.04.006.

[98] R.C. Ramola, S. Singh, H.S. Virk, A model for the correlation between radon anomalies and magnitude of earthquakes, Int. J. Radiat. Appl. Instrumentation. Part. 15 (1988) 689–692. https://doi.org/10.1016/1359-0189(88)90229-4.

[99] S. Singh, H.P. Jaishi, R.P. Tiwari, R.C. Tiwari, Time Series Analysis of Soil Radon Data Using Multiple Linear Regression and Artificial Neural Network in Seismic Precursory Studies, Pure Appl. Geophys. 174 (2017) 2793–2802. https://doi.org/10.1007/s00024-017-1556-4.

[100] K.M. Asim, F. Javed, S. Hainzl, T. Iqbal, Fault parameters-based earthquake magnitude estimation using artificial neural networks, Seismol. Res. Lett. 90 (2019) 1544–1551. https://doi.org/10.1785/0220190051.

[101] R.L. Fleischer, Dislocation model for radon response to distant earthquakes, Geophys. Res. Lett. 8 (1981) 477–480. https://doi.org/10.1029/GL008i005p00477.

[102] D.R. Montgomery, M. Manga, Streamflow and water well responses to earthquakes, Science (80-.).

300 (2003) 2047–2049. https://doi.org/10.1126/science.1082980.

[103] M. Kiyoo, 4. Migration of Seismic Activity, Migration. 46 (1968) 53–74.

[104] N.N. Ambraseys, Some characteristic features of the Anatolian fault zone, Tectonophysics. 9 (1970) 143–165. https://doi.org/10.1016/0040-1951(70)90014-4.

[105] M.N. Toksöz, A.F. Shakal, A.J. Michael, Space-Time Migration of Earthquakes Along the North Anatolian Fault Zone and Seismic Gaps, Earthq. Predict. Seism. Patterns. 117 (1979) 1258–1270. https://doi.org/10.1007/978-3-0348-6430-5_9.

[106] G. Purcaru, H. Berckhemer, Regularity patterns and zones of seismic potential for future large earthquakes in the mediterranean region, Tectonophysics. 85 (1982) 1–30. https://doi.org/10.1016/0040-1951(82)90073-7.

[107] A.A. Barka, K. Kadinsky-Cade, Strike-slip fault geometry in Turkey and its influence on earthquake activity, Tectonics. 7 (1988) 663–684. https://doi.org/10.1029/TC007i003p00663.

[108] R.S. Stein, A.A. Barka, J.H. Dieterich, Progressive failure on the North Anatolian fault since 1939 by earthquake stress triggering, Geophys. J. Int. 128 (1997) 594–604. https://doi.org/10.1111/j.1365-246X.1997.tb05321.x.

[109] A. Barka, H.S. Akyüz, E. Altunel, G. Sunal, Z. Çakir, A. Dikbas, B. Yerli, R. Armijo, B. Meyer, J.B. De Chabalier, T. Rockwell, J.R. Dolan, R. Hartleb, T. Dawson, S. Christofferson, A. Tucker, T. Fumal, R. Langridge, H. Stenner, W. Lettis, J. Bachhuber, W. Page, The surface rupture and slip distribution of the 17 August 1999 İzmit earthquake (M 7.4), North Anatolian fault, Bull. Seismol. Soc. Am. 92 (2002) 43–60. https://doi.org/10.1785/0120000841.

[110] H.S. Akyüz, R. Hartleb, A. Barka, E. Altunel, G. Sunal, B. Meyer, R. Armijo, Surface rupture and slip distribution of the 12 November 1999 Düzce earthquake (M 7.1), North Anatolian fault, Bolu, Turkey, Bull. Seismol. Soc. Am. 92 (2002) 61–66. https://doi.org/10.1785/0120000840.

[111] F. Lorenzo-Martín, F. Roth, R. Wang, Elastic and inelastic triggering of earthquakes in the North Anatolian Fault zone, Tectonophysics. 424 (2006) 271–289. https://doi.org/10.1016/j.tecto.2006.03.046.

[112] M. Inceöz, O. Baykara, E. Aksoy, M. Doğru, Measurements of soil gas radon in active fault systems: A case study along the North and East anatolian fault systems in Turkey, Radiat. Meas. 41 (2006) 349–353. https://doi.org/10.1016/j.radmeas.2005.07.024.

[113] M. Bohnhoff, P. Martínez-Garzón, F. Bulut, E. Stierle, Y. Ben-Zion, Maximum earthquake magnitudes along different sections of the North Anatolian fault zone, Tectonophysics. 674 (2016) 147–165. https://doi.org/10.1016/j.tecto.2016.02.028.

[114] M. Bohnhoff, M. Ickrath, G. Dresen, Seismicity distribution in conjunction with spatiotemporal variations of coseismic slip and postseismic creep along the combined 1999 Izmit-Düzce rupture, Tectonophysics. 686 (2016) 132–145. https://doi.org/10.1016/j.tecto.2016.07.029.

[115] N. Uchida, D. Kalafat, A. Pinar, Y. Yamamoto, Repeating earthquakes and interplate coupling along the western part of the North Anatolian Fault, Tectonophysics. 769 (2019) 228185. https://doi.org/10.1016/j.tecto.2019.228185.

[116] E. Bozkurt, Neotectonics of turkey–a synthesis, Geodin. Acta. 14 (2001) 3–30. https://doi.org/10.1080/09853111.2001.11432432.

[117] D. McKenzie, Active Tectonics of the Mediterranean Region, Geophys. J. R. Astron. Soc. 30 (1972) 109–185. https://doi.org/10.1111/j.1365-246X.1972.tb02351.x.

[118] A.M.C. Sengor, N. Gorur, F. Saroglu, Strike-slip faulting and related basin formation in zones of tectonic escape: Turkey as a case study., Strike-Slip Deform. Basin Form. Sediment. (1985) 227–264. https://doi.org/10.2110/pec.85.37.0227.

[119] B.A. Bolt, Seismic air waves from the great 1964 Alaskan earthquake, Nature. 202 (1964) 1095–1096. https://doi.org/10.1038/2021095a0.

[120] W.L. Donn, E.S. Posmentier, Ground-coupled air waves from the Great Alaskan Earthquake, J. Geophys. Res. 69 (1964) 5357–5361. https://doi.org/10.1029/jz069i024p05357.

[121] G.W. Moore, Magnetic disturbances preceding the 1964 Alaska earthquake, Nature. 203 (1964) 508–509. https://doi.org/10.1038/203508b0.

[122] K. Davies, D.M. Baker, Ionospheric effects observed around the time of the Alaskan earthquake of March 28, 1964, J. Geophys. Res. 70 (1965) 2251–2253. https://doi.org/10.1029/jz070i009p02251.

[123] R.S. Leonard, R.A. Barnes, Observation of ionospheric disturbances following the Alaska earthquake, J. Geophys. Res. 70 (1965) 1250–1253. https://doi.org/10.1029/jz070i005p01250.

[124] R. V. Row, Evidence of long-period acoustic-gravity waves launched into the F region by the Alaskan earthquake of March 28, 1964 , J. Geophys. Res. 71 (1966) 343–345. https://doi.org/10.1029/jz071i001p00343.

[125] P.C. Yuen, P.F. Weaver, R.K. Suzuki, A.S. Furumoto, Continuous, traveling coupling between seismic waves and the ionosphere evident in May 1968 Japan earthquake data, J. Geophys. Res. 74 (1969) 2256–2264.

[126] M. Mendillo, H. Rishbeth, R.G. Roble, J. Wroten, Modelling F2-layer seasonal trends and day-to-day variability driven by coupling with the lower atmosphere, J. Atmos. Solar-Terrestrial Phys. 64 (2002) 1911–1931. https://doi.org/10.1016/S1364-6826(02)00193-1.

[127] E.L. Afraimovich, E.I. Astafyeva, A. V. Oinats, Y. V. Yasukevich, I. V. Zhivetiev, Global electron content: A new conception to track solar activity, in: Ann. Geophys., 2008: pp. 335–344. https://doi.org/10.5194/angeo-26-335-2008.

[128] K. Hocke, Oscillations of global mean TEC, J. Geophys. Res. Sp. Phys. 113 (2008). https://doi.org/10.1029/2007JA012798.

[129] T.B. Yanovskaya, Basics of Seismology, St. Petersbg. State Univ. (2008).

[130] USGS, What is a fault and what are the different types?, Usgs. (2016) 1–6. https://www2.usgs.gov/faq/categories/9838/3312.

[131] M. Båth, Introduction to Seismology, Cambridge university press, 1975. https://doi.org/10.1111/j.1365-246X.1975.tb01612.x.

[132] C. Richter, Types Of Earthquakes, (2020) 1–4. https://people.uwec.edu/.

[133] Y.Y. Kagan, D.D. Jackson, Statistical earthquake focal mechanism forecasts, Geophys. J. Int. 197 (2014) 620–629. https://doi.org/10.1093/gji/ggu015.

[134] US, Fault Types, (2020) 20. http://homepage.usask.ca/.

[135] I. Ketin, Über die tektonisch-mechanischen Folgerungen aus den großen anatolischen Erdbeben des letzten Dezenniums, Geol. Rundschau. 36 (1948) 77–83. https://doi.org/10.1007/BF01791916.

[136] A. Dilemre Didik, S., Tekin, Z., Türkiye termal ve mineralli sular envanteri Eskişehir, MTA Genel Müdürlüğü Enerj. Hammadde Etüd ve Aram. Dairesi Raporu. (1998).

[137] Y. Bayrak, T. Türker, Evaluating of the earthquake hazard parameters with Bayesian method for the different seismic source regions of the North Anatolian Fault Zone, Nat. Hazards. 85 (2017) 379–401. https://doi.org/10.1007/s11069-016-2569-5.

[138] MTU, Types of seismic waves, Engineering. (2012). http://www.geo.mtu.edu/.

[139] H. Kanamori, The energy release in great earthquakes, J. Geophys. Res. 82 (1977) 2981–2987. https://doi.org/10.1029/jb082i020p02981.

[140] Y. Aydin, Etude pétrographique et géochimique de la partie centrale du Massif d'Istranca (Turquie), Univ. Nancy. 1 (1974) 131.

[141] K. Kasahara, Earthquake mechanics., Earthq. Mech. (1981). https://doi.org/10.1016/0040-1951(83)90266-4.

[142] C.H. Scholz, L.R. Sykes, Y.P. Aggarwal, Earthquake prediction: A physical basis, Science (80-.). 181 (1973) 803–810. https://doi.org/10.1126/science.181.4102.803.

[143] V.I. Mjachkin, W.F. Brace, G.A. Sobolev, J.H. Dieterich, Two models for earthquake forerunners, in: Pure Appl. Geophys. PAGEOPH, Springer, 1975: pp. 169–181. https://doi.org/10.1007/BF01592908.

[144] B.A. Bolt, Earthquakes, WH Freeman and Company, San Fr. (1993).

[145] T. Rikitake, Earthquake prediction: an empirical approach, Tectonophysics. 148 (1988) 195–210.

[146] N. Segovia, S. de la Cruz-Reyna, M. Mena, E. Ramos, M. Monnin, J.L. Seidel, Radon in soil anomaly observed at Los Azufres geothermal field, Michoacan: a possible precursor of the 1985 Mexico earthquake (Ms = 8.1), Nat. Hazards. 1 (1989) 319–329. https://doi.org/10.1007/BF00134830.

[147] C.Y. King, W. Zhang, B.S. King, Radon anomalies on three kinds of faults in California, Pure Appl. Geophys. PAGEOPH. 141 (1993) 111–124. https://doi.org/10.1007/BF00876238.

[148] M. Garavaglia, G. Dal Moro, M. Zadro, Radon and tilt measurements in a seismic area: Temperature effects, Phys. Chem. Earth, Part A Solid Earth Geod. 25 (2000) 233–237. https://doi.org/10.1016/S1464-1895(00)00038-7.

[149] S. Uyeda, T. Nagao, K. Hattori, M. Hayakawa, K. Miyaki, O. Molchanov, V. Gladychev, L. Baransky, A. Chtchekotov, E. Fedorov, O. Pokhotelov, S. Andreevsky, A. Rozhnoi, Y. Khabazin, A. Gorbatikov, E. Gordeev, V. Chebrov, V. Sinitzin, A. Lutikov, S. Yunga, G. Kosarev, V. Surkov, G. Belyaev, Geophysical Observatory in Kamchatka region for monitoring of phenomena connected with seismic activity, Nat. Hazards Earth Syst. Sci. 1 (2001) 3–7. https://doi.org/10.5194/nhess-1-3-2001.

[150] G. Igarashi, S. Saeki, N. Takahata, K. Sumikawa, S. Tasaka, Y. Sasaki, M. Takahashi, Y. Sano, Ground-water radon anomaly before the kobe earthquake in Japan, Science (80-.). 269 (1995) 60–61. https://doi.org/10.1126/science.269.5220.60.

[151] E. Tabar, Dikili ve Bergama Bölgelerindeki Tektonik Aktivitenin Jeotermal Sularda Radon Ölçümleri ile Değerlendirilmesi, Nükleer Bilim. Enstitüsü, Ege Üniversitesi, İzmir, Türkiye. (2010).

[152] S.S. Kouris, P. Spalla, B. Zolesi, Could ionospheric variations be precursors of a seismic event? A short discussion, Ann. Geophys. 44 (2001) 395–402.

[153] D. Halliday, R.D. Present, Introductory Nuclear Physics, 1956. https://doi.org/10.1119/1.1934189.
[154] E.K.J. Pauwels, Radioactivity Radionuclides Radiation, Springer Science & Business Media, 2005. https://doi.org/10.1007/s00259-005-1805-0.
[155] W.R. Leo, D.G. Haase, Techniques for Nuclear and Particle Physics Experiments , Springer Science & Business Media, 1990. https://doi.org/10.1119/1.16209.
[156] A. Das, T. Ferbel, Introduction to Nuclear and Particle Physics, PHI Learning Pvt. Ltd., 2010. https://doi.org/10.1142/9789812564351.
[157] P.A. Tipler, G. Mosca, Physics for scientists and engineers., Thomson Learning, 2003.
[158] Lumen, Radioactivity, (2020). https://courses.lumenlearning.com/.
[159] SU, V.A.P.A.H.C.S. Stanford University, Radiation Safety Manual, Environmental Health and Safety, Stanford University, 2012.
[160] USNRC, Radiation Terminology, (2016). https://www.nrc.gov/.
[161] Saeed A Durran and Radomir Ilic, Radon Measurements by Etched Track Detectors/Applications in Radiation Protection, Earth Sciences and the Environment, World Scientific, 1997. https://www.worldscientific.com/worldscibooks/10.1142/3106.
[162] I.E. Zakharenkova, I.I. Shagimuratov, N.Y. Tepenitzina, A. Krankowski, Anomalous modification of the ionospheric total electron content prior to the 26 September 2005 Peru earthquake, J. Atmos. Solar-Terrestrial Phys. 70 (2008) 1919–1928. https://doi.org/10.1016/j.jastp.2008.06.003.
[163] Y. Ishimori, K. Lange, P. Martin, Y.S. Mayya, M. Phaneuf, Measurement and Radon Releases from Calculation of NORM Residues, IAEA, 2013.
[164] G. Etiope, G. Martinelli, Migration of carrier and trace gases in the geosphere: An overview, Phys. Earth Planet. Inter. 129 (2002) 185–204. https://doi.org/10.1016/S0031-9201(01)00292-8.
[165] J.E. Gingrich, Radon as a geochemical exploration tool, J. Geochemical Explor. 21 (1984) 19–39. https://doi.org/10.1016/0375-6742(84)90032-3.
[166] A. Mogro-Campero, R.L. Fleischer, Subterrestrial fluid convection: A hypothesis for long-distance migration of radon within the earth, Earth Planet. Sci. Lett. 34 (1977) 321–325. https://doi.org/10.1016/0012-821X(77)90017-6.
[167] K. Krister, M. Lennart, Evidence for nondiffusive transport of Rn in the ground and a new physical model for the transport, Geophysics. 47 (1982) 1444–1452. http://link.aip.org/link/?GPY/47/1444/1%5Cnhttp://dx.doi.org/10.1190/1.1441293.
[168] W.E. Clements, M.H. Wilkening, Atmospheric pressure effects on 222 Rn transport across the Earth-air interface , J. Geophys. Res. 79 (1974) 5025–5029. https://doi.org/10.1029/jc079i033p05025.
[169] J.L. Pinault, J.C. Baubron, Signal processing of diurnal and semidiurnal variations in radon and atmospheric pressure: A new tool for accurate in situ measurement of soil gas velocity, pressure gradient, and tortuosity, J. Geophys. Res. B Solid Earth. 102 (1997) 18101–18120. https://doi.org/10.1029/97jb00971.
[170] S.D. Schery, D. Siegel, The role of channels in the transport of radon from the soil, J. Geophys. Res. Solid Earth. 91 (1986) 12366–12374. https://doi.org/10.1029/jb091ib12p12366.
[171] H.L. Beck, Gamma radiation from radon daughters in the atmosphere, J. Geophys. Res. 79 (1974) 2215–2221. https://doi.org/10.1029/jc079i015p02215.

[172] F. Aumento, Radon tides on an active volcanic island: Terceira, Azores, Geofis. Int. 41 (2002) 499–505.

[173] P. Talwani, W.S. Moore, J. Chiang, Radon anomalies and microearthquakes at Lake Jocassee, South Carolina., J. Geophys. Res. 85 (1980) 3079–3088. https://doi.org/10.1029/JB085iB06p03079.

[174] P.G. Silver, H. Wakita, A search for earthquake precursors, Science (80-.). 273 (1996) 77–78. https://doi.org/10.1126/science.273.5271.77.

[175] H. Wakita, Geochemical challenge to earthquake prediction, Proc. Natl. Acad. Sci. U. S. A. 93 (1996) 3781–3786. https://doi.org/10.1073/pnas.93.9.3781.

[176] M.A. Sadovsky, I.L. Nersesov, S.K. Nigmatullaev, L.A. Latynina, A.A. Lukk, A.N. Semenov, I.G. Simbireva, V.I. Ulomov, The processes preceding strong earthquakes in some regions of middle Asia, Tectonophysics. 14 (1972) 295–307. https://doi.org/10.1016/0040-1951(72)90078-9.

[177] P.M. Muller, Proceedings of the Lectures By the Seismological Delegation of the People'S Republic of China, 1976., Jet Propulsion Laboratory, California Institute of Technology, 1976.

[178] L. Kamra, V.M. Choubey, N. Kumar, G. Rawat, D.D. Khandelwal, Radon variability in borehole from Multi-Parametric Geophysical Observatory of NW Himalaya in relation to meteorological parameters, Appl. Radiat. Isot. 72 (2013) 137–144. https://doi.org/10.1016/j.apradiso.2012.10.019.

[179] Y. -C Chung, Correction [to "Radium-226 and radon-222 in southern California groundwaters: Spatial variations and correlations"], Geophys. Res. Lett. 8 (1981) 945–945. https://doi.org/10.1029/GL008i008p00945.

[180] M. Tarakçi, C. Harmanşah, M.M. Saç, M. Içhedef, Investigation of the relationships between seismic activities and radon level in Western Turkey, Appl. Radiat. Isot. 83 (2014) 12–17. https://doi.org/10.1016/j.apradiso.2013.10.008.

[181] E. Tabar, M.N. Kumru, M. Içhedef, M.M. Saç, Radioactivity level and the measurement of soil gas radon concentration in Dikili geothermal area, Turkey, Int. J. Radiat. Res. 11 (2013) 253.

[182] F.S. Erees, S. Aytas, M.M. Sac, G. Yener, M. Salk, Radon concentrations in thermal waters related to seismic events along faults in the Denizli Basin, Western Turkey, Radiat. Meas. 42 (2007) 80–86. https://doi.org/10.1016/j.radmeas.2006.06.003.

[183] K.M. Abumurad, M.H. Al-Tamimi, Natural radioactivity due to radon in Soum region, Jordan, Radiat. Meas. 39 (2005) 77–80. https://doi.org/10.1016/j.radmeas.2004.02.017.

[184] V.S. Iakovleva, N.K. Ryzhakova, Spatial and temporal variations of radon concentration in soil air, Radiat. Meas. 36 (2003) 385–388. https://doi.org/10.1016/S1350-4487(03)00156-2.

[185] P. Amponsah, B. Banoeng-Yakubo, A. Andam, D. Asiedu, Soil radon concentration along fault systems in parts of south eastern Ghana, J. African Earth Sci. 51 (2008) 39–48. https://doi.org/10.1016/j.jafrearsci.2007.11.004.

[186] M. Ngachin, M. Garavaglia, C. Giovani, M.G. Kwato Njock, A. Nourreddine, Radioactivity level and soil radon measurement of a volcanic area in Cameroon, J. Environ. Radioact. 99 (2008) 1056–1060. https://doi.org/10.1016/j.jenvrad.2007.12.022.

[187] H. Chaudhuri, N.K. Das, R.K. Bhandari, P. Sen, B. Sinha, Radon activity measurements around Bakreswar thermal springs, Radiat. Meas. 45 (2010) 143–146. https://doi.org/10.1016/j.radmeas.2009.11.039.

[188] V.M. Choubey, P.K. Mukherjee, B.S. Bajwa, V. Walia, Geological and tectonic influence on water-soil-radon relationship in Mandi-Manali area, Himachal Himalaya, Environ. Geol. 52 (2007) 1163–1171. https://doi.org/10.1007/s00254-006-0553-1.

[189] J. Chen, R. Falcomer, J. Ly, J. Wierdsma, L. Bergman, Long-term monitoring of soil gas radon and permeability at two reference sites, Radiat. Prot. Dosimetry. 131 (2008) 503–508. https://doi.org/10.1093/rpd/ncn274.

[190] K. Davies, Ionospheric Radio, IET, 1990. https://doi.org/10.1049/pbew031e.

[191] M.J. Rycroft, The upper atmosphere, data analysis and interpretation, J. Atmos. Solar-Terrestrial Phys. 60 (1998) 141. https://doi.org/10.1016/s1364-6826(97)82764-2.

[192] T. Ondoh, K. Marubashi, Science of space environment, IOS Press, 2001. https://books.google.com/books?hl=en&lr=&id=F_UpI_Our3AC&oi=fnd&pg=PA1&dq=Wave+summit+course%3B+Science+of+Space+Environment,+Ohmsha,+Ltd.+3-1+Kanda+Nishiki-cho,+Chiyoda-ku,+Tokyo+101-8460+Japan,+2000.&ots=MhH0OKiRXQ&sig=A6EnR6MB9W5gC3-L-p-TWpZjRdA.

[193] P.J. Wilkinson, P. Richards, K. Igarashi, E.P. Szuszczewicz, Ionospheric climatology and weather in the Australian-Japanese sector during the SUNDIAL/ATLAS 1 campaign, J. Geophys. Res. Sp. Phys. 101 (1996) 26769–26782.

[194] H. Rishbeth, U.R.S.I. handbook of ionogram interpretation and reduction, Planet. Space Sci. 21 (1973) 1272. https://doi.org/10.1016/0032-0633(73)90217-1.

[195] P.F. Weaver, P.C. Yuen, G.W. Prolss, A.S. Furumoto, Acoustic coupling into the ionosphere from seismic waves of the earthquake at Kurile Islands on August 11, 1969, Nature. 226 (1970) 1239–1241.

[196] S.A. Pulinets, V.P. Kim, V. V. Hegai, V.K. Depuev, S.M. Radicella, Unusual longitude modification of the night-time midlatitude F2 region ionosphere in July 1980 over the array of tectonic faults in the Andes area: Observations and interpretation, Geophys. Res. Lett. 25 (1998) 4133–4136. https://doi.org/10.1029/1998GL900109.

[197] S.A. Pulinets, Prospects of Topside Sounding, World Ionos. Study WITS Handb. N2. 2 (1989) 99–127. http://scholar.google.com/scholar?hl=en&btnG=Search&q=intitle:Prospects+of+Topside+Sounding#0%5Cnhttp://pulse1549.hut2.ru/PAPERS/WITS.PDF.

[198] R.L. Fleischer, Radon flux from the Earth: Methods of measurement by the nuclear track technique, J. Geophys. Res. Ocean. 85 (1980) 7553–7556. https://doi.org/10.1029/jc085ic12p07553.

[199] Y.I. Stozhkov, G.A. Bazilevskaya, V.I. Ermakov, P.E. Pokrevskij, Ion production in the atmosphere, Izv. Akad. Nauk. Ross. Akad. Nauk. Seriya Fiz. 61 (1997) 1155–1158.

[200] E.A. Martell, Enhanced ion production in convective storms by transpired radon isotopes and their decay products., J. Geophys. Res. 90 (1985) 5909–5916. https://doi.org/10.1029/JD090iD04p05909.

[201] R.E. Orville, D.W. Spencer, Global lightning flash frequency., Mon. Weather Rev. 107 (1979) 934–943. https://doi.org/10.1175/1520-0493(1979)107<0934:GLFF>2.0.CO;2.

[202] B.N. Turman, B.C. Edgar, Global lightning distributions at dawn and dusk., Journa Geophys. Res. 87 (1982) 1191–1206. https://doi.org/10.1029/JC087iC02p01191.

[203] R.M. Records, The Electrical Nature of Matter, Oxford University Press on Demand, 1973. https://doi.org/10.1080/00368121.1973.9957659.

[204] S. Pulinets, The Possibility of Earthquake Forecasting: Learning from nature, IOP Publishing, 2018. https://doi.org/10.1088/978-0-7503-1248-6.

[205] R.G. Roble, The global atmospheric-electrical circuit, Earth's Electr. Environ. (1986) 206–231.

[206] J.Y. Liu, Y.J. Chuo, S.J. Shan, Y.B. Tsai, Y.I. Chen, S.A. Pulinets, S.B. Yu, Pre-earthquake ionospheric anomalies registered by continuous GPS TEC measurements, Ann. Geophys. 22 (2004) 1585–1593. https://doi.org/10.5194/angeo-22-1585-2004.

[207] S. Pulinets, K. Boyarchuk, Ionospheric precursors of earthquakes, Ionos. Precursors Earthquakes. (2005) 1–315. https://doi.org/10.1007/B137616/COVER.

[208] S. Mie, K. Ryu, K. Min, Ionospheric anomalies related to strong earthquakes in North America as observed by TEC, Adv. Sp. Res. 68 (2021) 4137–4154. https://doi.org/10.1016/j.asr.2021.07.026.

[209] S. Pulinets, D. Davidenko, Ionospheric precursors of earthquakes and Global Electric Circuit, Adv. Sp. Res. 53 (2014) 709–723. https://doi.org/10.1016/j.asr.2013.12.035.

[210] S.A. Pulinets, D. V. Davidenko, The Nocturnal Positive Ionospheric Anomaly of Electron Density as a Short-Term Earthquake Precursor and the Possible Physical Mechanism of Its Formation, Geomagn. Aeron. 58 (2018) 559–570. https://doi.org/10.1134/S0016793218040126.

[211] G.A. Papadopoulos, M. Charalampakis, A. Fokaefs, G. Minadakis, Strong foreshock signal preceding the L ' Aquila (Italy) earthquake, (2010) 19–24.

[212] R. Armijo, B. Meyer, A. Hubert, A. Barka, Westward propagation of the North Anatolian fault into the northern Aegean: Timing and kinematics, Geology. 27 (1999) 267–270. https://doi.org/10.1130/0091-7613(1999)027<0267:WPOTNA>2.3.CO;2.

[213] B. Yücel, R. Özgür, Reşadiye (Tokat) bölgesinin jeolojisi ve jeotermal enerji olanaklari, Mineral Research and Exploration Directorate, TOKAT, 1992. Report No 10466.

[214] B.L. Mesci, H. Gürsoy, B. Ghaleb, O. Tatar, An Extensional Fracture Acting as Hot Water Source for Travertine Deposition on the North Anatolian Fault Zone, Turkey: The Reşadiye Fissure-Ridge, Türkiye Jeol. Bülteni. 63 (2020) 145–160.

[215] Earthquake Catalog - BOUN KOERI Regional Earthquake-Tsunami Monitoring Center, (n.d.). http://www.koeri.boun.edu.tr/sismo/2/earthquake-catalog/ (accessed July 1, 2022).

[216] A. Alam, N. Wang, G. Zhao, A. Barkat, Implication of Radon Monitoring for Earthquake Surveillance Using Statistical Techniques: A Case Study of Wenchuan Earthquake, (2020). https://doi.org/10.1155/2020/2429165.

[217] MainPage, (n.d.). https://web.ics.purdue.edu/~braile/edumod/MagCalc/MagCalcLocal/MagCalc.htm (accessed May 31, 2022).

[218] D.M. Thomas, J.M. Cotter, D. Holford, Experimental design for soil gas radon monitoring, J. Radioanal. Nucl. Chem. Artic. 161 (1992) 313–323. https://doi.org/10.1007/BF02040478.

[219] U. Sezen, F. Arikan, O. Arikan, O. Ugurlu, A. Sadeghimorad, Online, automatic, near-real time estimation of GPS-TEC: IONOLAB-TEC, Sp. Weather. 11 (2013) 297–305. https://doi.org/10.1002/SWE.20054.

[220] F. Arikan, U. Sezen, T.L. Gulyaeva, O. Cilibas, Online, automatic, ionospheric maps: IRI-PLAS-

MAP, Adv. Sp. Res. 55 (2015) 2106–2113. https://doi.org/10.1016/J.ASR.2014.10.016.

[221] K. Kauristie, A. Morschhauser, N. Olsen, C.C. Finlay, R.L. McPherron, J.W. Gjerloev, H.J. Opgenoorth, On the Usage of Geomagnetic Indices for Data Selection in Internal Field Modelling, Space Sci. Rev. 206 (2017) 61–90. https://doi.org/10.1007/S11214-016-0301-0/FIGURES/9.

[222] J.S. Armstrong, K.C. Green, A. Graefe, Golden rule of forecasting: Be conservative, J. Bus. Res. 68 (2015) 1717–1731. https://doi.org/10.1016/J.JBUSRES.2015.03.031.

[223] I. Yilmaz, O. Kaynar, Multiple regression, ANN (RBF, MLP) and ANFIS models for prediction of swell potential of clayey soils, Expert Syst. Appl. 38 (2011) 5958–5966. https://doi.org/10.1016/J.ESWA.2010.11.027.

[224] G. Zhang, B. Eddy Patuwo, M. Y. Hu, Forecasting with artificial neural networks:: The state of the art, Int. J. Forecast. 14 (1998) 35–62. https://doi.org/10.1016/S0169-2070(97)00044-7.

[225] A. Muhammad, F. Külahcı, P. Akram, Modeling radon time series on the North Anatolian Fault Zone, Turkiye: Fourier transforms and Monte Carlo simulations, Nat. Hazards. 104 (2020) 979–996. https://doi.org/10.1007/s11069-020-04200-8.

[226] W. Liu, L. Xu, Statistical analysis of ionospheric TEC anomalies before global M w ≥ 7.0 earthquakes using data of CODE GIM, J. Seismol. 21 (2017) 759–775. https://doi.org/10.1007/S10950-016-9634-0/FIGURES/5.

[227] S.P. Brooks, Markov chain Monte Carlo method and its application, J. R. Stat. Soc. Ser. D Stat. 47 (1998) 69–100. https://doi.org/10.1111/1467-9884.00117.

[228] D. van Ravenzwaaij, P. Cassey, S.D. Brown, A simple introduction to Markov Chain Monte–Carlo sampling, Psychon. Bull. Rev. 25 (2018) 143–154. https://doi.org/10.3758/S13423-016-1015-8/FIGURES/3.

[229] S. Meenakshisundaram, A. Srikanth, V.K. Ganesan, N. Vijayarangan, A.P. Srinivas, Forecasting: Bayesian Inference Using Markov Chain Monte Carlo Simulation, Smart Innov. Syst. Technol. 134 (2019) 215–228. https://doi.org/10.1007/978-981-13-5974-3_19.

[230] G.E.P. Box, G.M. Jenkins, G.C. Reinsel, Time series analysis: Forecasting and control: Fourth edition, Wiley, 2013. https://doi.org/10.1002/9781118619193.

CURRICULUM VITAE

Pishtiwan Akram Hama Rashid

[redacted]

ACADEMIC ACTIVITIES

Paper:

1. A. Muhammad, F. Külahcı, and P. Akram, “Modeling radon time series on the North Anatolian Fault Zone, Turkiye: Fourier transforms and Monte Carlo simulations,” Nat. Hazards, vol. 104, no. 1, pp. 979–996, 2020.
2. A. Muhammad, F. Külahcı, H. Salh, and P. A. Hama Rashid, “Long Short-Term Memory networks (LSTM)-Monte-Carlo simulation of soil ionization using radon,” J. Atmos. Solar-Terrestrial Phys., vol. 221, p. 105688, Sep. 2021.